Spin Electronics in Two-Dimensional Surface Conducting Diamonds

Golrokh Akhgar, *MSc, BEng*

This thesis presented in total fulfilment of the requirements for the degree of

Doctor of Philosophy

Department of Chemistry and Physics
School of Molecular Sciences
College of Science, Health and Engineering

La Trobe University
Victoria, Australia

October 2018

Abstract

When the surface of diamond is terminated with hydrogen and exposed to air it develops a pronounced p-type surface conductivity through the process of surface transfer doping. While this system has been exploited for a variety of electronic device applications at room temperature, its low-temperature transport properties have remained largely elusive due to carrier freeze-out as a result of poor surface quality. Recently, improvements in the quality of synthetic diamond material and surface processing protocols have enabled high-quality C(100):H surfaces to be prepared which retain metallic conductivity to low temperatures. This allows the phase coherent transport properties to be probed and a demonstration that the hole accumulation layer forms a two-dimensional (2D) hole band.

In this thesis, we explore the spin transport properties of the 2D hole band using low-temperature magnetotransport. Phase coherent backscattering effects in the form of weak localization and weak anti-localization are utilised as a powerful probe to the spin-orbit interaction, the in-plane gyromagnetic ratio, and the homogeneity of the 2D quantum well on lateral length scales of a few tens of nanometres at the diamond surface. To our knowledge, this is the first time that these properties, which are important in providing an assessment of the utility of a material for spin-transport devices, have been experimentally determined for surface conducting diamond.

By developing electrostatic gating protocols with an ionic liquid gate, we show that the 2D hole band possesses a strong and tunable spin-orbit interaction on account of the Rashba effect which arises due to the highly asymmetric quantum well at the diamond surface. The observed spin-orbit coupling was found to surpass, in both magnitude and tunability, that of other 2D hole and electron systems, pointing towards a role for diamond in future low-power electronics based upon spin transport.

By performing magnetotransport measurements with an additional in-plane applied magnetic field we probe the Zeeman effect which destroys weak localization. Through these experiments we determine the in-plane g-factor of the 2D hole band which importantly determines the coupling strength of spins with an external magnetic field and probe the homogeneity fluctuations in the width of the quantum well. Furthermore, the

change in g-factor and quantum well fluctuations as the hole carrier density is varied is evaluated by electrostatic gating.

We show that the fluctuation in the width of the 2D hole layer arises largely from a lateral inhomogeneity of the hole carrier density rather than from roughness of the diamond surface. Our data suggests that under high gate biases, using an ionic liquid gate, long-range fluctuations in the width of the quantum well may be induced such that fluctuations have a greater effect on the transport properties of the hole accumulation layer at higher carrier density.

Statement of Authorship

This thesis includes work by the author that has been published or accepted for publication as described in the text. Except where reference is made in the text of the thesis, this thesis contains no other material published elsewhere or extracted in whole or in part from a thesis accepted for the award of any other degree or diploma.

No other person's work has been used without due acknowledgment in the main text of the thesis.

This thesis has not been submitted for the award of any degree or diploma in any other tertiary institution.

Signed,

Golrokh Akhgar

12October 2018

Acknowledgment

First I would like to thank my supervisor and mentor for both my Masters and my PhD, Professor Chris Pakes. His great support and invaluable advice in all situations helped me to progress through my work since the first year I moved to Melbourne. Your guidance, patience and instruction helped me immensely throughout my Masters, PhD, all of my experimental work, and in writing this thesis. I cannot think of a better supervisor to have.

I have had a number of co-supervisors; to Professor Alex Hamilton, your knowledge of devices and 2D materials has been invaluable. I have learned so much since the beginning of my PhD from our discussions and under your guidance. I had some of my best time in your lab in UNSW, Sydney. To Professor Lothar Ley, this work would not have been possible without your infinite knowledge of diamonds. I truly appreciate all your wisdom and all the time you spent discussing with me. You made me feel the luckiest PhD student! To Dr Dongchen Qi, thank you for your guidance for over the years and valuable suggestions.

To the postdocs that I worked with in the various parts of my projects - Dr Daniel Creedon, Dr Laurens Willems van Beveren and Dr Oleh Klochan. You thought me how the dilution refrigerators work, and I had the great learning experience of setting up instruments while working alongside you in the lab. To Dr Mark Edmonds and Dr Kevin Rietwyk thanks for your invaluable career advice, I owe a great depth of gratitude to you.

To all other people at La Trobe university, The University of Melbourne and UNSW that I worked with. Particularly, Associate Professor Jeff McCallum, Dr Alastair Stacey and Dr David Hoxley for encouragement, motivation and offering great advice along the way. To Ben Spencer, Alex Schenk, Michael Stuiber, Michael Sear, Fadhlia Zakaria, Kaijian Xing, Steve Yianni and Manjith Bose, working alongside you have been a lot fun! Kaijian, Steve and Manjith, good luck with your PhDs.

To Catherine Sadatnajafi who always been with me unconditionally since the very beginning of my time at La Trobe University. Thank you for being there for me, you helped me not give up, and survive all the stress! To Jennifer Chen, who helped me

through my conference and PhD talks. Thanks for listening to me talking about physics and diamonds for hours. You made my PhD life easier!

I would also like to extend a special thanks to my parents Ali and Mahrokh, their words and support helped me through highs and lows. I could not be where I am without your support. And also to my sister and brother, Alice and Reza for all their support, I could not wish for any better siblings.

This work was supported by an Australian Government Research Training Program Scholarship.

List of Publications

Chapter 3

G. Akhgar, O. Klochan, L. H. Willems van Beveren, M. T. Edmonds, F. Maier, B. J. Spencer, J. C. McCallum, L. Ley, A. R. Hamilton, C. I. Pakes, "*Strong and Tunable Spin-Orbit Coupling in a Two-Dimensional Hole Gas in ionic-liquid gated Diamond Devices*", *Nano Letters* 16 (6), 3768-3773 (2016).

Chapter 4

G. Akhgar, D. L. Creedon, L. H. Willems van Beveren, A. Stacey, D. I. Hoxley, J. C. McCallum, L. Ley, A. R. Hamilton, and C. I. Pakes,"*G-factor and well width variations for the two-dimensional hole gas in surface conducting diamond", Applied Physics Letters* 112, 042102 (2018).

Chapter 5

G. Akhgar, L. Ley, D. L. Creedon, A. Stacey, J. C. McCallum, A. R. Hamilton, and C. I. Pakes *"G-factor and well width fluctuation of carrier density in the 2D hole accumulation layer of transfer doped diamond", Physical Review B* (Under review, Submitted October 2018)

List of Acronyms

1D/2D/3D	One/Two/ Three Dimensional
2DHG	Two dimensional hole gas
ALD	Atomic Layer Deposition
CB	Conduction band
FET	Field Effect Transistors
HHI	Hole-Hole Interaction
I-V	Current-voltage (characteristics)
MESFET	Metal-Semiconductor Field Effect Transistor
SGFET	Solution Gated Field Effect transistor
MISFET	Metal-Insulator Field Effect Transistor
MOSFET	Metal-Oxide Field Effect Transistor
NEA	Negative electron affinity
PEA	Positive electron affinity
QW	Quantum Well
SC	Surface conductivity
UV	Ultraviolet
VB	Valence band
VBM	Valence band maximum
WAL	Weak anti-Localization
WL	Weak Localization

Table of Contents

1

Introduction and Literature Review

1.1 Introduction

There has been enormous interest in engineering electronic devices with reduced dimensionality, ranging from two-dimensional (2D) heterostructured semiconductors, and one-dimensional (1D) quantum point contacts and carbon nanotubes, to quantum dot structures [1-3]. Nowadays, the field effect transistor (FET) based on semiconducting materials which support a 2D electron band are one of the most common electronic devices in industry [4, 5]. The realisation of graphene with what was at the time a novel 2D bandstructure has led to a new phase of discovery of systems which support a 2D band at the surface of a material or in atomically thin materials.

The hydrogen-terminated surface of diamond can support a *p*-type surface conductivity as a result of surface transfer doping [6]. In this doping mechanism, a hole accumulation layer is induced just below the diamond surface as a result of electron transfer into a surface water layer or adlayer materials with sufficiently high electron affinity. As we shall explain, and despite the simplicity of the doping mechanism, the hole accumulation layer takes the form of a metallic 2D hole band with a high carrier density up to about 10^{14} cm^{-2}. Furthermore, unlike interstitial doping in the bulk of a semiconductor which is subject to carrier freeze out at low temperature, surface transfer doping of diamond is

achieved with a negative acceptor energy so, in principle, metallic transport may be retained even at very low temperature. In this thesis we undertake an in-depth study of the magnetotransport properties of this 2D hole system, from which its spin transport properties are explored. The band bending at the diamond surface induced by the surface doping gives rise to hole confinement in a highly asymmetric quantum well, ultimately because the high electrostatic break-down field of diamond permits the material to support a high electric field. As we shall show, for holes confined by this potential the spin-orbit interaction is very large and outstrips in both its magnitude and tunability that of other 2D hole systems [7-9]. This both makes the spin-transport properties of the surface conducting layer in diamond fundamentally interesting and suggests that this system may have potential as a material for future spintronic applications.

Spintronics conceptually aims to use spin, rather than charge, to transport information in a controlled manner [10]. There are two fundamental mechanisms that may influence the electron spin and must be understood for any material studied with spin transport applications in mind. These are the spin-orbit interaction, which governs the strength of coupling of the carrier spin to its orbital motion and is central to the operation of a spin filter or spin field effect transistor device, and the Zeeman interaction which governs the coupling of carrier spins to an external magnetic field. Magnetotransport measurements have been widely used as a tool to study these mechanisms in low dimensional electron systems [11-13] through the observation of quantum coherent backscattering effects in the form of weak localization (WL) and weak anti-localization (WAL). These effects can be used to inform the dimensionality of the system, the phase and spin coherent lengths along with the corresponding relaxation times, the spin-orbit coupling and the gyromagnetic ratio in the carrier band, and provide information about the microroughness of the confinement potential well. The study of spin transport in surface conducting diamond is in its infancy and these effects are either not fully understood or are yet to be explored.

This thesis undertakes an in-depth study of WL and WAL effects in surface conducting diamond with the aim of determining these important properties which will determine the utility of using this system for future spintronic applications:

A. To study the strength of the spin-orbit coupling in the 2D hole band and to determine its response to applied magnetic and electric fields.

B. Through a measurement of the Zeeman interaction, to determine the in-plane gyromagnetic ratio (g-factor) of holes in the 2D band which determines the response of the hole spins to an applied magnetic field.
C. To examine the possible mechanisms that lead to changes in the in-plane g-factor and additional dephasing of the hole spin as a result of sample microroughness.

The thesis is outlined as follows. The remainder of this chapter is devoted to reviewing the literature relating to the properties of the hydrogen-terminated surface of diamond, the mechanism of surface transfer doping, and the transport properties of surface conducting diamond devices. There is limited literature on the low temperature magnetotransport of surface-conducting diamond so, in addition, we consider a number of relevant articles on similar 2D systems. In Chapter 2 we discussed the techniques used in the present study for device fabrication and magnetotrasport measurements. The quantum transport theories that are required to fit and to interpret the experimental data are also discussed in Chapter 2. Chapters 3-5 present the experimental results in the form of journal articles. Chapter 3 explores the possibility of engineering the spin-orbit coupling in the 2D hole band in diamond by gating the surface with an ionic liquid gate. The evolution of the magnetotransport curves from WL to WAL behaviour is studied as a function of temperature and of gate voltage and the tunability of the spin-orbit coupling explored. In Chapter 4 we explore magnetotransport in this system in the presence of an in-plane magnetic field. By performing systematic magnetoconductance measurements as the in-plane field component is increased we quantify dephasing of the WAL signature due to the Zeeman effect. We report the gyromagnetic ratio (or g-factor) of the holes in the 2D surface band for the first time; this is important since it describes the extent of coupling of spins in a spintronic material to an applied magnetic field. As we shall show, the parallel magnetic field measurements also allow us to probe the microroughness of the hole quantum well and, by comparing the results of magnetoconductance measurements with surface topographic data obtained using atomic force microscopy, we show that the hole accumulation layer in diamond exhibits significant lateral variation in local carrier density. In Chapter 5, we bring together ionic liquid gating and in-plane magnetotransport techniques to explore how the g-factor and hole well microroughness is influenced by macroscopic variations in the carrier density. Finally, Chapter 6 draws conclusions from this work and suggests opportunities for future work.

1.2 Literature Review

1.2.1 History and Background

Diamond has been known as the hardest material for over two thousand years and was for many years utilised only for its mechanical properties and as a gem stone. However, in recent years, as the control over diamond synthesis has improved and the availability of low-cost synthetic material has increased, the study of its electronic and optical properties has become prevalent [14].

The crystal structure of diamond is cubic with eight atoms per unit cell. Each carbon atom is tetrahedrally surrounded by four nearest neighbours and the carbon atoms are covalently bonded via sp^3 hybrids [15]. Figure 1 shows the face-centred cubic (fcc) diamond unit cell with the two atomic bases indicated by the two interpenetrating cubes [16].

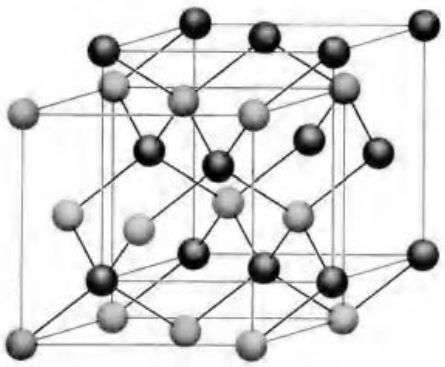

Figure 1: Two cubes of diamond lattice. Showing the fcc crystal structure of diamond with sp3 bonding [15].

When un-doped, diamond is a bona fide insulator with carrier concentrations of about 10^{-28} cm^{-3} and an intrinsic conductivity below 10^{-16} $\Omega^{-1}cm^{-1}$. It has a large band gap of 5.47 eV, the largest among all other semiconductors, due to the strong covalent bonds with large bonding - antibonding splitting [16]. As a result, diamond has historically been a less popular electronic material when compared to other semiconductors because of its low carrier concentration at normal operating temperatures and non-trivial doping. The key issue with diamond is the lack of shallow dopants. If such dopants existed it could be a great transparent conductive material. However, because of it's extremely high thermal conductivity, as well as its high breakdown field and low dielectric constant, and large

bandgap, diamond is of significant interest for a variety of applications requiring exceptional properties such as electronic devices operating with high-power and at high temperature [14, 17]. Moreover, rapid progress in the development of high quality CVD diamond growth has resulted in a reduction of the impurity content and a corresponding increase in the carrier mobility. Advances in protocols for bulk doping with boron and phosphorus, yielding p and n-type material, have increased the utility of diamond for high-power, high frequency devices, and opto-electronics [16].

1.2.2 The Diamond (100) Surface

For electronic applications, single crystal CVD diamond with a (100) surface orientation is the most useful. Okashi *et al.* and Ri *et al.* have shown that CVD diamond growth can produce a (100) plane with smooth surfaces of low misorientation angle by using CH_4/H_2 with high methane concentrations [18, 19]. Methane helps to increase the growth rate, however it is worth noting that this is not useful for processing thick and large-scale diamonds but is more useful for thin film diamonds [18-20].

Figure 2(a) shows the atomic arrangement of the (100) surface with the surface unit cell defined by the blue square. Each atom on the diamond (100) surface has two dangling bonds. This so called (1x1) unreconstructed surface is very unstable. Consequently, in order to stabilise the surface, two neighbouring dangling bonds can lower their energy by forming mutual bonds along the [011] direction and thereby form rows of π-bonded dimers. This leads to the reconstruction of the surface into a 2x1 unit cell as shown by the blue rectangle in figure 2(b). [16].

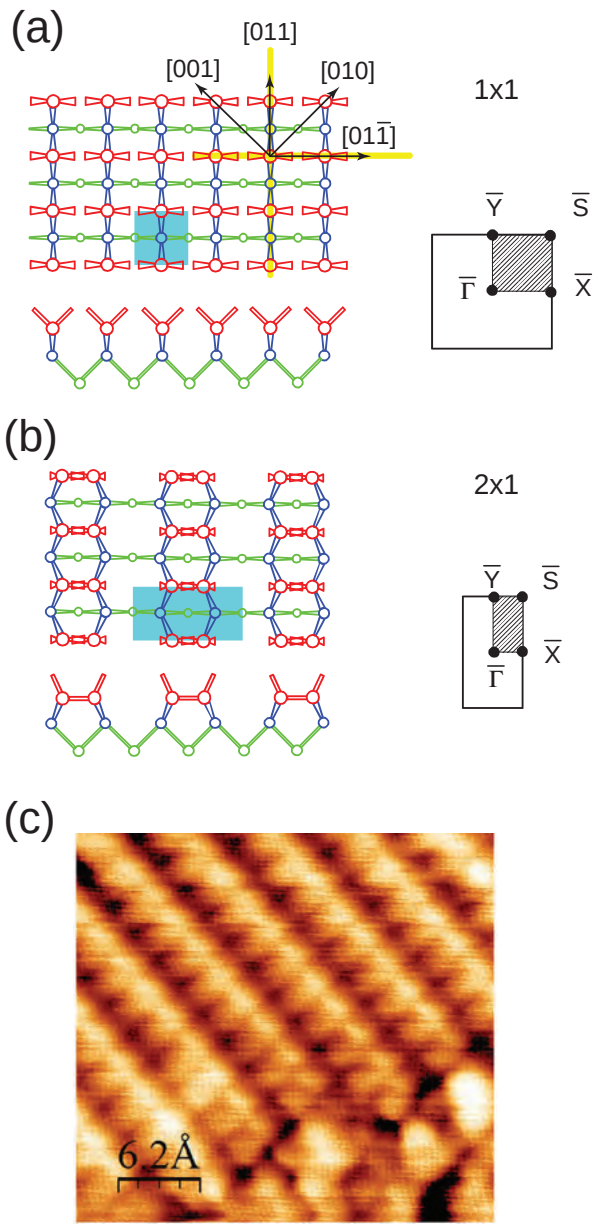

Figure 2: Schematic image of the diamond (100) surface: (a) (showing the top view of unreconstructed 1x1 unit mesh with crystallography direction parallel to the surface and along the mirror planes (yellow shaded axes, [011] and [01$\bar{1}$]). (right hand side) surface Brillioun zone with the irreducible part shaded that shows high symmetry in the conventional used notation; (bottom) showing the side view of the top three atomic layers along with dangling bonds. (b) (top) showing the top view of the 2x1 reconstructed geometry with neighbouring carbon atoms forming dimers. (right hand side) The surface Brillioun zone. (bottom) Illustrating the side view of the reconstructed surface with carbon atoms bonding with their neighbouring atoms to form rows of dimers[16]. (c) High resolution STM image illustrating dimer structure of the surface [21].

1.2.3 Hydrogen-terminated Diamond

To date, the most important atomic species for termination of the diamond surface is hydrogen. Hydrogen terminated surfaces are usually prepared via exposure of the surface to a microwave hydrogen plasma, including post-CVD plasma hydrogenation. The advantage of hydrogen terminated diamond (100) compared to the other relevant surfaces of group IV semiconductors, such as Si and Ge, is the high stability and passive nature. Unlike, hydrogen-terminated silicon, for example, the C(100):H surface is stable in area for a considerable period of time. This stabilisation is due to the saturation of all dangling bonds on the diamond (100) surface with hydrogen and the strength of the C-H bond [22, 23]. Compared to the clean, (2x1) reconstructed (100) surface, one hydrogen at each surface atom forms a covalent C-H bond and thereby destroys the π-bond between the dimer atoms. The transition from a double to a single bond increases the bond length between the C-C atoms to 1.16A. However, the unit cells maintains the same symmetry, namely (2x1) [16].

1.2.4 The Electronic Properties of the Hydrogen-terminated Diamond Surface

An electron has to overcome an energy barrier known as the work function ∅ in order to escape from a solid into vacuum level. The work function is the difference between the energy of the vacuum level E_{vac} and the Fermi energy E_f ($\emptyset = E_{vac} - E_f$). However, the work function is influenced by doping and surface band bending which makes it a less unique material property for a semiconductor. Therefore, parameters that can more usefully define the energies of the electron states at the surface are the electron affinity ($\chi = E_{vac} - E_c$) and the ionisation energy ($I = E_{vac} - E_v$), where E_v and E_c are the valence band maximum and the conduction band minimum respectively [14, 16]. The hydrogen-terminated surface possesses a negative electron affinity (NEA), in which the vacuum level is energetically below the conduction band minimum and hence $\chi = E_{vac} - E_c < 0$ [14]. NEA on diamond was first reported by Himpsel *et al.* in the late seventies [24] and corresponding measurements by Cui *et al.* [25] and Maier *et al.* [26] accurately determined the electron affinity and hence the ionisation energy as a function of hydrogen coverage on the diamond surface. A negative electron affinity of -1.3 eV and an ionisation energy of 4.2 eV have been determined for the fully hydrogenated single crystalline diamond (111) surface [25, 26]. An ionisation energy of 4.2 eV is the lowest

amongst all commonly used semiconductors; silicon, for example, has an ionisation energy of 5.2 eV [26].

In contrast to the hydrogen-terminated surface, when the surface of a diamond is terminated with oxygen it results in a positive electron affinity of +1.7 eV, with the vacuum level residing above the conduction band minimum, and an ionisation energy of 7.2 eV. As Figure 3 demonstrates, the clean surface of diamond has a barrier for electron emission from the conduction band and this barrier is χ = +0.4 eV high corresponding to an ionisation energy of 5.9 eV. For the hydrogen-terminated surface, the ionic $C^{-}H^{+}$ bonds set up a dipole layer at the surface which results in a potential drop ΔV at the surface i.e. pushing the vacuum level energetically below E_c. On the other hand, when the surface is terminated with oxygen instead of hydrogen, a dipole layer with opposite sign is formed on the oxygen terminated diamond surface, as oxygen has a higher electronegativity compared with carbon on the Pauling scale [14, 16, 26]. This results in a potential step in the opposite direction which increases the electron affinity.

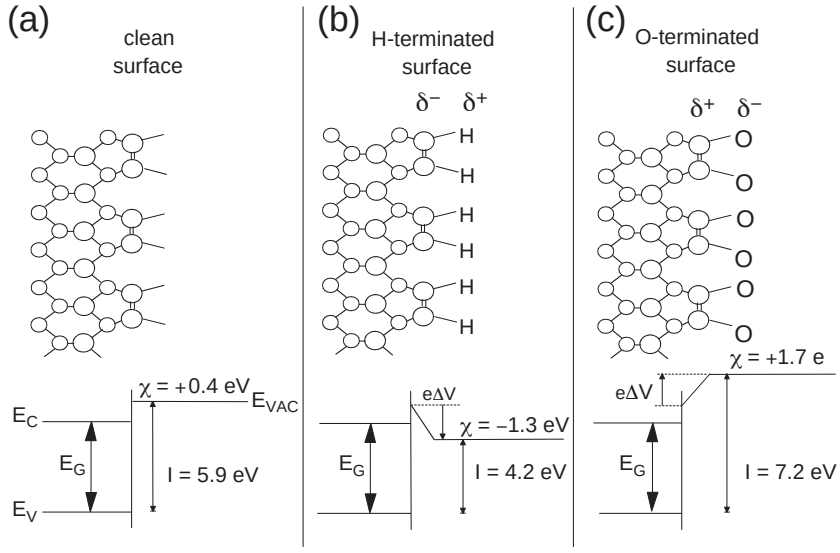

Figure 3: (Top) Schematic cross-section of the atomic arrangement at the diamond surface and (Bottom) the band diagrams corresponds to (a) clean surface, (b) when the surface is terminated with H and a dipole layer forms as a results of ionic C-H bonds and (c) when the surface is terminated with O and dipole layers with opposite sign compared to H is formed as a result of ionic O-H bonds. Note: compared to the clean surface the vacuum level and ionisation energy is lowered or raised with is termination by hydrogen or oxygen, respectively, by an amount of $e\Delta V$ where $e\Delta V$ is the potential step associated with two dipole layers of opposite sign [14].

It turns out that the lowering of the ionisation potential by the hydrogen termination is crucial for the *p*-type surface conductivity in diamond that forms spontaneously upon exposure to moist air. The resulting hole accumulation layer, which takes the form of a two-dimensional hole band, that is responsible for the surface conductivity that is at the heart of this thesis.

1.2.5 The Origin of Surface Conductivity in Diamond

In 1989, Landstrass and Ravi were the first to report an increase of conductivity from 10^{-16} $\Omega^{-1}cm^{-1}$ to 10^{-6} $\Omega^{-1}cm^{-1}$ for single-crystal CVD diamond following exposure of its surface to a hydrogen plasma [27]. Since then the origin of the surface conductivity has been controversially discussed. Shirafuji and Sugino suggested that the observed surface conductivity arises from a sub-surface hole accumulation layer [28]. In 2000, Maier *et al.* reported the role of atmospheric exposure, in addition to hydrogen termination, as a necessary condition for surface conductivity [6]. Maier *et al.* performed a crucial experiment by heating the hydrogen terminated diamond in UHV and measuring the conductivity *in situ*. They observed a reduction of the conductivity following annealing under vacuum at a temperature sufficient to remove the water layer that forms on the surface upon exposure to air, while the hydrogen termination remains intact. When subsequently exposed to air the surface conductivity was found to gradually recover. Therefore, they deduced that the hydrogen termination of the surface is not the sole cause of the observed surface conductivity; additional accepter species, present in air are also necessary to induce the conductance on the hydrogen terminated diamond [6]. The adsorbed water layer arising from air leads to the hole accumulation and band bending at the hydrogen terminated diamond surface, as illustrated in Figure 4 [6]. An electrochemical transfer doping model was developed by Maier *et al.* that elaborates the surface charge transfer that arises from an electrochemical redox reaction (equation 1) [6]. In this model electrons from the diamond are transferred to the water layer and neutralize the H^+ ions that are always present in water due to the partial dissociation of water into H^+ and OH^-. The remaining OH^- in the water layer form the surface acceptors. The electron transfer proceeds until the Fermi level in diamond and the electrochemical potential μ of the redox reaction come into equilibrium. Here, the lowering of the ionisation energy by hydrogen is a necessary condition for the electrochemical redox reaction to proceed, yielding the hole accumulation layer at the diamond surface [6].

$$Diamond + 2H_3O^+ + 2e^- \leftrightarrow Diamond^{2+(holes)} + H_2 + 2H_2O \quad (1)$$

Once this novel type of transfer doping was successfully described, other surface acceptors with high electron affinities were shown to induce transfer *p*-type doping on diamond as well. Strobel *et al.* demonstrated *p*-type surface doping using films of C_{60} [29, 30], Russel *et al.* showed surface doping with the transition metal oxide MoO_3 [31] and Verona *et al.* demonstrated that other metal oxides such as V_2O_5 can similarly be used as surface acceptors [32]. Transfer doping with these materials may, in principle, give higher p-type doping on account of their very high electron affinity, but they suffer from a lack of stability in air and during device fabrication. They may need to be immersed in deionised water during the device fabrication which, for instance, dissolves metal oxides such as MoO_3. As a result, the hole carrier densities achieved in fabricated devices doped with metal oxides is not considerably high than for the much simpler process of water-doping.

Edmonds *et al.* examined the electronic properties of C(100):H surface in response to doping with $C_{60}F_{48}$ molecules using high-resolution synchrotron based X-ray photoemission techniques. This permitted a detailed study of the energy level alignment at the C(100):H surface which unravelled details about the doping mechanism and the factors that determine the achievable hole carrier density [33]. Most significantly, a negative acceptor of -0.6 eV was observed, showing that the acceptor energy is below the valence band maximum [33]. This implies that transfer doping – in contrast to conventional bulk doping – does not requires an activation energy. Therefore, there should be no inherent reason why carrier freeze out would occur in surface conducting diamond samples at low temperature which is crucial for the low temperature magnetotransport measurements performed in this thesis.

For the work undertaken in this thesis, water-based doping was chosen rather than fullerene [33] or the recently studied metal oxides [32]. This is firstly on account of the simplicity of the device fabrication and secondly on account of the proven stability of hydrogen-terminated surfaces when exposed to water that permits reproducible hole densities to be maintained over long periods of time and at low temperatures.

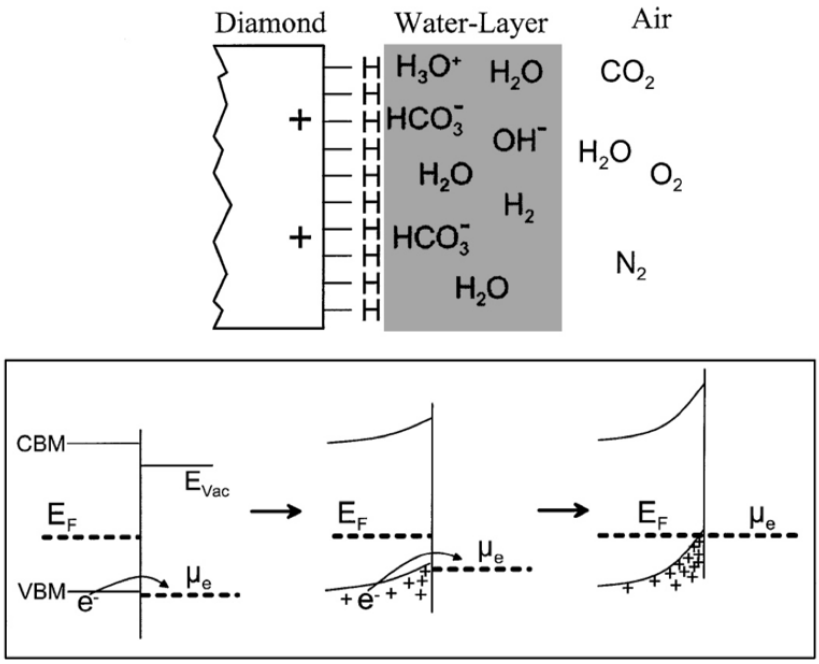

Figure 4: Top: Schematic image of the hydrogen terminated diamond surface in contact with water species in air. Bottom: The process of band bending change during the electron transfer doping at the diamond the water layer interface [6].

1.3 Surface Conducting Diamond Devices

To produce electronic devices, diamond heterocontacts with metals, insulators and in some cases, the addition of other semiconductors is required. The first Field Effect Transistor (FET) using surface conducting hydrogen-terminated diamond was reported by Kawarada *et al.* with a simple enhancement mode FET architecture [34]. In a metal-semiconductor (MES)-FET a robust pinch-off characteristic was demonstrated [35, 36]. In this architecture two ohmic contacts are formed using gold (Au) pads with an aluminium (Al) gate electrode on top of the hydrogen-terminated surface conducting channel. The Al layer forms a Schottky barrier in direct contact with the hydrogen-terminated diamond surface, leading to the complete depletion of the underlying hole channel in the absence of an applied gate bias. Surface conductivity is achieved with a positive applied gate bias.

In device applications using hydrogen terminated diamond a key requirement for satisfactory device operation is the formation of high quality metal-semiconductor interfaces on the hydrogen-terminated diamond surface. The electronic behaviour of metallic contacts on diamond is governed by the Schottky barrier height [36, 37]. Au contacts have a high work function (5.1 eV) and exhibit a very low Schottky barrier height

on hydrogen-terminated diamond, typically less than 0.2 eV [36, 37] and therefore they behave as ohmic contacts. Such contacts, formed using metals with high work function, are advantageous for creating source and drain contacts with low contact resistance in device architectures. In contrast, Al contacts have a low work function (4.3 eV), facilitating a higher Schottky barrier of typically 0.9 eV with on the hydrogen-terminated diamond surface. This makes Al suitable as a gate electrode [37], the high Schottky barrier possessing a low gate leakage. MESFET devices, using an Al gate electrode, have achieved the first high-frequency (GHz) transistor operation in a carbon-based semiconductor [38]. Following this development and through further improvements in the cut-off frequency, more advanced device architectures such as Metal-Insulator Semiconductor (MIS)-FET and Metal-Oxide Semiconductor (MOS)-FET devices operating at GHz frequencies have been explored [39-41].

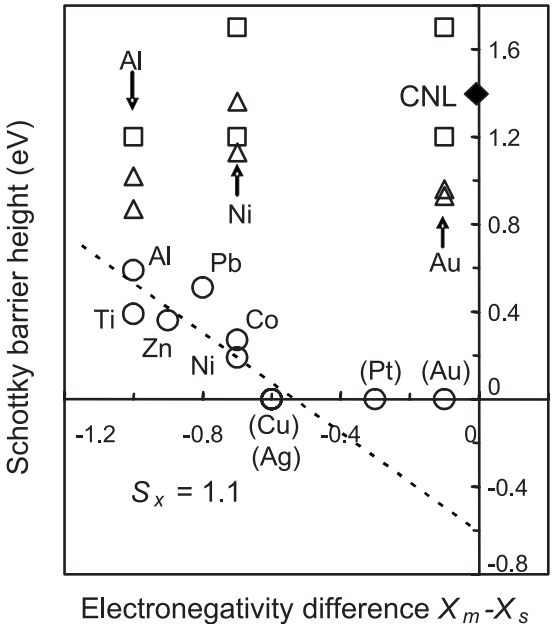

Figure 5: Schottky barrier height of different metal/diamond contacts as a function of the difference in electronegativity of the metal (χ_m) and diamond (χ_s). Open circles are data for metal/diamond (100) interfaces. Open squares and open tringles are the data for metal on oxygen terminated diamond (100) and (111) respectively. Note: the scale is in Pauling electronegativity [37].

Tsugawa *et al.* studied the relationship between the difference in electronegativity between the metal (χ_m) and diamond (χ_s) and the resulting Schottky barrier height at the metal-diamond interface [37]. Figure 5 illustrates the Schottky barrier height for diamond contacts formed using Au, Pt, Cu and Ag exhibit Ohmic behaviour and, in contrast, Al, Pb, Ti and Co contacts show strong Schottky characteristics. The Schottky barrier heights were explored for both hydrogen-terminated and oxygen-terminated diamond surfaces as

shown in the figure. For the case of hydrogen-terminated diamond, the Schottky barrier height depends almost linearly on the metal electronegativity (with slope factor S_x =1.1), whereas it is pinned at a barrier height of about 1.2 eV for the oxygen-terminated surface. [37].

As we shall show, superior devices with low contact resistance can be formed using palladium (Pd) contacts that were not explored by Tsugawa *et al.* Pd contacts on hydrogen-terminated diamond were first explored by Wang *et al.* in 2016 who showed that these contacts display Ohmic behaviour with a contact resistance of 1.8×10^{-6} Ωcm^2 that was measured on single-crystal diamond using a transmission line model [42]. Achieving a low contact resistance between electrodes and the diamond surface conducting channel is extremely important for low temperature studies since it permits the operation of devices with low excitation voltage. The adhesion of Au on the hydrogen-terminated diamond surface is quite poor, rendering fabrication of Ohmic Au contacts difficult. For this reason, several studies have shown the successful engineering of contacts using metals such as Ti and Pt as an adhesion layer prior to Au deposition [43-46]. However, achieving a very low contact resistance with these metals requires a high temperature annealing process to form a titanium-carbide interface [47], however the removal of carbide from the surface for the purpose of recycling diamond substrates is difficult. The study by Wang *et al.* has shown Pd to be an excellent Ohmic contact material for diamond device applications by demonstrating low contact resistances of Pd on hydrogen-terminated diamond as a result of Schottky barrier height (0.15 eV) [42]. Pd contacts are additionally thermally stable with no carbide formation nor degradation of the Ohmic properties observed on sample annealing [42].

An alternative and very effective way of gating surface conducting devices is to utilise electrolyte-based gates which additionally have several important applications within the rapidly growing area of biological sensing devices [48]. Araki *et al.* developed the first solution-gate devices on a hydrogen-terminated diamond [48]. In this device architecture, the diamond surface is immersed in an aqueous solution (the electrolyte) and the conductivity at the diamond surface may be modulated using a gate electrode to change the electric potential at the electrolyte/diamond interface [48-50]. Figure 6 shows this mechanism schematically, illustrating the effect of electrolyte gating on the surface potential relative to the case of an air-induced surface doping. In the air-doped case, charge transfer at the interface is responsible for the surface conductivity and there is

thermodynamic equilibrium expressed by the equality between the Fermi energy E_F and the electrochemical potential of the relevant redox couple, the $O_2\ /OH^-$ ions in this case. This equilibrium is achieved through a balance of charge transfer and the resulting band bending. In contrast, as shown in Figure 6b, in the absence of charge transfer the Fermi energy E_F may be tuned by the potential between the diamond surface and the reference electrode (Ag/AgCl); this potentiostat alters the thermodynamic equilibrium. When a negative potential, U_G is applied to the gate electrode, E_F is shifted below the valence band maximum leading to an enhancement of the hole carrier density at the diamond and electrolyte interface. On other hand, when a positive voltage is applied to the gate, the hole accumulation will diminishes as E_F is pushed above the valence band maximum [49]. In both cases, the potential in the water or electrolyte layer is referenced to the vacuum level. As such, the negative electron affinity of the diamond surface crucially influences the position of E_F relative to the valence band maximum at the surface.

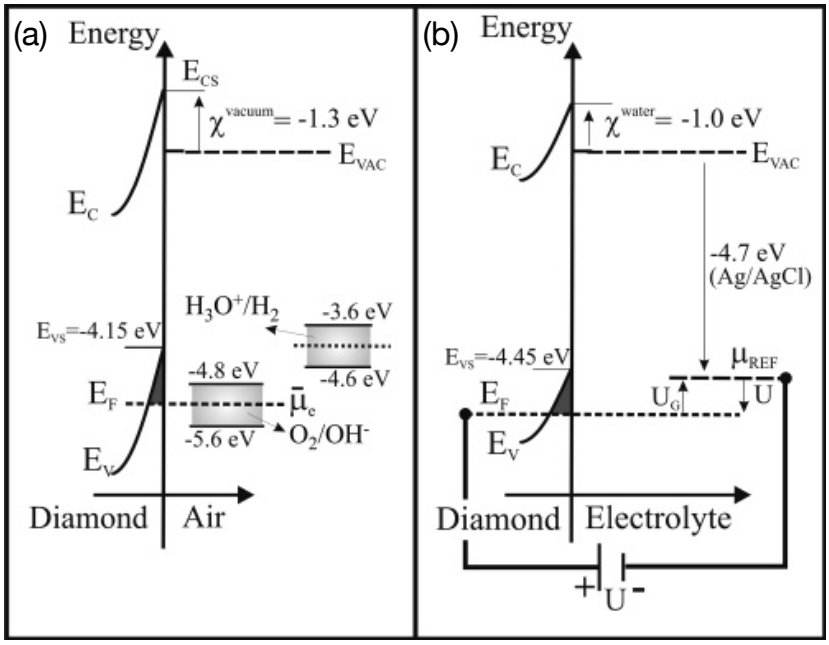

Figure 6: Energy band diagram illustrating (a) the interface between diamond and air with diamond electron affinity $\chi = -1.3\ eV$ and (b) the interface between diamond and electrolyte with $\chi = -1.0\ eV$ [49].

As mentioned earlier, in comparison to the air-doped situation, charge transfer may have no influence on hole accumulation when the device is immersed in a suitable electrolyte (such as the 10 mM potassium based phosphate buffer solution with additional 50 mM NaCl utilsied in [51]). In this case capacitive polarisation causes the change in Fermi level and hence hole accumulation at the diamond-electrolyte interface [49, 51-53]. Figure 7

shows the dependence of carrier density to the gate voltage under the electrolyte potential control [51]. This figure confirms the linear relationship between the gate bias and carrier density and the interfacial capacitance of 2 $\mu F cm^{-2}$ is deduced from the slope of this relationship [51]. The resulting hole carrier density can be measured using standard Hall effect measurements.

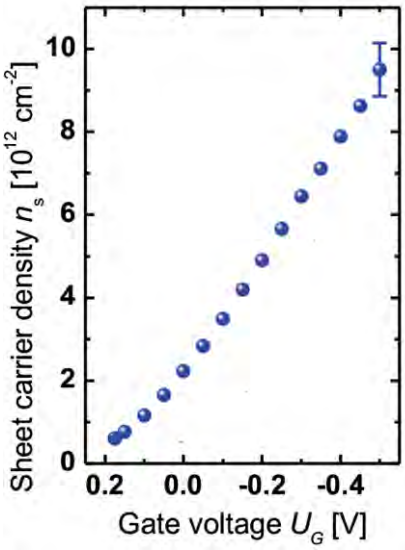

Figure 7: Sheet carrier density as a function of gate voltage. From the linear slope an interfacial capacitance of 2 $\mu F cm^{-2}$ is deduced [51].

It is also important to consider hydrophobic interactions as the value of the interfacial capacitance is also affected by the condition of the hydrogen-terminated surface. The hydrophobic nature of this surface is known to create fluctuations in the dielectric constant as a result of fluctuations in water density when it is air doped [51, 52, 54].

Moreover, there exist several other solutions in addition to electrolytes that can be used to create solution-gated devices such as ionic liquids, ion gels and solid electrolyte. The physics and principle of operation of these solutions are similar to the electrolyte case but their chemistry, stability and achievable capacitance differ considerably [50, 55-57]. In general, the advantage of these approaches is in their simplicity; an electrolyte-gated FET architecture does not require a solid-state gate oxide as is required for MOSFETs and MISFETs, so that fabrication is more straightforward. Moreover, thanks to a combination of chemical and physical properties, electrolyte-gated FETs on diamond have shown great potential in bioelectronics and biosensing applications [52, 58-61]. For instance,

solution-gated diamond has been used to create device arrays in order to record electrogenic cell action potentials [60]. Also, enzyme-based sensors and DNA-hybridization have been reported using the sensing capability of the combination of hydrogenated diamond and electrolytes [59, 62].

1.4 Transport Properties of Surface Conducting Diamond

There have been several studies of the transport properties of surface conducting diamond, primarily focused on understanding the temperature dependence of hole carrier density and mobility. Until recently, transport measurements have shown an exponential reduction in the hole density as the temperature is lowered as a result of carrier freeze. By performing Hall effect measurements as a function of temperature, Nebel *et al.* reported the temperature dependence of the mobility and hole density, and suggested that the observed exponential reduction in density (Figure 8(a)) most likely arises from high surface disorder leading to hopping between localised states [63]. Disorder induced localised states in a narrow hole accumulation layer at the edge of the valence band were considered to be a consequence of poor hydrogenation or surface roughness [63]. The carrier freeze-out was observed below a critical temperature of about 70 K as a result of carriers being trapped in these localised states. Nebel *et al.* used a classical mobility-edge model to describe the transport mechanism in which above the critical temperature carriers are mobile in extended states [63-65].

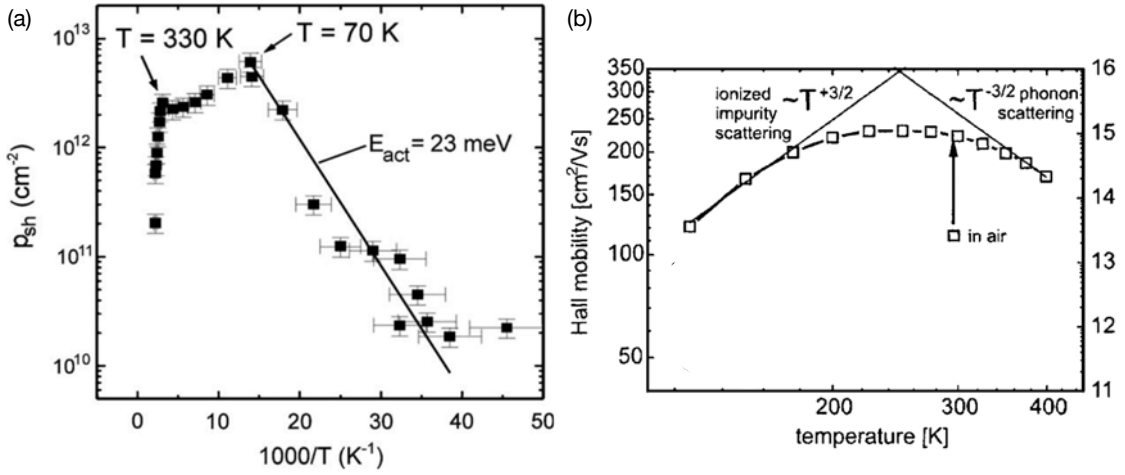

Figure 8: (a) Hole sheet densities as a function temperature measured from 20-400 K. According to Nebel et al. holes get localised in trap states below the critical temperature of 70 K [65].(b) Hall mobility as a function of temperature, demonstrating low mobility as a result of charged impurity scattering due to the ionised surface scattering [66].

Garrido *et al.* also studied the properties of holes in the conducting channel of a hydrogen terminated sample by performing Hall effect measurements at temperatures between 30 to 300 K [67]. They also observed the exponential dependence of conductivity on temperature [67], however, they adopted a different model to describe the temperature dependence of the localised carriers based upon the activated transport through the device. Using this model, the metallic conductivity and mobility, the effective fraction of the surface which is insulating, and the average potential barrier between metallic regions were determined by fitting the experimental results [67].

As discussed earlier, the fact that the acceptor energy relevant to surface transfer doping is negative [34] implies that carrier freeze-out should not be an inherent property of the surface doped hole accumulation layer in diamond. However, for many years the carrier freeze-out in disorder induced localised states has limited the opportunity to study the transport properties of the hole accumulation layer at low temperature but recent improvements in the quality of CVD diamond surfaces have made available single-crystal samples with low surface disorder in which conductivity can be maintained at cryogenic temperatures. This has opened a new avenue of research into the quantum transport properties of the hole accumulation layer. Yamaguchi *et al.* demonstrated the evolution of insulating to metallic conduction at cryogenic temperatures [68]. This is done by modulating the hole carrier density on surface conducting diamond with the use of the ionic liquid gating technique. The sub-surface hole band reported in this work was found to remain metallic at low temperature, demonstrating, for the first time, that a high surface conductivity could be maintained; consistent with the report of the negative acceptor energy in this system [68]. Figure 9 illustrates the metallic behaviour at temperatures as low as 400 mK with the ionic liquid gate achieving modulation of the hole density at these temperatures (although noting that the temperature would have to be raised in order to vary the gate bias). These experiments were performed using single crystal CVD diamonds with both (100) and (111) oriented surfaces [68]. The (111) oriented surface shows a slightly higher density compared to the (100) oriented diamond surface at the same gate bias; this can be due to the difference in C^{-}–H^{+} dipole density between the two surface orientations. The hydrogen-terminated (100) oriented diamond forms a 2×1 surface reconstruction while the (111) surface is not reconstructed [69].

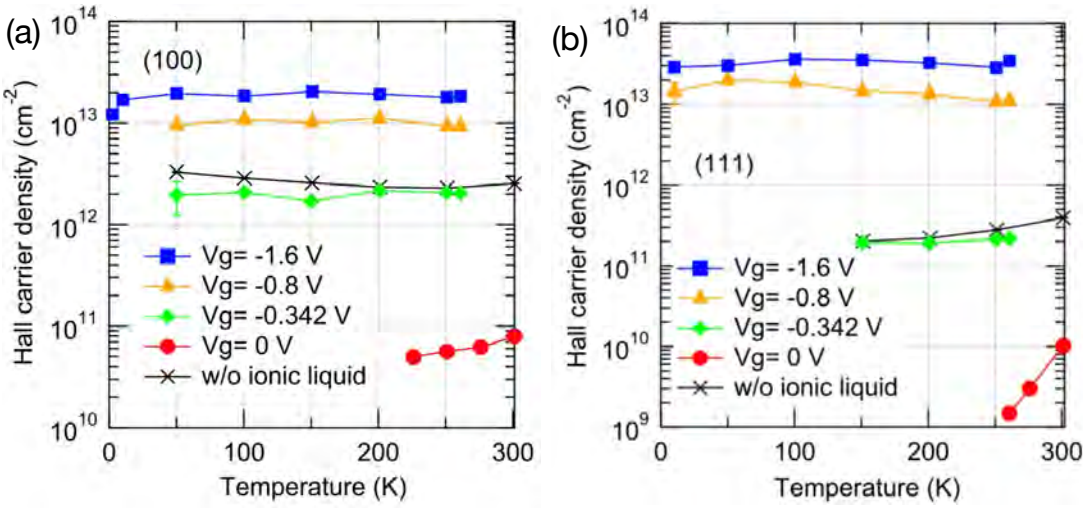

Figure 9: Temperature dependence of hole carrier density as function of temperature at different gate voltages (a) single crystalline diamond with (100) surface and (b) (111) surface [68].

Only within the last few years have the low-temperature transport studies of surface conducting diamond been extended to consider the response to a variable applied magnetic field. As we shall show, magnetotransport is a powerful experimental tool that can inform the dimensionality and spin transport properties of the hole band in the accumulation layer of diamond. During 2014, three different studies of the dimensionality of the diamond hole band were published, all three confirming the hole band to be two-dimensional [7, 70, 71].

Firstly, Hauf *et al.* fabricated an in-plane gated device on a hydrogen-terminated surface conducting diamond and, by using the gates to confine the channel to the nanometre scale, observed Coulomb blockade effects in the transport through the channel at low temperature [71]. By monitoring the separation in gate bias of Coulomb blockade peaks, they determined the capacitance of islands of charge within the channel; electrostatic modelling suggested that the corresponding islands must be 2, similar to the behaviour of other 2D systems [72-74].

Secondly, Takahide *et al.* claimed the hole band on hydrogen-terminated (111) diamond to be 2D by interpreting quantum oscillations in the magnetotransport as a signature of the Shubnikov-de Haas effect [70]. Shubnikov-de Haas oscillations can be observed in a 2D system with sufficiently high carrier mobility. In the case of Takahide *et al.*, the hole mobility ($\mu = 91$ cm^{2}V^{-1}s^{-1}) was typical of that measured in surface conducting diamond and too low to observe Shubnikov-de Haas oscillations directly. Instead, they inferred the

presence of oscillations from peaks in the fourier spectrum of the differential resistance, suggesting that while the mobility is too low to support the Shubnikov-de Haas effect on the macroscopic scale [70].

Finally, Edmonds *et al.* explored the dimensionality and spin transport in the surface conducting channel of a Hall bar device on hydrogen-terminated (100) diamond by performing magnetotransport measurements at low temperature [7]. These measurements revealed quantum coherent transport in the form of weak localization (WL) and weak anti-localization (WAL) which give rise to characteristic signatures in the magnetoconductance close to B = 0 T, with the WAL becoming more prominent as the temperature was lowered. By fitting the magnetoconductance curves to quantum transport theory, two important conclusions were drawn from this work. Firstly, from the temperature dependence of the phase coherence length the 2D nature of the hole band was unequivocally confirmed. Secondly, the presence of WAL suggested that the 2D hole band possesses a strong spin-orbit coupling, which was determined by fitting the measured magnetoconductance curves to Dresselhaus (bulk inversion asymmetry) and Rashba (structural asymmetry of the triangular confining potential) theories. A spin-orbit coupling strength of hydrogen terminated diamond in reference [7] was determined which is significantly higher than in other 2D hole systems [8, 9] and comparable to, for example, the value obtained for hydrogen-terminated graphene [75]. In principle, as we shall explain in Section 1.5, in a quantum-confined well the spin-orbit coupling can be substantially larger than that of bulk material due to the Rashba mechanism. For bulk diamond, the atomic spin-orbit splitting of its valence electrons is only $\Delta_{atomic} = 8$ meV on account of its low atomic number [76]. It is interesting to note that the spin-orbit coupling determined by Edmonds *et al.* does not exceed this value but, as we shall show in Chapter 3 by gating the device with an ionic liquid we can substantially increase the spin-orbit interaction via the Rashba mechanism.

Edmonds *et al.* found that both the Dresselhaus and Rashba models fitted the experimental data adequately and similar parameters were extracted for each model [7]. However, the paper is focused on the Dresselhaus model and the inversion asymmetry, required for the Rashba model, could only be due to the surface of the diamond not the diamond bulk which has inversion symmetry.

As we discuss later in this thesis (Chapter 2), the Rashba effect is the most likely cause of the high spin-orbit coupling in surface conductivity diamond as a result of the very highly asymmetric quantum well created by the near-surface band bending; this can be maintained due to the high breakdown field in diamond. We show that by gating a surface conducting diamond Hall bar using an ionic liquid it is possible to tune the spin orbit coupling over a five-fold range by imposing a variable hole sheet density, and through the Poisson equation, electric field, at the surface. This adds strength to the argument that the observed strong spin-orbit coupling arises from the Rashba effect at the exclusion of the Dresselhaus mechanism.

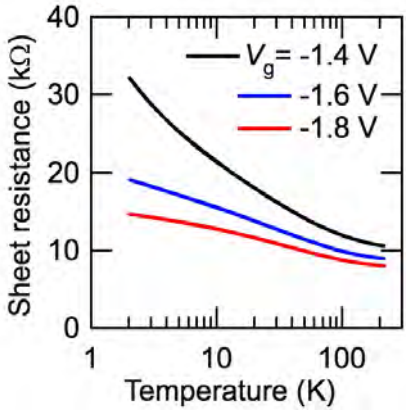

Figure 10: Sheet resistance as a function of temperature and gate bias determined by Takahide et al. [77].

Also worth mentioning is a recent study of magnetotransport in surface conducting diamond by Takahide *et al.* [77]; here magnetotransport measurements where undertaken using an ionic liquid gated diamond device at low temperatures with strength and direction of an applied magnetic field varied [77]. This paper reported a magnetoresistance that is independent of the magnetic field direction which is rather surprising and unexpected for a 2D system. It is interesting to note that Takahide *et al.* did not measure the magnetotransport for bare (water-doped) diamond Hall bar in the absence of an ionic liquid. This may indicate that the resistivity of the devices is higher than those examined by Edmonds *et al.* and in this thesis, perhaps due to a low carrier density for their ungated device and more disordered surface giving rise to a degree of charge carrier freeze-out at low temperature. If this is the case, Takahide's sample may be operating in a non-metallic regime which would be consistent with the temperature dependence of the sheet resistivity that they obtained as shown in Figure 10. In-plane magnetotransport measurements are important because, as we shall show in Chapter 4, the contrasting behaviour between the magnetoconductance in the presence of

perpendicular and in-plane magnetic fields allows us to probe Zeeman splitting in the hole band and to extract the gyromagnetic ratio.

In this thesis, we fabricate high-quality surface conducting Hall bar devices and show that the 2D hole band maintains metallic behaviour down to cryogenic temperatures without the need for electrostatic gating using an oxide dielectric gate or ionic liquid solution. Magnetotransport measurements were performed systematically in the presence of an in-plane magnetic field to gain more information about the spin properties of holes in this system. We show that the gyromagnetic ratio and micro-roughness of the 2D hole channel can be extracted, and further explore the effect on the in-plane magnetotransport of ionic liquid gating. To understand the significance and utility of these measurements in probing the spin properties of 2D materials, we first review a series of magnetotranport studies in related 2D electron and hole systems.

1.5 Spin-orbit Coupling Effects in Related Two-dimensional Materials

Spin-orbit coupling is a relativistic effect that couples the spin of an electron or hole to its orbital movement. It results in a splitting of atomic energy levels with non-vanishing orbital angular momentum. The magnitude of the splitting increases with the atomic number of the element involved. As a consequence, the spin-orbit coupling is strongest in compound semiconductor materials with at least one heavy component such as InSb or GaSb and its alloys [78]. Quasi-two dimensional systems based upon these materials have band structures that are well-suited to the study of quantum coherent transport and for spintronic applications that rely on the presence of a high spin orbit coupling.

Spin orbit coupling has been widely studied for quantum wells and nanowires and subsequently exploited in the development spin field effect transistors, or spin-FETs [79-83]. Much of this work has focused on 2D electron systems and there are fewer reports of spin-orbit effects in 2D hole systems [7-9, 84]. This is because the spin-orbit coupling in hole systems tends to be smaller than in electron systems. However, in 2D systems there are extrinsic mechanisms which enhance the spin-orbit coupling in the case of both electrons and holes. They operate when the inversion symmetry perpendicular to the 2D plane is broken. In that case, one obtains a spin-orbit interaction that depends on an odd power of the wavevector k of the charge carriers. There are two mechanisms that act to enhance the spin-orbit interaction in this way. The Dresselhaus effect depends on a

structural breaking of the inversion symmetry such as in zinc-blende crystal structures and it scales linearly with k [85]. The Rashba effect relies on an extrinsic breaking of the inversion symmetry [85] due, for example, to the presence of a highly asymmetric confinement potential as in the case of the confinement of holes near the surface of hydrogen-terminated diamond. The strength of the Rashba effect scales with the carrier wavevector, with both k and k^3 terms [8, 9, 86, 87]. It turns out that for holes, as in our case, only the k^3 term is present [88]. More detail about the k and k^3 terms in Rashba and Dresselhaus theories is discussed in Chapter 2.

Low-field magnetotransport measurements, in which a magnetic field is applied perpendicular to the plane of a material, are a very powerful tool for the study of the spin properties of 2D electronic materials. The magnetoresistance is influenced by quantum coherent backscattering in the form of weak localization (WL), which gives rise to a negative magnetoresistance in the vicinity of B = 0 T, and weak anti-localization (WAL) which creates a characteristic cusp in the magnetoresistance at B = 0 (Figure 11). The mechanisms that cause these effects will be explained in detail in the next chapter. The presence of WAL reveals a strong spin-orbit coupling and analysis of magnetoconductance curves can inform the magnitude of this interaction. WAL has been very extensively studied from a theoretical perspective, with important contributions by Bergmann and Pikus [89-91]. These studies include a description of heterostructured systems with low carrier mobility in which transport occurs in a diffusive regime which is relevant to the case of surface conducting diamond. Diffusive transport occurs when charge carriers undergo frequent elastic scattering events resulting in a small mean free path and where the applied magnetic field is much smaller than a characteristic transport field, which is defined in the next chapter [90].

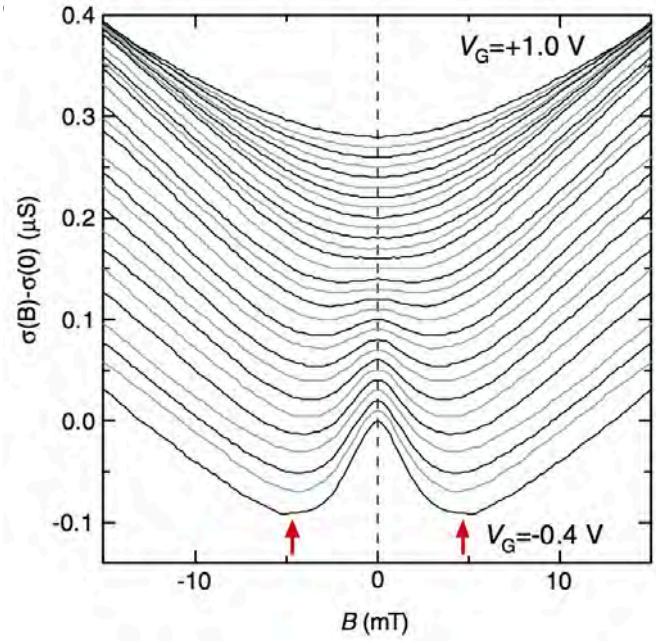

Figure 11: The change of Magnetoconductance in strained Ge quantum wells as a function at gate voltage at 1.6 K. Demonstrating the change from WL to WAL by sweeping from $V_G = +1\ V$ to $V_G = -0.4\ V$ [8].

Moreover, spin properties can also be explored by preforming measurements using magnetic fields tilted with respect to the plane of the 2D quantum well. This technique opens new possibilities for investigation because the perpendicular field component affects the orbital motion whereas the in-plane field component couples mostly to the carrier spin. In-plane fields are known to destroy WAL through the Zeeman interaction, interface microroughness and orbital mixing [13]. Therefore, by applying an additional in-plane magnetic field the effect of the Zeeman interaction on the weak anti-localization can be systematically explored and the in-plane gyromagnetic ratio can be determined. As Cabanas and others have discussed [11, 12, 92] an in-plane field can affect the spin transport in a 2D system in a number of ways. In this thesis we shall discuss in detail the effects that arise from both perpendicular and in-plane magnetotransport on hydrogenated diamond devices.

References:

1. Iijima, S., *Helical microtubules of graphitic carbon.* Nature, 1991. **354**(6348): p. 56.
2. Hayden, O., R. Agarwal, and W. Lu, *Semiconductor nanowire devices.* Nano Today, 2008. **3**(5-6): p. 12-22.
3. Novoselov, K.S., et al., *Electric field effect in atomically thin carbon films.* science, 2004. **306**(5696): p. 666-669.
4. Krasnozhon, D., et al., *MoS_2 transistors operating at gigahertz frequencies.* Nano letters, 2014. **14**(10): p. 5905-5911.
5. Lopez-Sanchez, O., et al., *Ultrasensitive photodetectors based on monolayer MoS_2.* Nature nanotechnology, 2013. **8**(7): p. 497.
6. Maier, F., et al., *Origin of surface conductivity in diamond.* Physical review letters, 2000. **85**(16): p. 3472.
7. Edmonds, M.T., et al., *Spin–Orbit Interaction in a Two-Dimensional Hole Gas at the Surface of Hydrogenated Diamond.* Nano letters, 2014. **15**(1): p. 16-20.
8. Moriya, R., et al., *Cubic rashba spin-orbit interaction of a two-dimensional hole gas in a strained-Ge/SiGe quantum well.* Physical review letters, 2014. **113**(8): p. 086601.
9. Morrison, C., et al., *Observation of Rashba zero-field spin splitting in a strained germanium 2D hole gas.* Applied Physics Letters, 2014. **105**(18): p. 182401.
10. Awschalom, D.D. and M.E. Flatté, *Challenges for semiconductor spintronics.* Nature Physics, 2007. **3**(3): p. 153-159.
11. Minkov, G., et al., *Weak antilocalization in quantum wells in tilted magnetic fields.* Physical Review B, 2004. **70**(15): p. 155323.
12. Glazov, M. and L. Golub, *Spin–orbit interaction and weak localization in heterostructures.* Semiconductor Science and Technology, 2009. **24**(6): p. 064007.
13. Meijer, F., et al., *Competition between spin-orbit interaction and Zeeman coupling in Rashba two-dimensional electron gases.* Physical Review B, 2004. **70**(20): p. 201307.
14. Sussmann, R.S., *CVD diamond for electronic devices and sensors*. Vol. 26. 2009: John Wiley & Sons.
15. Madelung, O., *Semiconductors: data handbook*. 2012: Springer Science & Business Media.
16. Wandelt, K., *Surface and interface science Vol 2: Properties of Elemental Surfaces.* 2012.
17. Balmer, R., et al., *Unlocking diamond's potential as an electronic material.* Philosophical Transactions of the Royal Society of London A: Mathematical, Physical and Engineering Sciences, 2008. **366**(1863): p. 251-265.
18. Okushi, H., et al., *Device-grade homoepitaxial diamond film growth.* Journal of crystal growth, 2002. **237**: p. 1269-1276.
19. Ri, S.-G., et al., *Misorientation angle dependence of surface morphology in homoepitaxial diamond film growth at a low CH4/H2 ratio.* Journal of crystal growth, 2002. **235**(1-4): p. 300-306.
20. May, P.W., *Diamond thin films: a 21st-century material.* Philosophical Transactions of the Royal Society of London A: Mathematical, Physical and Engineering Sciences, 2000. **358**(1766): p. 473-495.
21. Schenk, A., et al., *High resolution core level spectroscopy of hydrogen-terminated (1 0 0) diamond.* Journal of Physics: Condensed Matter, 2016. **28**(30): p. 305001.
22. Frauenheim, T., et al., *Stability, reconstruction, and electronic properties of diamond (100) and (111) surfaces.* Physical Review B, 1993. **48**(24): p. 18189.

23. Jing, Z. and J. Whitten, *Ab initio studies of H chemisorption on C (100) surface.* Surface science, 1994. **314**(2): p. 300-306.
24. Himpsel, F., et al., *Quantum photoyield of diamond (111)—A stable negative-affinity emitter.* Physical Review B, 1979. **20**(2): p. 624.
25. Cui, J., J. Ristein, and L. Ley, *Electron affinity of the bare and hydrogen covered single crystal diamond (111) surface.* Physical Review Letters, 1998. **81**(2): p. 429.
26. Maier, F., J. Ristein, and L. Ley, *Electron affinity of plasma-hydrogenated and chemically oxidized diamond (100) surfaces.* Physical Review B, 2001. **64**(16): p. 165411.
27. Landstrass, M. and K.V. Ravi, *Resistivity of chemical vapor deposited diamond films.* Applied Physics Letters, 1989. **55**(10): p. 975-977.
28. Shirafuji, J. and T. Sugino, *Electrical properties of diamond surfaces.* Diamond and Related Materials, 1996. **5**(6-8): p. 706-713.
29. Strobel, P., et al., *Surface transfer doping of diamond.* Nature, 2004. **430**(6998): p. 439.
30. Strobel, P., et al., *Surface transfer doping of diamond by fullerene.* Diamond and related materials, 2005. **14**(3-7): p. 451-458.
31. Russell, S.A., et al., *Surface transfer doping of diamond by MoO3: A combined spectroscopic and Hall measurement study.* Applied Physics Letters, 2013. **103**(20): p. 202112.
32. Verona, C., et al., *Comparative investigation of surface transfer doping of hydrogen terminated diamond by high electron affinity insulators.* Journal of Applied Physics, 2016. **120**(2): p. 025104.
33. Edmonds, M., et al., *Surface transfer doping of hydrogen-terminated diamond by C60F48: Energy level scheme and doping efficiency.* The Journal of chemical physics, 2012. **136**(12): p. 124701.
34. Kawarada, H., M. Aoki, and M. Ito, *Enhancement mode metal-semiconductor field effect transistors using homoepitaxial diamonds.* Applied physics letters, 1994. **65**(12): p. 1563-1565.
35. Itoh, M. and H. Kawarada, *Fabrication and characterization of metal-semiconductor field-effect transistor utilizing diamond surface-conductive layer.* Japanese journal of applied physics, 1995. **34**(9R): p. 4677.
36. Kawarada, H., *Hydrogen-terminated diamond surfaces and interfaces.* Surface Science Reports, 1996. **26**(7): p. 205-259.
37. Tsugawa, K., et al., *Schottky barrier heights, carrier density, and negative electron affinity of hydrogen-terminated diamond.* Physical Review B, 2010. **81**(4): p. 045303.
38. Taniuchi, H., et al., *High-frequency performance of diamond field-effect transistor.* IEEE Electron Device Letters, 2001. **22**(8): p. 390-392.
39. Hirama, K., et al. *High-performance p-channel diamond MOSFETs with alumina gate insulator*. in *Electron Devices Meeting, 2007. IEDM 2007. IEEE International*. 2007. IEEE.
40. Matsudaira, H., et al., *Over 20-GHz cutoff frequency submicrometer-gate diamond MISFETs.* IEEE Electron Device Letters, 2004. **25**(7): p. 480-482.
41. Pakes, C.I., J.A. Garrido, and H. Kawarada, *Diamond surface conductivity: Properties, devices, and sensors.* MRS Bulletin, 2014. **39**(6): p. 542-548.
42. Wang, W., et al., *Palladium ohmic contact on hydrogen-terminated single crystal diamond film.* Diamond and Related Materials, 2015. **59**: p. 90-94.
43. Zhen, C., et al., *Ohmic contacts to boron-doped diamond.* Optical Materials, 2003. **23**(1-2): p. 117-121.

44. Robinson, J.A., et al., *Contacting graphene.* Applied Physics Letters, 2011. **98**(5): p. 053103.
45. Nakanishi, J., et al., *Formation of ohmic contacts to p-type diamond using carbide forming metals.* Journal of applied physics, 1994. **76**(4): p. 2293-2298.
46. Jingu, Y., K. Hirama, and H. Kawarada, *Ultrashallow TiC source/drain contacts in diamond MOSFETs formed by hydrogenation-last approach.* IEEE Transactions on Electron Devices, 2010. **57**(5): p. 966-972.
47. Zhen, C., et al., *Au/p-diamond ohmic contacts deposited by RF sputtering.* Applied Surface Science, 2008. **255**(5): p. 2916-2919.
48. Kawarada, H., et al., *Electrolyte-Solution-Gate FETs Using Diamond Surface for Biocompatible Ion Sensors.* physica status solidi (a), 2001. **185**(1): p. 79-83.
49. Garrido, J.A., et al., *The surface conductivity at the diamond/aqueous electrolyte interface.* Journal of the American Chemical Society, 2008. **130**(12): p. 4177-4181.
50. Dankerl, M., et al., *Solid polyelectrolyte-gated surface conductive diamond field effect transistors.* Applied Physics Letters, 2012. **100**(2): p. 023510.
51. Dankerl, M., et al., *Hydrophobic interaction and charge accumulation at the diamond-electrolyte interface.* Physical review letters, 2011. **106**(19): p. 196103.
52. Dankerl, M., et al., *Diamond solution-gated field effect transistors: Properties and bioelectronic applications.* physica status solidi (a), 2012. **209**(9): p. 1631-1642.
53. Garrido, J.A., et al., *The diamond/aqueous electrolyte interface: an impedance investigation.* Langmuir, 2008. **24**(8): p. 3897-3904.
54. Sedlmeier, F., et al., *Water at polar and nonpolar solid walls.* Biointerphases, 2008. **3**(3): p. FC23-FC39.
55. Ignat'ev, N., et al., *New ionic liquids with tris (perfluoroalkyl) trifluorophosphate (FAP) anions.* Journal of Fluorine Chemistry, 2005. **126**(8): p. 1150-1159.
56. Raymundo-Pinero, E., et al., *Relationship between the nanoporous texture of activated carbons and their capacitance properties in different electrolytes.* Carbon, 2006. **44**(12): p. 2498-2507.
57. Kim, S.H., et al., *Electrolyte-Gated Transistors for Organic and Printed Electronics.* Advanced Materials, 2013. **25**(13): p. 1822-1846.
58. Bergveld, P., J. Wiersma, and H. Meertens, *Extracellular potential recordings by means of a field effect transistor without gate metal, called OSFET.* IEEE Transactions on Biomedical Engineering, 1976(2): p. 136-144.
59. Härtl, A., et al., *Enzyme-modified field effect transistors based on surface-conductive single-crystalline diamond.* Langmuir, 2008. **24**(17): p. 9898-9906.
60. Dankerl, M., et al., *Diamond transistor array for extracellular recording from electrogenic cells.* Advanced functional materials, 2009. **19**(18): p. 2915-2923.
61. Zhou, Y.L., R.H. Tian, and J.F. Zhi, *Amperometric biosensor based on tyrosinase immobilized on a boron-doped diamond electrode.* Biosensors and Bioelectronics, 2007. **22**(6): p. 822-828.
62. Song, K.-S., et al., *Label-free DNA sensors using ultrasensitive diamond field-effect transistors in solution.* Physical review E, 2006. **74**(4): p. 041919.
63. Nebel, C., et al., *Low temperature properties of the p-type surface conductivity of diamond.* Diamond and related materials, 2002. **11**(3-6): p. 351-354.
64. Nebel, C., et al., *Hydrogen-induced transport properties of holes in diamond surface layers.* Applied physics letters, 2001. **79**(27): p. 4541-4543.
65. Nebel, C., B. Rezek, and A. Zrenner, *Electronic properties of the 2D-hole accumulation layer on hydrogen terminated diamond.* Diamond and Related Materials, 2004. **13**(11-12): p. 2031-2036.

66. Rezek, B., H. Watanabe, and C. Nebel, *High carrier mobility on hydrogen terminated⟨100⟩ diamond surfaces.* Applied physics letters, 2006. **88**(4): p. 042110.
67. Garrido, J., T. Heimbeck, and M. Stutzmann, *Temperature-dependent transport properties of hydrogen-induced diamond surface conductive channels.* Physical Review B, 2005. **71**(24): p. 245310.
68. Yamaguchi, T., et al., *Low-Temperature Transport Properties of Holes Introduced by Ionic Liquid Gating in Hydrogen-Terminated Diamond Surfaces.* Journal of the Physical Society of Japan, 2013. **82**(7): p. 074718.
69. Sque, S., R. Jones, and P. Briddon, *Structure, electronics, and interaction of hydrogen and oxygen on diamond surfaces.* Physical review B, 2006. **73**(8): p. 085313.
70. Takahide, Y., et al., *Quantum oscillations of the two-dimensional hole gas at atomically flat diamond surfaces.* Physical Review B, 2014. **89**(23): p. 235304.
71. Hauf, M.V., et al., *Low dimensionality of the surface conductivity of diamond.* Physical Review B, 2014. **89**(11): p. 115426.
72. Beenakker, C. and H. van Houten, *Quantum transport in semiconductor nanostructures*, in *Solid state physics*. 1991, Elsevier. p. 1-228.
73. Sols, F., F. Guinea, and A.C. Neto, *Coulomb blockade in graphene nanoribbons.* Physical Review Letters, 2007. **99**(16): p. 166803.
74. Gallagher, P., K. Todd, and D. Goldhaber-Gordon, *Disorder-induced gap behavior in graphene nanoribbons.* Physical Review B, 2010. **81**(11): p. 115409.
75. Balakrishnan, J., et al., *Colossal enhancement of spin–orbit coupling in weakly hydrogenated graphene.* Nature Physics, 2013. **9**(5): p. 284.
76. Kuemmeth, F., et al., *Coupling of spin and orbital motion of electrons in carbon nanotubes.* Nature, 2008. **452**(7186): p. 448.
77. Takahide, Y., et al., *Spin-induced anomalous magnetoresistance at the (100) surface of hydrogen-terminated diamond.* Physical Review B, 2016. **94**(16): p. 161301.
78. Winkler, R., et al., *Spin-Orbit Coupling in Two-Dimensional Electron and Hole Systems*. Vol. 41. 2003: Springer.
79. Akabori, M., et al., *Realization of In0. 75Ga0. 25As two-dimensional electron gas bilayer system for spintronics devices based on Rashba spin-orbit interaction.* Journal of Applied Physics, 2012. **112**(11): p. 113711.
80. Chuang, P., et al., *All-electric all-semiconductor spin field-effect transistors.* Nature nanotechnology, 2015. **10**(1): p. 35.
81. Koo, H.C., et al., *Control of spin precession in a spin-injected field effect transistor.* Science, 2009. **325**(5947): p. 1515-1518.
82. Kum, H., et al., *Electric field control of magnetoresistance in a lateral InAs quantum well spin valve.* Applied Physics Letters, 2009. **95**(21): p. 212503.
83. Nitta, J., et al., *Gate Control of Spin-Orbit Interaction in an Inverted I n 0.53 G a 0.47 As/I n 0.52 A l 0.48 As Heterostructure.* Physical Review Letters, 1997. **78**(7): p. 1335.
84. Hu, B., et al., *High mobility two-dimensional hole system on hydrogen-terminated silicon (111) surfaces.* Applied Physics Letters, 2012. **100**(25): p. 252107.
85. Schäpers, T., *Semiconductor Spintronics*. 2016: Walter de Gruyter GmbH & Co KG.
86. Nakamura, H., T. Koga, and T. Kimura, *Experimental evidence of cubic Rashba effect in an inversion-symmetric oxide.* Physical review letters, 2012. **108**(20): p. 206601.
87. Winkler, R., et al., *Spin orientation of holes in quantum wells.* Semiconductor science and technology, 2008. **23**(11): p. 114017.

88. Ma, T. and Q. Liu, *Spin Hall conductance of the two-dimensional hole gas in a perpendicular magnetic field.* Physical Review B, 2006. **73**(24): p. 245315.
89. Bergmann, G., *Weak localization in thin films: a time-of-flight experiment with conduction electrons.* Physics Reports, 1984. **107**(1): p. 1-58.
90. Knap, W., et al., *Weak antilocalization and spin precession in quantum wells.* Physical Review B, 1996. **53**(7): p. 3912.
91. Pikus, F. and G. Pikus, *Conduction-band spin splitting and negative magnetoresistance in A 3 B 5 heterostructures.* Physical Review B, 1995. **51**(23): p. 16928.
92. Cabañas, S., et al., *Suppression of weak antilocalization in an $Al_xGa_{1-x}N$/Ga N two-dimensional electron gas by an in-plane magnetic field.* Physical Review B, 2007. **75**(19): p. 195329.

2

Experimental Details and Theory

2.1 Introduction

This chapter details the device fabrication and measurement techniques on hydrogen terminated diamond used throughout this study. The goal of this chapter is to outline the basic principles of Hall bar and solution-gated Hall bar fabrication techniques. Magnetotransport measurements and instruments are described and the techniques that were used to determine the properties of the two-dimensional hole band at the hydrogen terminated are discussed. The theoretical detail and methods that were used to characterise fabricated devices throughout this thesis are also explained.

2.2 Diamond processing and hydrogen termination

For all experiments in this thesis commercial single crystal type-IIa (100) diamonds from Element Six Ltd. were used. All samples were acid etched by boiling diamonds in a mixture of sulphuric acid (1 ml) and sodium nitrate (0.25 ml) for 30 minutes prior to hydrogen termination to ensure non-carbon phases and metallic contamination were removed. Subsequently, the diamonds were rinsed in de-ionised water to remove residual acid. Following the acid treatment samples were hydrogen terminated in a high-power microwave plasma (iPLAS Cyrannus CVD reactor) using a plasma power of 1500-1700

W and hydrogen pressure of 80 Torr at 850 °C for 10 minutes. After samples were cooled to room temperature they were exposed to ambient air with normal humidity for several days in order to facilitate charge transfer doping via redox reactions with the adsorbed water layer which results in a *p*-type conducting surface.

2.3 Device Fabrication

Hall bars with two different length scales were fabricated: with a length/width of 320 μm/40 μm (Device A) and with a length/width of 200 μm / 40 μm (Device B). Standard photolithography and lift-off techniques were used to define the hydrogen terminated Hall bars and metal contacts, employing mask alignment and electron-beam evaporation systems. Each of the steps is described in detail below.

2.3(a). Photolithography mask design and exposure

Patterning of a device on a diamond coated with photoresist is achieved using a photomask made from a square glass slide in which the device design is reproduced in opaque chromium patterns but is otherwise transparent to ultraviolet (UV) light. The chrome mask was designed using an AutoCAD software application and commercially fabricated by the Research and Prototype Foundry in Sydney, Australia [1]. Photomasks can be either light-field or dark-field masks. A light-field mask is a mask with dark patterns and dark-field mask is a mask with clear patterns. The figure below shows both light and dark field masks that were used to fabricate all devices in this thesis.

Photolithographic exposure of the samples through the mask was performed using a Neuronix Quinted Q4000-6 mask aligner with ultraviolet light of wavelength $\lambda \cong 0.2\mu m - 0.4\mu m$. This tool is widely used in photolithography processing and in this work was used to define alignment markers, hydrogen-terminated Hall bars and metal contacts through multiple processing steps. It is therefore important to have accurate and reproducible alignment of the photolithographic mask to the sample for each step of the multilayer fabrication process. This was achieved by incorporating into the mask design several metal alignment markers that were engineered at the first fabrication step and used to ensure that subsequent patterns were perfectly aligned through all fabrication steps.

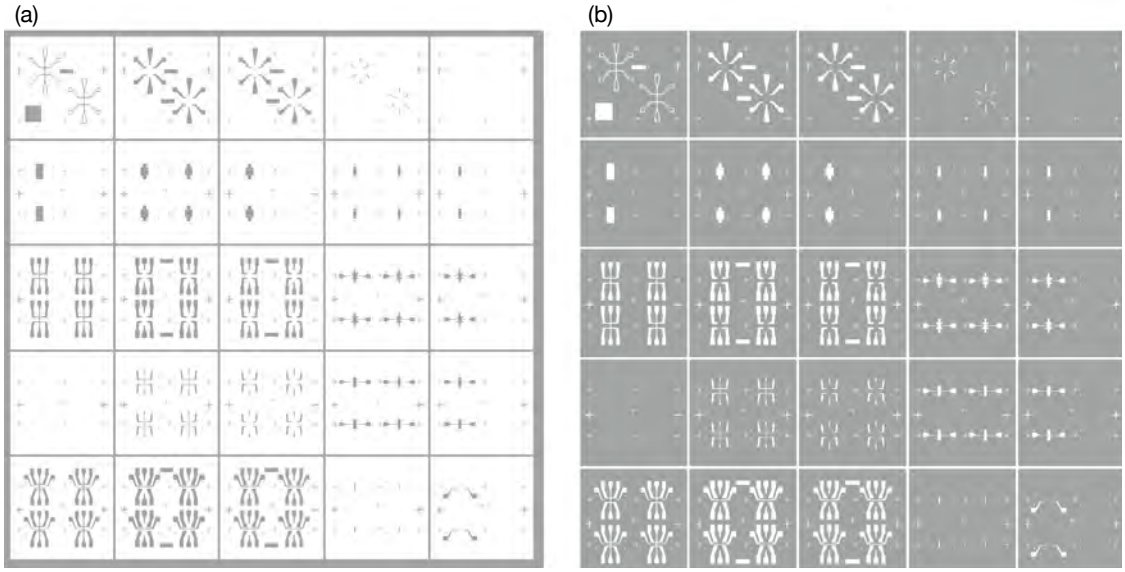

Figure 12: Chrome masks used in photolithography process. (a) light-field mask and (b) dark-field mask.

2.3(b). Photoresist

The first step in any photolithography process involves dispensing onto the sample an organic polymer (photoresist) that is sensitive to UV radiation. For the small diamonds used here, the samples were held in a silicone mould and placed on the sample plate of a spin coater system. A vacuum chuck holds the silicone mould in place during operation of the coater. The use of the mould aids the adhesion of the sample to the sample plate and additionally reduces the effect of beading in which the solution collects at the edge, resulting in greater the thickness of photoresist on the order of ten times compared to the centre. The silicone mould was formed using Sylgard 184 silicone elastomer base mixed with Sylgard 184 silicone curing agent in a ratio of 10:1.

To ensure the uniformity of photoresist across the sample and remove any contamination in the coating solvent, samples were soft-baked on a hotplate after spin coating and before patterning of the devices. Soft-baking also improves the hardness of the photoresist which leads to an increase in the photoresist resistance to the following steps.

Two types of photoresist were used in the experiments reported in this thesis: positive tone (AZ1514H) and negative tone (AZnlof2020) photoresists. A positive tone photoresist, AZ1514H, was used to create Device A. Exposing the positive photoresist to UV light causes scission of polymer chains through a photochemical reaction, weakening the polymer and rendering it soluble [2]. Subsequent chemical development solution

dissolves only the exposed regions of photoresist, thus selectively etching the exposed region and creating normal or overcut sidewalls depending on UV exposure dose and developing time (Figure 13c).

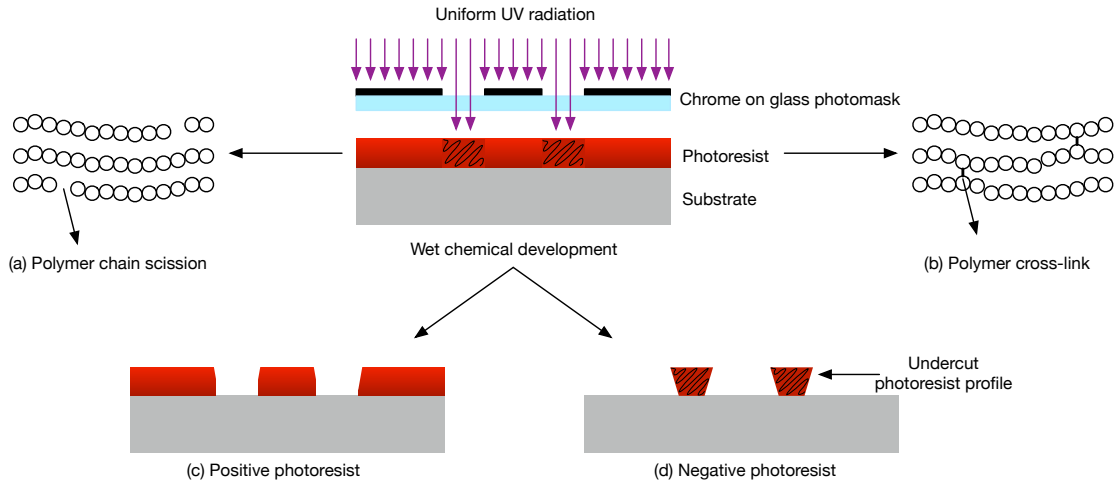

Figure 13: UV exposure, pattern transfer and development. (a) Exposed positive photoresist (polymer chain scission). (b) Exposed negative photoresist (polymer cross-link). (c) Positive photoresist profile. (d) Negative photoresist profile.

The negative tone photoresist AZnlof2020 was used to fabricate Device B. In a negative tone resist UV light causes cross-linking of the exposed polymer chains and reduces the solubility rate [2]. Therefore, only the areas that have not been exposed to UV radiation are selectively etched by a developing solution and undercut sidewalls are created (Figure 13d). Post exposure baking is an additional step that is required after UV exposure and before the chemical development step when a negative tone photoresist is used as it is necessary to drive the cross-linking mechanism induced during UV exposure.

2.3(c). Oxygen Termination

A Diener oxygen plasma system is used for a mild oxygen plasma treatment in the fabrication of Hall bars. This technique is used for two purposes; firstly, it is used to remove any unwanted photoresist that is left behind after the development process, thus improving the metal adhesion to the surface [3]. Secondly, it is used to define hydrogen-terminated Hall bars by oxygen terminating regions surrounding each Hall bar pattern [3].

2.3(d). Metal deposition by electron beam evaporation

The deposition of metal components on the diamond substrates is achieved by electron beam evaporation and lift-off. The electron beam evaporator is a thin film deposition tool that can be used to evaporate a range of different materials in a high-vacuum environment; in this case a Thermionics Electron Beam Evaporation system was used. A schematic diagram illustrating the function of the system is shown in
Figure 14. The sample is placed over the water-cooled hearth that contains the metal to be deposited. A high energy electron beam, generated by a heated filament, is magnetically focused onto the metal in the crucible, which melts and is deposited onto the sample. The advantage of this system is the low degree of contamination compared to the other thermal evaporation methods [2]. This arises because while the material in the crucible is directly heated the crucible itself remains cooled by the hearth. This technique is also advantageous for lift-off processes because the evaporated material does not cover the sidewalls of photoresist layers, although this of course depends upon the relative location of the metal source and substrate.

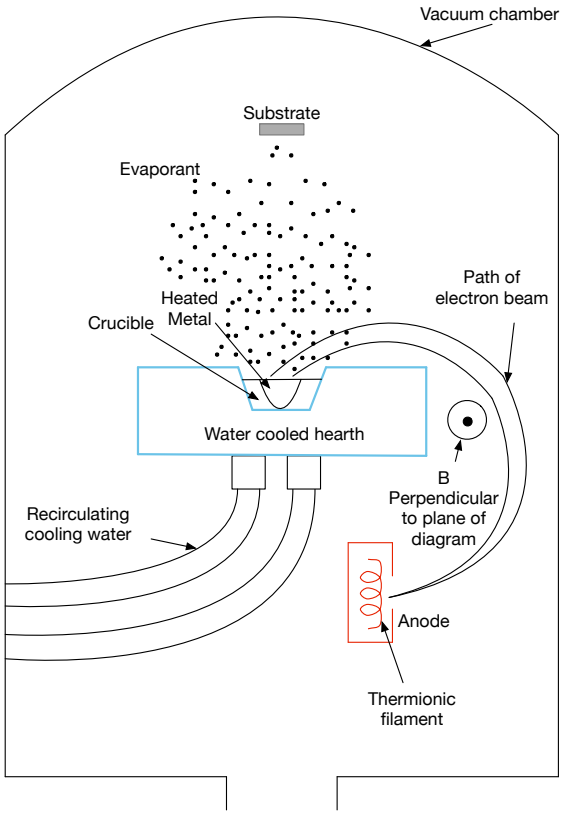

Figure 14: Schematic diagram of electron-beam evaporation system illustrating magnetised deflection of electron beam.

2.3(e). Lift-off process for positive and negative photoresists

Lift-off is one of the key patterning techniques in microfabrication that has been very extensively applied to a broad range of applications. Lift-off is performed by via mild agitation of a sample in acetone until unwanted adlayers, in this case metals, on top of a lithographically patterned photoresist layer are peeled off. The lift-off process usually takes about 30-40 minutes using a positive tone photoresist and about 10-15 minutes for a negative tone photoresist due to the difference in their photoresist profiles.
Figure *15* shows the lift-off process applied to positive and negative resists. For the case of a positive photoresist, overcut sidewalls of the photoresist can give rise to metal regions retaining wings at edges after the lift-off process. This can be problematic particularly if gate dielectrics and subsequently deposited since the metal wing can punch through the dielectric material. In contrast, the under-cut photoresist profile that is typically seen for negative photoresists both leads to a quicker lift-off process and results in a retrograde profile that is more applicable for device applications.

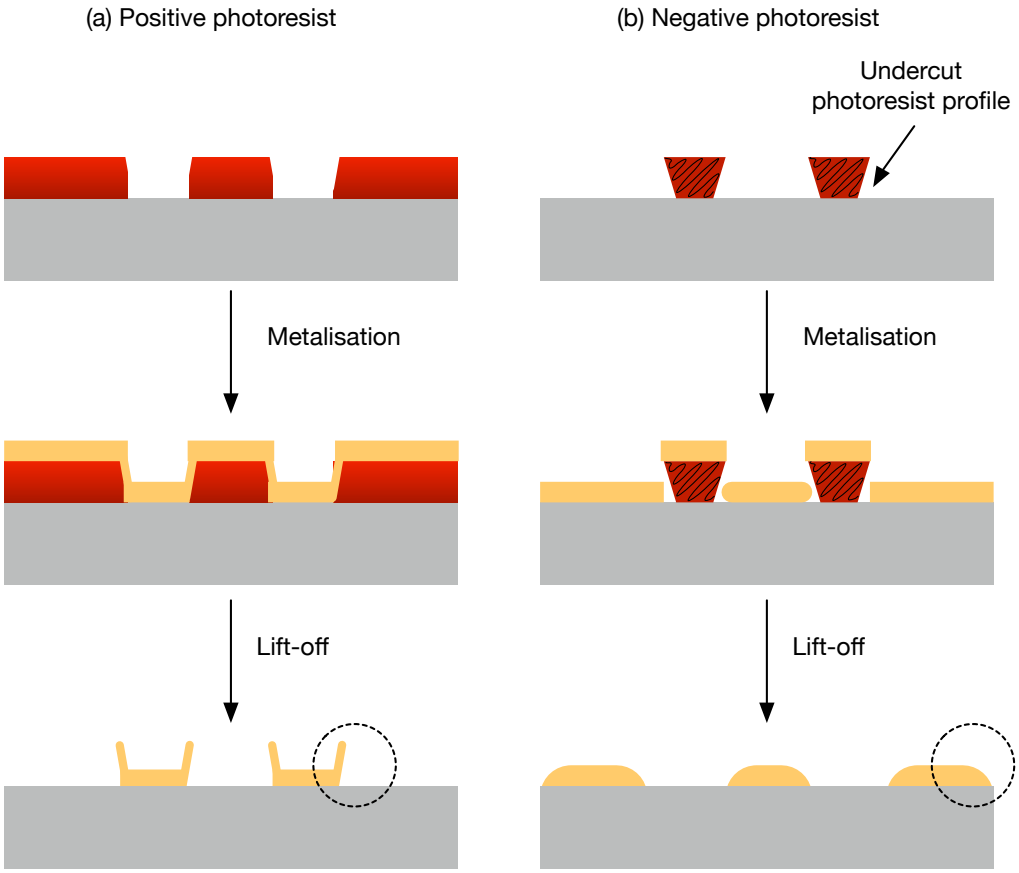

Figure 15: Lift-off profile. (a) Positive photoresist. (b) Negative photoresist.

2.3(f). Device processing

During the course of this project a large number of devices where fabricated and tested which is typical of a new device fabrication protocol. The results presented in Chapters

3-5 are based upon two device architectures that employed different photolithography mask designs and fabrication procedures.

In each case, prior to commencing device fabrication, alignment markers were fabricated as they are necessary for multilayer photolithography steps to achieve the desirable alignment of each device layer.

The fabrication steps for processing Titanium/Gold (10/20 nm) alignment markers is shown schematically in Figure 16 along with a photograph of a sample with alignment markers in place ready for device processing.

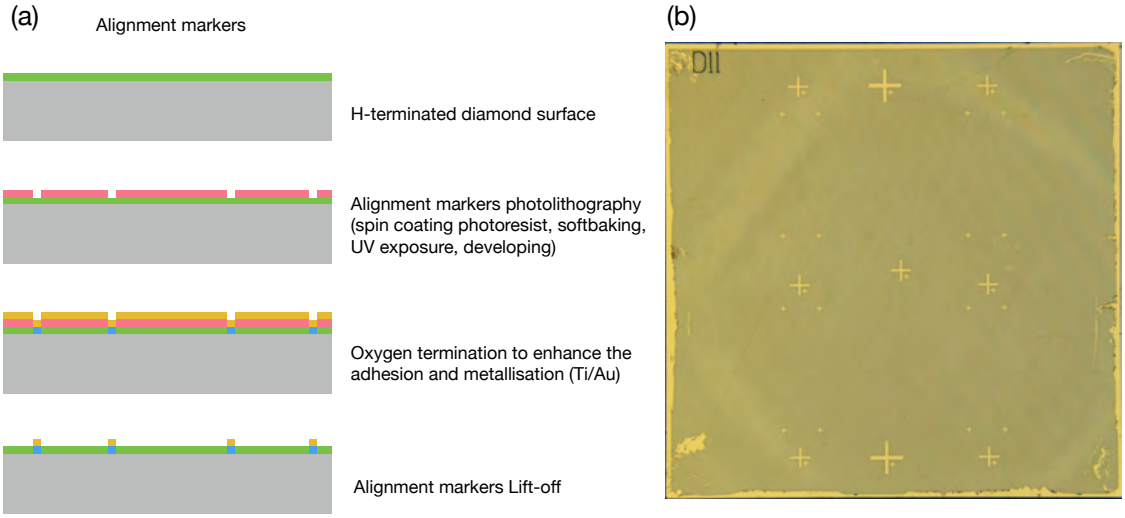

Figure 16: Alignment markers. (a) Fabrication steps. (b) Optical image of fabricated alignment markers based upon Ti/Au contacts.

Device A was the first device type that was engineered in this thesis; the lay-out is shown in Figure 18. The length and width of the Hall bar channel are $320\,\mu m$ and $40\,\mu m$ respectively, producing a channel of 8 squares. A positive photoresist, AZ1514H, was used for the fabrication. The photolithographic process steps used to pattern metal contacts on Device A are summarised as follows:

- This photoresist was dropped onto a hydrogen-terminated diamond surface in a silicon mould located on the resist spinner and spun at 4000 rpm for 60 seconds.
- The diamond was removed from the silicone mould and soft-baked at 100 °C for 60 seconds to dry the photoresist. This results in a photoresist thickness of approximately 1.4 µm.

- The sample was exposed to UV light for 13 seconds through a photomask
- The sample was soaked in a AZ826MIF developer solution for 30 seconds and then rinsed with deionised water.
- A sequence of Titanium/Platinum/Gold (10/10/100 nm) evaporation was used to create metal contacts. The titanium layer serves as an adhesion layer on the diamond surface and an additional platinum layer is used to improve the adhesion between titanium and the gold bond pad [4].

The fabrication steps for Device A are illustrated schematically in Figure 17 and the photographs of complete devices are shown in Figure 18. Device A was used in the experiments described in Chapter 3 which utilised an ionic liquid gate to tune the hole carrier density and spin orbit interaction in the Hall bar channel.

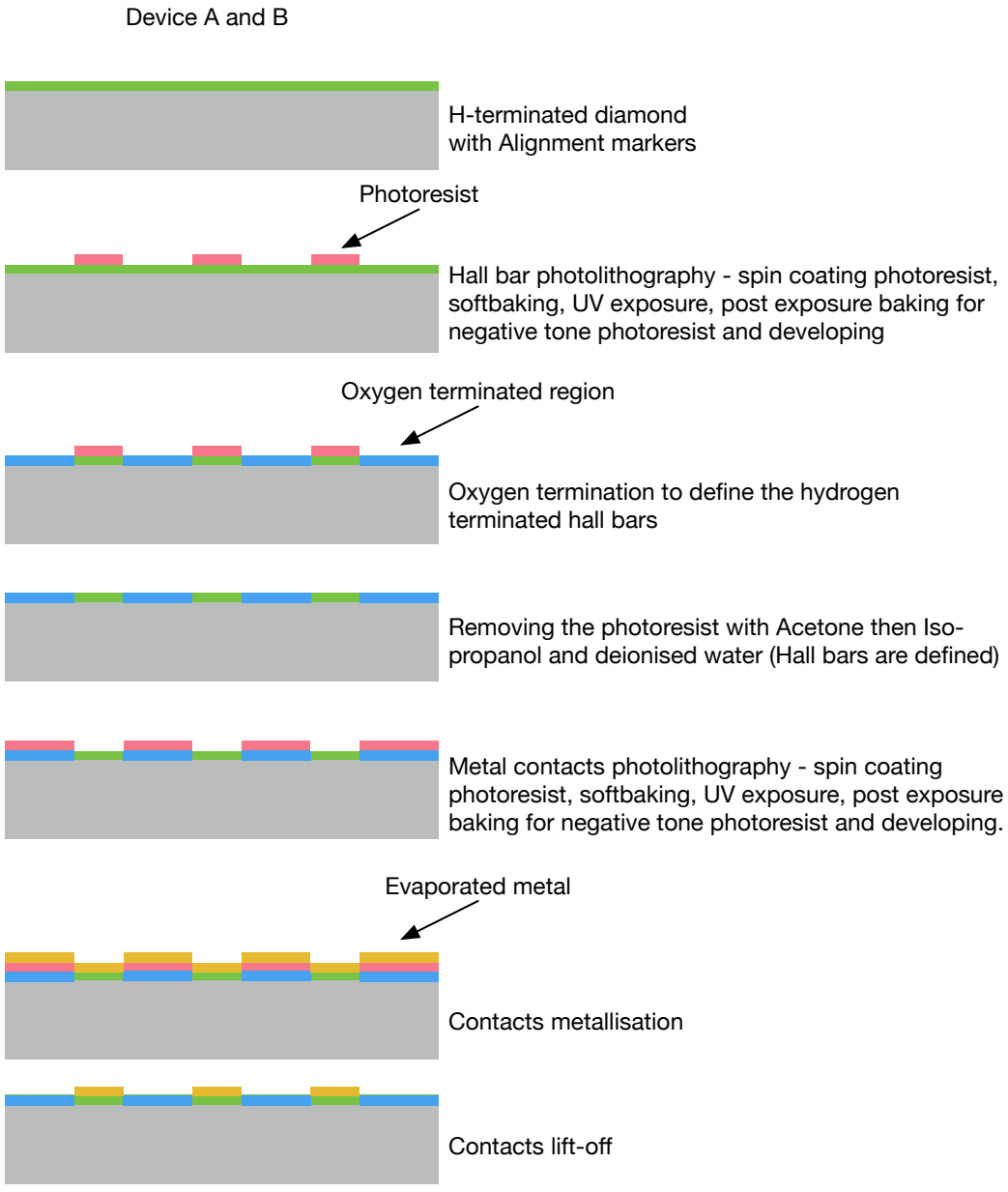

Figure 17: Steps of Hall bar device fabrication.

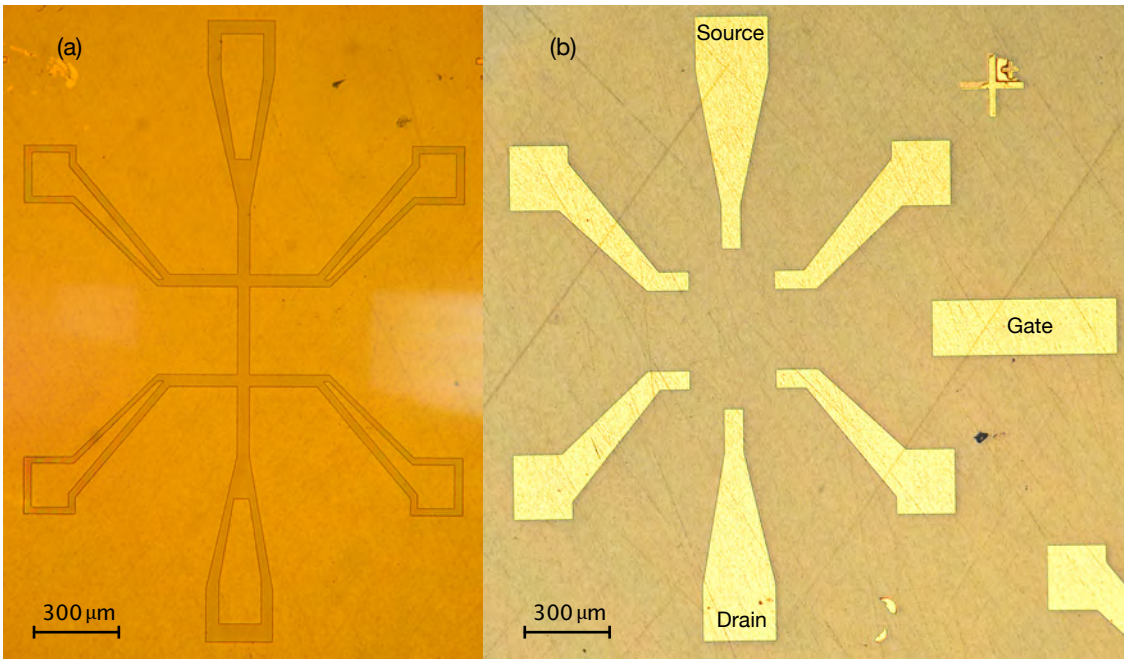

Figure 18: Optical images of Device A. (a) Definition of Hall bar; the dark regions are covered with photoresist and remain hydrogen terminated upon oxygen plasma processing and the light region is oxygen terminated region. (b) After evaporated Ti/Pt/Au contacts on hydrogen terminated Hall bar and gate electrode which is separated from the hall bar channel by the oxygen terminated surface.

Device B was developed later in the project and offers a number of improvements. In addition, it was fabricated using a negative photoresist, AZnlof2020. The photolithographic process steps used to pattern metal contacts on Device B are summarised as follows:

- The photoresist was spun at 4000 rpm for 60 seconds and soft-baked at 100 °C for 60 seconds which leads to a photoresist thickness of 1.7 µm.
- Post UV exposure baking is also performed as it is required for the cross-linking mechanism; then the substrate is soaked in AZ826MIF developer solution for 30 seconds and rinsed in deionised water.
- For Device B Palladium (150 nm) contacts were developed and found to give a much improved contact resistance on the hydrogen terminated diamond surface compared to the Ti/Pt/Au contacts [5]. The contacts were additionally corrugated at the edges to improve adhesion to the surface and to increase the number of holes in the diamond below the contacts. The fabrication steps for Device B of fabrication are demonstrated in Figure 17 and Figure 19. Device B was used in

the experiments described in Chapters 4 and 5 in which the g-factor in the 2D hole band and microroughness of the surface confinement potential are probed.

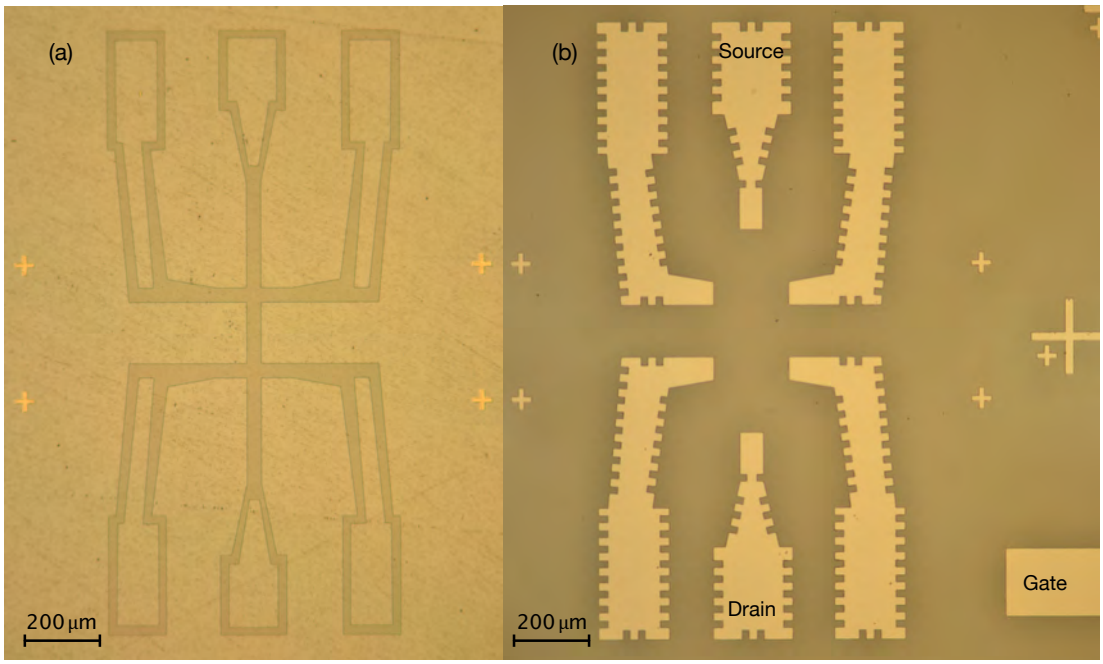

Figure 19: Optical images of Device B. (a) Defined hall bar; dark region covered photoresist i.e. hydrogen terminated, and light region is oxygen terminated region. (b) After evaporated Pd contacts on hydrogen terminated hall bar and gate contact is separated from the channel by oxygen terminated region.

2.3(g). Device Packaging

For measurement purposes fabricated devices were glued into a standard 20-pin chip carrier (
Figure *20*). Gold bond wires were bonded between each device and the chip carrier using a Hesse Mechatronics ultrasonic wire bonder based at the University of Melbourne.

Figure 20: Chip carrier and wire bonding. Diamond samples were glued into the chip carrier using epoxy and contacts are wire bonded.

2.3(h). Ionic liquid as a gate dielectric

The FAP-based ionic liquid 1-ethyl-3-methyl-imidazolium tris(pentafluoroethyl) trifluorophosphate $[C_2C_1Im]^+[FAP]^-$ was used to gate both devices [6]. The ionic liquid was used on account of its high dielectric constant and low leakage current. After wire bonding, a small volume of ionic liquid was dropped onto the device using a micropipette, coating both the Hall ball channel and a nearby gate electrode (
Figure *21*). Ions in the ionic liquid are mobile at temperatures above about 236 K and move in response to a bias applied to the gate electrode [6]. At lower temperatures the ionic motion is frozen and an electric field induced in the liquid can be retained once the electrode bias is removed. This allows the hole carrier density to be easily tuned by simply elevating the temperature of the device to change the gate bias.

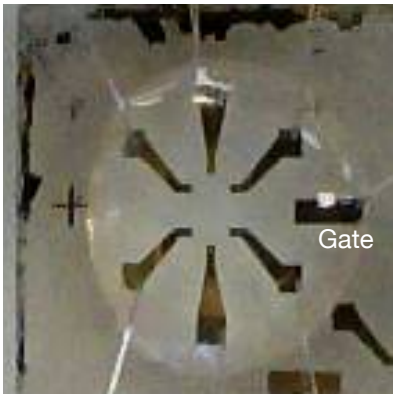

Figure 21: Ionic liquid gated device. Gated Hall bar (device A) using Ionic liquid that connect the gate electrode to the channel.

2.4 Magnetotransport measurements – cryogenic systems

Extensive magnetotransport measurements were performed at low temperature and in high magnetic fields (applied both perpendicular and parallel to the diamond surface) to understand spin transport in the 2D hole channel. Two different cryogenic systems were used in this thesis. Device A was measured using a liquid helium cooled Oxford Instruments Heliox ^{3}He Refrigerator located at the University of New South Wales, which is equipped with 2 T superconducting magnet. Device B was measured using a Leiden Cryogenics cryogen-free dilution refrigerator equipped with a 9-1-1 T superconducting vector magnet based at the University of Melbourne.

2.4(a). Oxford Instrument Heliox ^{3}He refrigerator

The Oxford Instruments Heliox ^{3}He refrigerator is a sorption pumped ^{3}He system with a base temperature of 250-300 mK. Device A was mounted in a chip carrier socket on the bottom of the measurement probe (
Figure *22*a) that is connected directly to the ^{3}He pot.
Figure 23 shows the principle of operation of a ^{3}He refrigerator. The Heliox system is designed to operate in a 'wet' cryostat consisting of a liquid ^{4}He storage dewar with integrated superconducting magnet for performing magnetotransport measurements. The Heliox system has an inner vacuum chamber (IVC) that creates thermal isolation of the 1K pot and ^{3}He pot from the higher temperature liquid ^{4}He in the storage dewar, as shown in
Figure 23.

Figure 22: a) Picture of the end of the Heliox system, showing the 1K pot, and sample mount directly connected to the ^{3}He pot. (b) Picture of the Heliox fridge fully inserted into the liquid ^{4}He dewar next to the rack of measurement electronics.

The Heliox system consists of a charcoal sorption pump whose very large surface area efficiently adsorbs large amounts of gas when cooled below 40 K. The sorption pump is charged with several litres of ^{3}He gas and the system is allowed to cool to 4.2 K by immersing the probe in the liquid helium dewar. Using the internal heater of the sorption pump to bring the charcoal sorb above 40 K, the gaseous ^{3}He is released and liquefied by the 1 K pot [7]. The 1 K pot draws liquid helium from the main dewar through a pickup tube and needle valve, and is vacuum pumped in order to reduce its temperature to

between 1-2 K [7]. When all of the ^{3}He has been condensed by this cold stage into the ^{3}He pot, the sorption pump heater is turned off and the sorb is again allowed to cool below 40 K where it acts as a high efficiency vacuum pump [7]. As the sorption pump evacuates the volume above the now liquefied ^{3}He, the reduction in vapour pressure causes the liquid to cool to as low as 250 mK. By adjusting the sorption pump temperature with a temperature controller, we can effectively control the pumping efficiency on the ^{3}He vapour and thus the temperature of the sample. This system has been used to measure Device A with an ionic liquid gate at temperatures from 250 mK to 20 K. Weak anti-localization and weak localization effects were observed during these experiments, and we have demonstrated that we can tune the localization effects and therefore the spin-orbit interaction using an ionic liquid as a gate. The complete results of these experiments are summarised in Chapter 3.

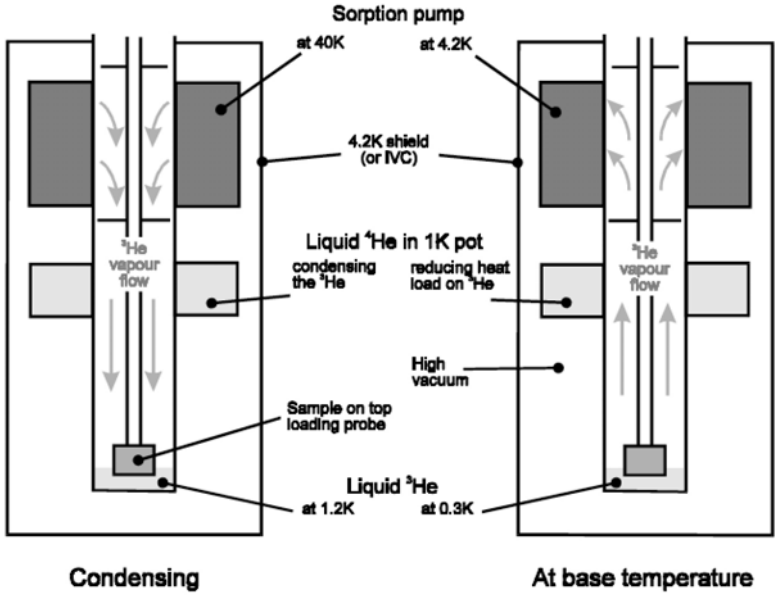

Figure 23: Principle of Heliox operation and its working parts [7].

2.4(b). Leiden Cryogenics dry dilution refrigerator

A Leiden Cryogenics dry dilution refrigerator based at the University of Melbourne has been used to undertake the magnetotransport experiments described in Chapters 4 and 5. The system, pictured in
Figure *24*, is a ^{3}He/^{4}He refrigerator with integrated 9-1-1 T superconducting magnet (up to 9T vertically and 1T in mutually orthogonal directions horizontally), and is operated 'dry' by a pulse tube cryocooler rather than being immersed in liquid helium. The base

temperature of the dilution refrigerator is 20 mK, and the sample temperature can be controlled up to 20 K for magnetotransport measurements.

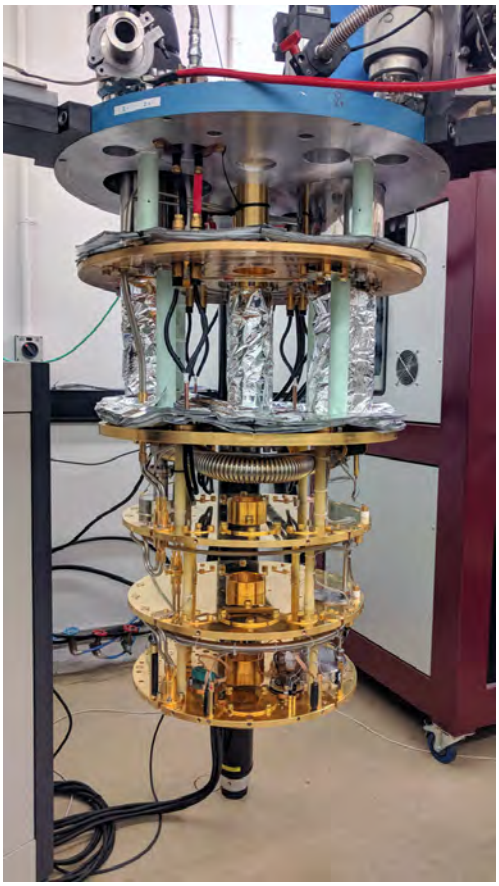

Figure 24: Leiden Cryogenics dry dilution refrigeration at the University of Melbourne.

The system operates using a mixture of two helium isotopes, helium-3 and helium-4, which undergo a phase separation when cooled below a critical temperature (see

Figure 25) [7]. The ^{3}He/^{4}He mixture is fed into the system after being compressed to approximately 2 bar and is pre-cooled by heat exchangers at the 50 K and 4 K stages of the integrated pulse tube cryocooler [7, 8]. The helium mixture is then condensed into the dilution unit through a flow impedance using the Joule-Thompson effect. Once all of helium has been condensed into the mixing chamber, the dilution refrigerator is started by pumping on the still at the outlet of the mixing chamber. This pumping allows the mixture to evaporatively cool, eventually bringing the temperature below the tricritical point at 870 mK where a separation occurs into a 'concentrated' ^{3}He phase, and a 'dilute' ^{3}He phase [7, 8].

When cooled below the tricritical point, the liquid ^{3}He in the concentrated phase will float on top of the more dense liquid ^{4}He. The electronic structure of both isotopes is identical, and thus the van der Waals potential is the same. However, because of their differing mass and thus zero point motion, the very small attractive van der Waals force between both atoms in the mixture is different. The lighter ^{3}He atom, having higher zero-point motion, occupies a larger volume and thus experiences a larger attractive force to ^{4}He atoms than it does to other ^{3}He atoms due to their ability to come closer together [7, 8]. Because of the stronger van der Walls forces, at the boundary between the two liquid phases ^{3}He atoms spontaneously 'dilute' themselves into the ^{4}He. In terms of the phase diagram, this represents a move from the concentrated phase to the dilute phase, which requires energy. The energy is extracted from the system as heat, causing the mixing chamber to cool – eventually reaching temperatures as low as 20 mK [7, 8].

In order to provide continuous cooling and avoid saturating the concentration of ^{3}He in the dilute phase, the outlet of the mixing chamber is pumped at the still. Because of the large difference in vapour pressure between the two isotopes, pumping results in almost pure ^{3}He being pumped away from the dilute phase. The resultant drop below the equilibrium concentration of ^{3}He in the dilute phase leads to an osmotic pressure that causes more ^{3}He to cross the phase boundary. The outlet of the still is pumped outside the fridge and re-introduced to the condensing side of the dilution unit, allowing continuous circulation of ^{3}He around the dilution refrigerator circuit and across the phase boundary in the mixing chamber [7, 8].

The sample is mounted on a probe and inserted into the dilution refrigerator cryostat, where it makes good thermal contact with the mixing chamber. Magnetotransport measurements were performed with independently applied perpendicular and parallel magnetic fields utilising the vector magnet integrated into the Leiden refrigerator. By collecting magnetotransport curves as a function of perpendicular magnetic field while applying a fixed parallel field it has been possible to probe the Zeeman interaction and thus determine the gyromagnetic ratio in the 2D hole band for the first time (Chapter 4).

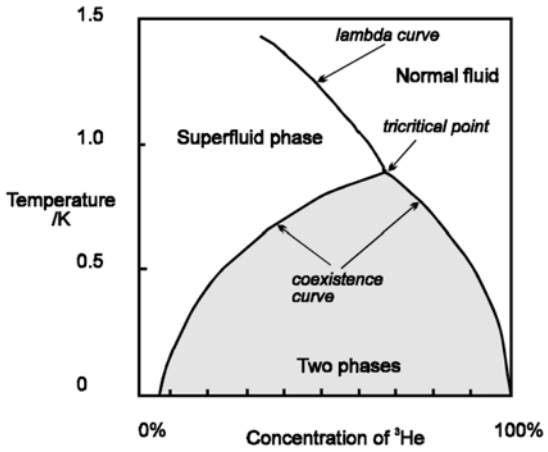

Figure 25: $^{3}He/\ ^{4}He$ phase diagram [7].

2.5 Hall measurements – measurement principles

This section will cover the principles of the magnetotransport measurements and the theoretical analysis used to examine the properties of the hole accumulation layer. The fitting methods utilised to extract the spin transport properties of the 2D hole band are also explained.

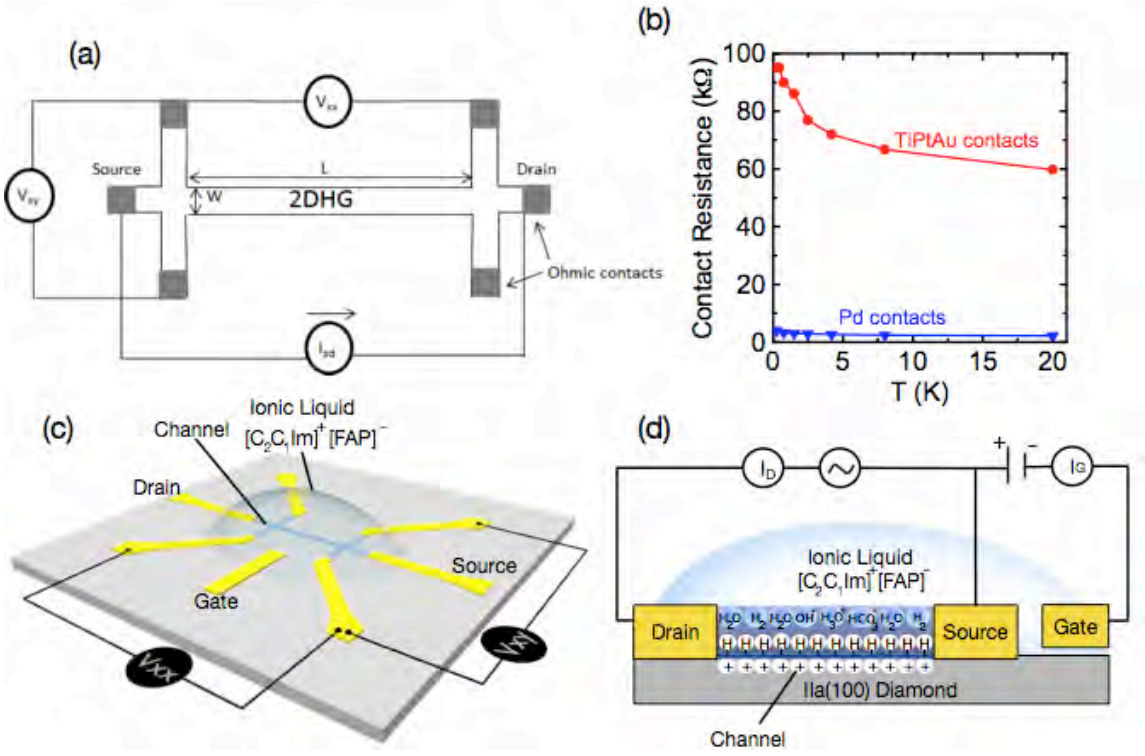

Figure 26: (a) Schematic illustration of a six contact Hall bar geometry and measurement set-up. (b) Contact resistance: Device A using Ti/Pt/Au contacts is plotted in red and Device B using Pd contacts is plotted in blue. (c) and (d) illustrate the arrangement used for ionic liquid gating of Hall bar devices.

2.5(a). Hall bar and Ionic Liquid Gated Device Measurements

Fabricated Hall bars were characterised as a function of temperature using standard low frequency AC lock-in techniques with addition of an applied magnetic field and with electrostatic gating in cases where an ionic liquid gate was utilised. Four-terminal measurements were performed using a low-noise AC lock-in set-up based around Stanford Research Systems lock-in amplifiers. In addition to measuring the longitudinal and transverse resistivity of the surface conducting diamond channel, using this 4-terminal measurement we were able to determine the contact resistance of fabricated devices. The contact resistance is given by $R_c = 0.5(R_{2T} - (L_{2T}/L_{4T}) \times R_{4T})$ [9]. Here R_{2T} is two-terminal resistance, R_{4T} is four-terminal resistance, L_{2T} is the length between source and drain leads (equal to 520 μm in the case of device A, and 540 μm in the case of device B) and L_{4T} is the length of the Hall bar channel (320 μm for device A and 200 μm for device B). The temperature dependence of the contact resistance for both devices A and B are illustrated in Figure 26b. We have seen a significant improvement in our contact resistant in device B using Pd contacts compared to device A with Ti/Pt/Au contacts, with the Pd contacts routinely providing superior device performance at cryogenic temperatures with low resistance at the metal-diamond interface [5]. For ionic liquid gating the FAP-based liquid, $[C_2C_1Im]^+[FAP]^-$, was used to tune the hole carrier density in the channel of the Hall bar. This was done by applying a voltage to the gate contact with the sample held at room temperature where the ions in the liquid are mobile. Magnetotransport measurements were performed on gated devices at low temperatures where the ions are no longer mobile (below about 236 K). In order to change the gate bias it was therefore necessary to warm the device to room temperature and re-cool for subsequent measurements. Thermal cycling of the device alone was not found to modify its electronic properties.

2.5(b). Transport Measurements - Perpendicular Magnetic Fields

Magnetoconductivity measurements were carried out by applying a constant voltage between source and drain leads and measuring a two-terminal current (between source and drain contacts) and four-terminal longitudinal voltage, V_{xx}, between contacts on the side of the Hall bar. This was carried out as a function of magnetic field applied perpendicular to the sample at a variety of temperatures. Therefore, the source-drain resistance and sheet resistivity, ρ_{xx}, were determined as a function of perpendicular

magnetic field. In parallel, the transverse voltage V_{xy} (which is the same as the Hall voltage V_H), measured across the device, was used to determine the Hall resistivity, ρ_{xy}. Using this approach, the hole carrier density and hole mobility were determined, and through $\rho_{xx}(B)$ weak localization and weak anti-localization effects were identified.

2.5(c). Transport Measurements – Concurrent Perpendicular and Parallel Magnetic Fields

As we have explained, magnetoresistance measurements using a perpendicular magnetic field were used to determine the transport properties of devices. In order to determine Zeeman splitting and well width variations of the diamond surface 2D hole band, an in-plane magnetic field should be applied in addition to the perpendicular field.

In this thesis magnetotransport measurements are performed on device B using both perpendicular and in-plane fields by sweeping B-perpendicular while a constant in-plane field was applied as shown in Figure 27. We observed changes in localization effects as the in-plane field strength was increased. More detail and results from this experiment are summarised in Chapter 4 and 5.

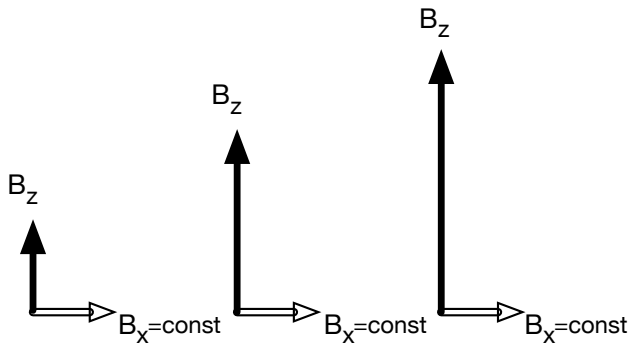

Figure 27: Magnetoresistance measurements in presence of in-plane field. Constant in-plane field (B_x) is applied and while sweeping the perpendicular field (B_z).

2.5(d). The Drude Model and Magnetoconductivity Tensor

To describe carrier motion in the presence of both an electric and a magnetic field the Lorentz equation can be used. The drift velocity $\vec{v}_d$ for holes is expressed in terms of $\vec{E}$ and $\vec{B}$ according to

$$\frac{m_h^*}{\tau}\vec{v}_d = +e\vec{E} + e\vec{v}_d \times \vec{B}. \quad (2.\ 1)$$

The drift velocity in the absence of $\vec{B}$ is,

$$\vec{v}_d = \frac{e\tau}{m_h^*}\vec{E} = \mu_h\vec{E}, \quad (2.\ 2)$$

where $\mu_h = \frac{e\tau}{m_h^*}$ is the hole mobility, τ is the momentum relaxation time and m_h^* is the effective hole mass. For a 2D system, the conductivity is $\sigma_0 = pe\mu_h = pe^2\tau/m_h^* = (e^2/\mathrm{h})k_F l$ where p is the number of holes per unit area, $k_F = \sqrt{2\pi p}$ is the Fermi wavevector and $l = (h\,\tau\sqrt{2\pi p})/(2\pi)$ is the mean free path which can also be expressed as $l = \sqrt{2D\tau}$; D is the carrier diffusion constant.

When a magnetic field is present σ takes the form of the conductivity tensor and therefore it is no longer a single number. From Ohm's law the relationship between the current density and electric field is $J = pe\mu_h\vec{E} = \sigma_0\overrightarrow{E}$, which can be expressed in Cartesian coordinates as

$$\begin{pmatrix} J_x \\ J_y \end{pmatrix} = \begin{pmatrix} \sigma_{xx}\ \sigma_{xy} \\ \sigma_{yx}\ \sigma_{yy} \end{pmatrix} = \begin{pmatrix} E_x \\ E_y \end{pmatrix}. \quad (2.\ 3)$$

From the ratio of the current density to the electric field, in the presence of an applied magnetic field perpendicular to the sample i.e. the Drude model, we can express the 2D conductivity and resistivity tensors respectively as

$$\vec{\sigma} = \frac{\sigma_0}{1+(\omega_c\tau)^2}\begin{pmatrix} 1 & \omega_c\tau \\ -\omega_c\tau & 1 \end{pmatrix} \quad (2.\ 4)$$

and

$$\vec{\rho} = \frac{1}{\sigma_0}\begin{pmatrix} 1 & -\omega_c\tau \\ \omega_c\tau & 1 \end{pmatrix}, \quad (2.\ 5)$$

where $\omega_c = eB/m^* = \mu B/\tau$ is the classical cyclotron frequency.

The conductivity and resistivity tensor equations (2. 4) and (2. 5) show that the external magnetic field affects the off-diagonal elements and is therefore responsible for the Hall Effect. The off-diagonal elements are independent of τ. As a result, the Hall coefficient provides information about the material itself such as charge carrier density rather than properties that are caused by scattering. In contrast, ρ_{xx} is sensitive to the scattering time as it is measured in appropriate length and width area.

From the longitudinal and transverse elements of the resistivity tensor, we may deduce the corresponding elements of the conductivity tensor:

$$\sigma_{xx}(B) = \frac{\rho_{xx}}{\rho_{xx}^2+\rho_{xy}^2} \tag{2. 6}$$

and

$$\sigma_{xy}(B) = \frac{\rho_{xy}}{\rho_{xy}^2+\rho_{xx}^2}. \tag{2. 7}$$

However, in systems for which $\rho_{xx} \gg \rho_{xy}$ holds, the equation (2.6) can be reduced to $\sigma_{xx} = 1/\rho_{xx}$.

2.5(e). The Classical Hall Effect

When a constant current flows along the channel of the Hall bar device (in the x-direction) and a constant magnetic field B_z is applied perpendicular to the plane of the two dimensional carrier sheet (xy plane), the Hall effect manifests itself by an induced Hall voltage in y-direction. This arises because the applied magnetic field induces an acceleration of electrons and holes perpendicular to the x-direction. In other words, the charge carriers experience a force (the Lorentz force), $F = qv_x \times B_z$, along the y-direction causing the charge carriers to accumulate on one side and deplete on the other of the Hall bar. In equilibrium, the accumulated charge difference creates an electric field E across the Hall bar such that the Coulomb force in the y-direction is equal and opposite to the Lorentz force (Figure 28). The density p and mobility μ of carriers can then be determined from the equations:

$$p = \frac{IB}{eV_H} = \frac{1}{e\rho_{xy}} \tag{2. 8}$$

and

$$\mu = \frac{1}{ep\rho_{xx}}. \tag{2. 9}$$

The Hall (transverse) resistivity, $\rho_{xy} = V_{xy}/I_{sd}$, while the longitudinal resistivity, $\rho_{xx} = (W/L)\, V_{xx}/I_{sd}$, where W and L are the width and length of the channel in the Hall bar device. For the devices measured in this thesis, $W/L = 320\ \mu m/40\ \mu m$ (device A) and $W/L = 200\ \mu m/40\ \mu m$ (device B).

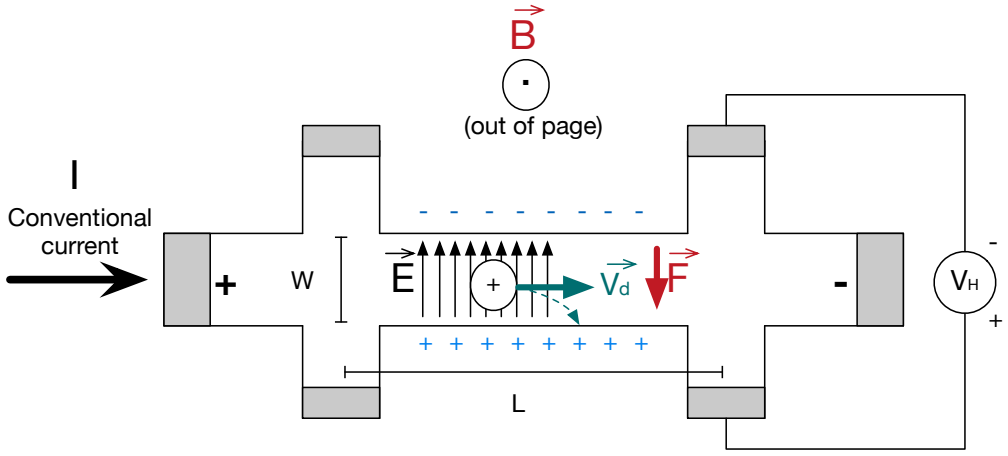

Figure 28: (a) Hall Effect in a p-type Hall bar geometry (Note: Hall Voltage, $V_H = V_{xy}$).

Under steady-state conditions, the Hall coefficient, R_H, describes carrier density and the sign of their charge. It can be expressed as:

$$R_H = \frac{E_y}{J_x B_x} = \frac{\omega_c \tau}{\sigma_0 B_0} = \frac{\rho_{xy}}{B_z} = \frac{1}{pe}, \tag{2.10}$$

where τ is the relaxation time, σ_0 is the conductivity and ω_c is the classical cyclotron frequency.

2.6 Magnetotransport Measurements and Spin Interference at Low Temperature

At low temperature, when electron-phonon scattering is suppressed, transport phenomena due to the interference of the wavefunction of carriers (in our case holes) can be observed. The measurement of longitudinal and transverse resistivities as a function of temperature and of magnetic field are at the centre of this thesis as they reveal interesting information about charge and spin transport in 2D systems. In the previous section, we described charge transport in the Drude picture, with the Hall effect applied to extract the carrier density and mobility. When performed at cryogenic temperatures, magnetotransport may involve quantum corrections to the Drude model which arise from hole-hole interactions (HHI) and phase-coherent backscattering phenomena in the form of weak localization (WL) and weak anti-localization (WAL). As we have noted previously, this can be particularly prevalent in electronic systems that support a quasi-2D band-structure where the effects of a spin-orbit interaction on the WAL backscattering may also be evident.

The modelling of phase coherent transport in 2D systems has been discussed in detail by McPhail *et al.* [10] and Bergmann [11] who consider a number of methods for modelling the quantum corrections to the Drude model in 2D systems where the mean free path is smaller than the cyclotron radius [10]. In this work we focus predominantly on the quantum transport model developed by Hikami which can be used to study spin relaxation in the diffusive transport regime [12]. This work enables magnetoconductance curves to be modelled at low magnetic fields for 2D electronic bands in the presence of a spin orbit interaction. In the following we focus firstly on understanding the quantum corrections that arise when a perpendicular magnetic field is applied to the 2D hole band in diamond by using the Hikami equation to model the magnetotransport behaviour in the presence of spin-orbit coupling due to both the Rashba and Dresselhaus mechanisms. Secondly, we will discuss in some detail the additional mechanisms that come into play when an in-plane field is applied, following the approach of Minkov *et al.* [11] by adding further corrections to the singlet and triplet terms in the Hikami equation.

2.6(a). Interference Effects – Weak Localization

When an electron, or in our case a hole, moves through a material, whether it is a 2D or 3D system, it undergoes transport as a quantum mechanical wave function. If that material is disordered, the charge transport is diffusive due to the presence of scattering centres

[15]. For transport measurements performed at high temperature, no correction to the Drude conductivity is required to take account of the wave character of the propagating charged particles. Quantum mechanical interference is strongly suppressed because the time associated with the temperature averaging is smaller than the phase coherence time ($\tau_T < \tau_\phi$) [12]. Therefore, at high temperature, the phase coherence time is strongly reduced compared to transport scattering time since there are more phonons. However, inelastic electron-phonon scattering is suppressed at sufficiently low temperatures such that scattering is elastic only which preserves the phase of the wave function of the carrier in the scattering process [13].

We consider the case that the size of that loop is smaller than the phase coherence length l_ϕ, i.e. elastic mean free path l_e is shorter than l_ϕ at low temperatures [13]. Therefore, multiple scattering events occur and there is a small but finite chance that the carrier scatters backwards around a closed loop to its origin (Figure 29).

The total probability that a charge carrier will diffuse from point $\vec{r}$ to point $\vec{r}'$ (around a closed loop) is determined by considering all possible paths the carrier can traverse and takes the form of the square the wave function: [12, 13]

$$P(\vec{r},\vec{r}',t) = \left|\sum_j A_j\right|^2 = \left|\sum_j C_j e^{i\varphi_j}\right|^2, \qquad (2.\ 11)$$

where A is a complex amplitude that defines each path j and φ_j is the phase shift that a charge carrier undergoes when travelling between consecutive scattering events.

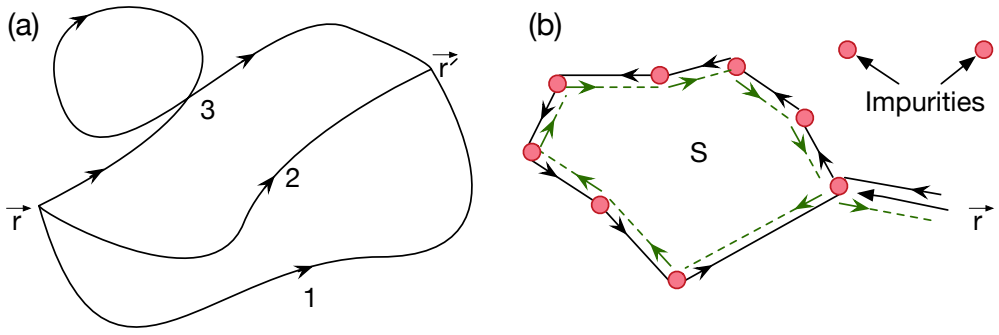

Figure 29: (a) Possible diffusion trajectories of charge carriers (in our case holes) at low temperatures from point $\vec{r}$ to point $\vec{r}'$ within a disordered system. The phase shift of holes travelling in trajectories 1 and 2 are uncorrelated but holes travelling in trajectory 3 are scattered and a self-intersecting loop is created. (b) Closed loop; charge carrier propagation in both directions (clockwise and counter-clockwise) in a disordered system can lead to constructive and destructive interfere of the carrier wave function.

According to the Aharonov-Bohm effect [14], first explained with a ring-shaped geometry in 1959, if we consider two partial waves that are propagating in opposite directions along the same path to return to their origin, they arrive there with the same accumulated phase and will therefore interfere constructively [13, 14]. In other words, in the absence of spin-orbit coupling, the phase difference is zero as both the clockwise ($\Psi^{\circlearrowright}$) and anticlockwise ($\Psi^{\circlearrowleft}$) wave functions possess the same amplitude along the looped path but propagate in opposite directions. As a result, the hole waves constructively interfere. This implies that the probability of returning to the original point is $P(\vec{r},\vec{r}',t) = |\Psi^{\circlearrowright} + \Psi^{\circlearrowleft}|^2 = |A_1 + A_2|^2 = 4|A|^2$. Thus, the probability for backscattering is twice as high as the classical diffusion case for which there is no quantum interference [10, 12, 13]. It is worth mentioning that the size of loops in a disordered conductor are different as a result of statistical distribution of scattering centres (Figure 30). However, regardless of the size when B = 0 T, constructive interference occurs in all loops for which the loop length is shorter than the phase coherence length. [13]

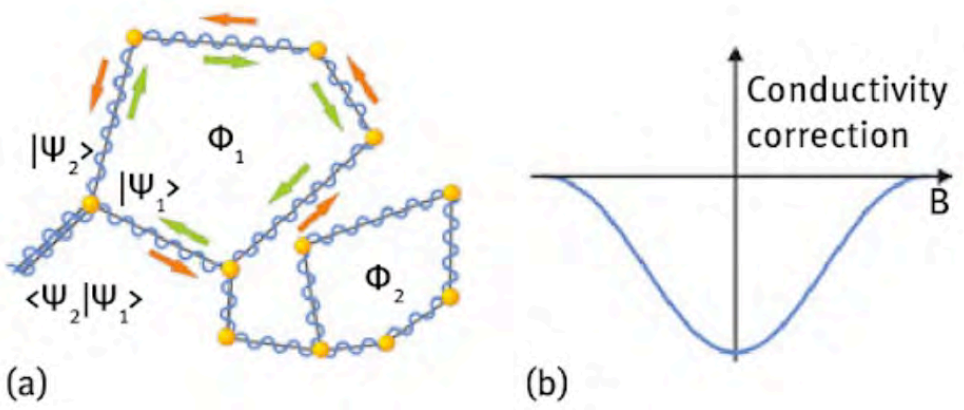

Figure 30: Weak localization: (a) Electron interference during propagation of charge carriers around closed loops. (b) The resulting negative conductivity correction at B = 0 T [13].

The probability of this event is rare in 3D systems but in 2D systems which possess one less degree of freedom, the contribution of these cases of backscattering is higher. As a result in 2D systems an enhancement in resistance, and concurrent reduction in conductance, at B = 0 T is often observed as illustrated in Figure 30; this is a signature of weak localization (WL). WL may be observed in the magnetoconductance as long as the phase coherence of the carriers is not lost. In contrast, when the phase coherence is lost, carrier transport is in a non-phase coherent regime and even though both clockwise and anti-clockwise wave functions interfere, one of the partial waves may become out of

phase. In this case the probability of returning to the origin is $|A_1|^2 + |A_2|^2$ and therefore it is a factor of two smaller than in the phase coherent regime.

As we shall show, in surface conducting diamond WL can usually be observed at temperatures up to 20 K, as long as the hole carrier density is not too low.

2.6(b). Dependence on an applied magnetic field

The application of a perpendicular magnetic field breaks the time-reversal symmetry between counter-propagating charge particles by inducing an additional phase to the carrier wave function as it moves around the loop (Figure 31). The sign of the phase depends on the direction of motion of the particle with respect to the field direction. As a result, a phase shift ($\Delta\phi$) is acquired between the two wave functions in a closed loop [12, 13]. The phase shift is given by

$$\Delta\phi = \frac{2e}{\hbar}\int\left(\nabla \times \vec{A}\right)d\vec{S} = \frac{2e}{\hbar}BS = \frac{2S}{l_m^2} = 2\pi\frac{\phi}{\phi_0}, \qquad (2.\ 12)$$

where $\vec{A}$ is the magnetic potential, $\phi_0 = h/2e$ is the elementary flux quantum, $l_m = \sqrt{\hbar/eB}$ is the magnetic length and magnetic field B is proportional to the flux ϕ enclosing the loop of area of S. Therefore, when a magnetic field perpendicular to the quantum well is applied the interference between the two wave functions is no longer as constructive as before and the contribution of this loop to the increased resistivity is reduced. As previously discussed, many such loops traversed by the charge carriers in a device contribute to the resistance enhancement at B = 0 T. As the applied magnetic field increases, a gradual reduction in the resistance is observed (Figure 31) as the constructive interference of wave functions for each loop is suppressed. The magnetic field strength at which WL is no longer present is called the transport field: [12]

$$B_{tr} = \frac{\hbar}{2eD\tau}, \qquad (2.\ 13)$$

where D is the diffusion coefficient and $\tau = m^*\sigma_D/pe^2$ is the transport or elastic scattering time. τ can be calculated using the measured Drude conductivity σ_D either at

high temperature or in a high magnetic field, where the correction to the conductivity arising from WL is fully suppressed. In this thesis, we used the first of these approaches to evaluate the Drude conductivity and hence determine τ. For systems with low carrier mobility, such as surface conducting hydrogen terminated diamond, B_{tr} is larger than the magnetic field typically achievable in the laboratory [15-17].

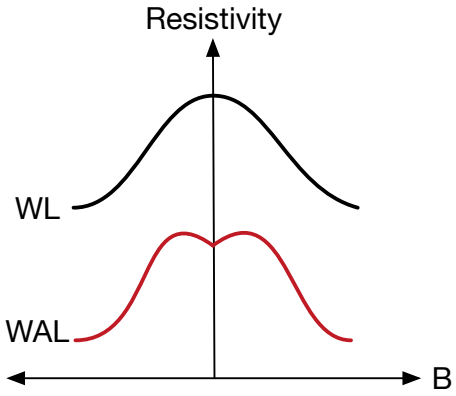

Figure 31: Magnetic field effect on weak localization (WL) and weak anti-localization (WAL).

2.6(c). Weak Anti-localization (WAL)

Weak anti-localization (WAL) is a characteristic effect that, like WL, is evident in 2D systems but observed in materials which additionally possess a high spin-orbit interaction. As we shall show, it can therefore be used to determine the strength of the spin-orbit coupling in semiconductors possessing a 2D band structure. WAL is observed as a cusp in the magnetoresistance at B = 0 T (Figure 31) and therefore has significant utility in probing spin-orbit effects in materials which possess a low carrier mobility, for which the alternative technique of determining spin orbit coupling from the observation of Shubnikov-de-Haas oscillations would require unachievably high magnetic fields.

In our earlier discussion of WL we assumed that the spin orientation of charge carriers is preserved when they propagate. A consequence of the spin-orbit interaction is that the spin orientation changes while the partial waves propagate around closed loops. This will destruct the constructive interference that gives rise to WL by breaking the time reversal symmetry, a phenomenon known as weak anti-localization (WAL), resulting in an increase in conductivity at B = 0 T which is observable as long as the spin-orbit interaction is sufficiently strong. As we shall show, for surface conducting diamond a signature of

WAL emerges in the magnetoconductance curves as the measurement temperature of our devices decreases below about 4 K. As the temperature decreases, the phase coherence time and phase coherence length increase. This means the phase-coherent loops around which partial waves propagate increase in size. If the size of the loop exceeds the spin coherence length spin-orbit effects then come into play. In this case, when a charge carrier moves around the loop, the high spin-orbit coupling causes a rotation of the carrier spin. The total carrier wave function is a product of spatial and spin components of the form $\Psi^{\circlearrowleft} = u(\vec{r}).e^{i(\omega t+\phi+\Delta\phi)}$ and $\Psi^{\circlearrowleft} = u(\vec{r}').e^{i(\omega t+\phi-\Delta\phi)}$ (where ϕ is the spatial part and $\Delta\phi$ is the phase change due to the spin precession). In the presence of a spin-orbit interaction the spatial component of the wave function may still interfere constructively but the spin component does not. This gives rise to an increase in conductivity at B = 0 T, relative to the magnetoconductivity arising from WL. On account of the peculiarities of the spin wave function, in the extreme case there may be negative interference between counterpropagating wave functions which leads to an enhancement in the conductivity even beyond the Drude conductivity, as illustrated in Figure 32. As noted above, WAL is known to be the characteristic of 2D systems which possess a high spin-orbit coupling. Consequently, in materials with a strong spin orbit coupling, as the temperature is reduced the resistance will decrease logarithmically and magnetoresistance changes sign [10].

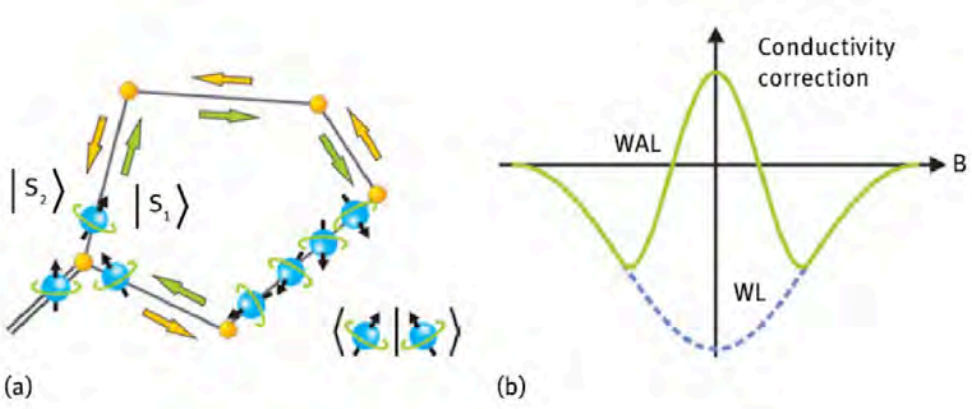

Figure 32: Weak anti-localization: (a) Spin precession as a result of spin-orbit coupling; (b) The resulting enhancement of the conductivity at B = 0 T relative to the WL curve [13].

In this thesis the spin-orbit interaction in the 2D hole band at the surface of diamond was determined from magnetoconductance measurements using the approach of Bergmann *et al.* [18]. For the case of WL, as discussed above, interference of the carrier wave functions around phase coherent loops is always constructive at B = 0 T regardless of the shape and the size of the loops. However, according to Bergmann *et al.* [18], in the presence of spin

orbit coupling the geometry of the closed loops also need to be considered as the spin orientation of carriers changes as they move around the loop and each closed loop causes a different spin rotation. In the approach of Bergman *et al*., where there is a strong spin orbit coupling, the final state of the spin is distributed statistically and averaging over all the interference amplitudes caused by both carrier phase and spin orientation leads to a destructive interference effect and enhancement of conductance at $B = 0$ T as illustrated in Figure 32 [10, 18].

There are two well-known mechanisms that may lead to spin precession in 2D systems, both depending on a loss of inversion symmetry, the Rashba and Dresselhaus effects. In the Rashba effect the loss is due to a strong electric field perpendicular to the 2D plane that gives rise to a higher asymmetric quantum confinement potential. When the crystal structure itself has inversion symmetry, spin precession arises from the Dresselhaus effect. In this thesis, we fit data to both models and find similar strengths of the spin orbit coupling are derived. However, as we point out below, due to the strong band bending at the diamond surface and tunability of the spin orbit coupling we expect the spin precession of the hole band in this case to arise from the Rashba effect.

2.7 Hikami Theory (Dresselhaus and Rashba mechanisms)

As previously mentioned, one way to determine the strength of the spin-orbit coupling in a 2D system is by analysing the beating patterns observed in Shubnikov-de Hass oscillations. However, as our surface conducting diamond devices have low hole mobility it is difficult to obtain such information. As an alternative, the spin parameters can be extracted from analysis of the WAL as this mechanism relies on the diffusive transport of the holes. In order to extract spin orbit coupling parameters from magnetoconductance data we need to apply the WAL theories and fit the magnetoconductance as a function of applied magnetic field to the theoretical models.

There have been several seminal papers discussing localization effects in 2D systems. Bergmann *et al.* provided an excellent review about magnetoconductance in 2D electronic systems [10]. Al'tshuler *et al.* and Hikami *et al.* discussed in detail the effect of localization on the magnetoconductance [19, 20]. Pikus *et al.* developed the theory behind WAL in the 1990s [16, 17] and McPhail *et al*., discuss the many approaches that have been developed to extract the corresponding quantum corrections to the Drude

conductivity [21]. In this thesis, we have used the model developed by used Hikami *et al.* that is limited to the diffusive regime ($B \ll B_{tr}$) to describe the effects of spin relaxation on magnetoconductance curves in low magnetic fields. Also, Hikami theory is only valid for low quality samples or high-quality samples, with low mobility as in our case, for which the momentum relaxation length is smaller than the phase coherence length [21]. In contrast, for samples with high mobility the measurement needs to take place beyond the diffusive regime in order to study the WL and WAL effects [21].

Following the approach of Hikami *et al.,* the correction to the Drude conductivity due to WL effects takes the form

$$\Delta\sigma_{WL} = \frac{e^2}{2\pi^2\hbar}\left[\Psi\left(\frac{1}{2}+\frac{B_1}{B}\right) - \Psi\left(\frac{1}{2}+\frac{B_2}{B}\right) + \frac{1}{2}\Psi\left(\frac{1}{2}+\frac{B_3}{B}\right) - \frac{1}{2}\Psi\left(\frac{1}{2}+\frac{B_4}{B}\right)\right], \quad (2.14)$$

where Ψ is the digamma function, $B_1 = B_{tr} + B_{so} + B_s$, $B_2 = 4/3\,B_{so} + 2/3\,B_s + B_\phi$, $B_3 = 2B_s + B_\phi$ and $B_4 = 4/3\,B_{so} + 2/3\,B_s + B_\phi$. The indices in the characteristic fields: tr, ϕ, so and s relate to the common scattering mechanisms: momentum scattering, phase breaking scattering, spin orbit scattering and magnetic scattering. These characteristic fields, B_n, are proportional to the corresponding scattering rates $1/\tau_n$ through the equation $B_n = \hbar/4eD\tau_n$ [10]. In our hydrogen terminated devices we expect minimal magnetic scattering so assume B_s = 0 in what follows.

Establishing the most valid theory for modelling WAL is more complicated in part due to the fact that, as noted above, a spin orbit interaction can arise due to a lack of inversion symmetry in the crystal structure of the quantum well (Dresselhaus mechanism) or due to the asymmetry quantum well that may be caused by an external electric field perpendicular to the plane of the 2D system (Rashba mechanism). Theoretically, the difference between these two spin orbit interaction mechanisms can be explored via the Hamiltonian

$$H(\boldsymbol{k}) = \hbar\boldsymbol{\sigma}.\boldsymbol{\Omega}(\boldsymbol{k}), \quad (2.15)$$

where k is the wave vector of the charge carrier, σ is the vector of Pauli matrices and $\Omega(k)$ is a vector operator that is an odd function of k. The spin splitting that leads to the spin orbit interaction is given by $2\hbar\Omega(k)$ [15], such that $\Omega(k)$ is an effective magnetic

field around which the spin of the carrier processes. In both mechanisms the spin splitting is isotropic in k-space [15]. This Hamiltonian can have two different forms due to the functional form of $\Omega(k)$ which can be either linear or cubic in k in 2D heterostructure systems.

In this thesis, we considered both the Dresselhaus and Rashba mechanisms but, as noted above, we expect that the WAL observed arises predominantly from the Rashba effect. The Dresselhaus mechanism depends on the inversion symmetry of the crystal lattice. The strength of the spin orbit splitting depends on the intrinsic atomic spin orbit interaction which in diamond is the lowest of all elements except for boron. Therefore, in our case any role that the Dresselhaus mechanism plays must be due to the hydrogen terminated surface of diamond. The Rashba mechanism is due to the asymmetry that is imposed by the electric field perpendicular to the 2D plane. In surface conducting diamond there exists a strong band bending that confines the holes to the near surface. The magnitude of the electric field F right at the diamond surface is tied to the hole carrier density via Gauss's law (Figure 33) and may be as high as 1 Vnm^{-1}.

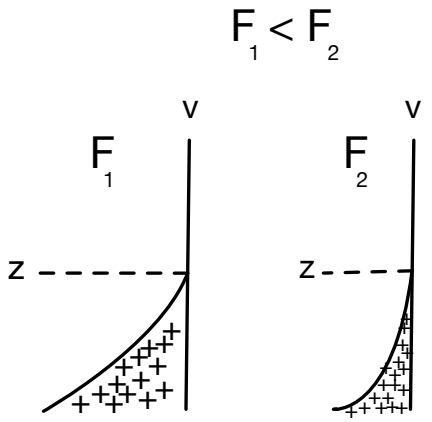

Figure 33: Asymmetry quantum well. $F = \Delta v/\Delta s = 1/\varepsilon\varepsilon_0$ is the electric field perpendicular to the 2D plane and it is proportional to the areal charge density p and equal to the slope of the band bending right at the surface.

Schäpers [15] and Glazov and Golub [17] give an excellent review of the differences between the Dresselhaus and Rashba mechanisms in 2D semiconductor systems, including a description of the corresponding forms of the function $\Omega(k)$. $\Omega(k)$ can be expanded as a Taylor series and adopts only odd powers of k: $\Omega(k) = \Omega^{1}(k) + \Omega^{3}(k)$ [15]. In the Dresselhaus case, Ω_D contains both linear and cubic terms in k, as first

described for Zinc-blende crystals [22]. However, when considering quantum wells with (001) orientation the cubic terms in k are diminished and Ω_D reduces to a linear function of k [23, 24]. The Rashba effect has historically only been described with Ω_R linear in k, however in recent years contributions that are cubic in k have been included in order to describe spin-orbit effects in p-type 2D quantum systems [25-27].

For both the Rashba and Dresselhaus cases, the effective magnetic field vector $\Omega(k)$ lies in the 2D plane of the electronic system, defined here as the x-y plane [15]. However, the direction of $\Omega(k)$ within the x-y plane are different for the two mechanisms. In their linear-k form the field directions are defined by $\Omega_D^1 = \Omega_D(\cos\theta - \sin\theta)$ and $\Omega_R^1 = \Omega_R(\sin\theta - \cos\theta)$ respectively [15], where θ is the angle between $\boldsymbol{k}$ and the x-axis; the resulting vector directions are illustrated in Figure 34. In the Dresselhaus case, the direction of Ω_D can be both parallel and perpendicular to the direction of $\boldsymbol{k}$; in contrast, in the Rashba mechanism, Ω_R is always perpendicular to $\boldsymbol{k}$.

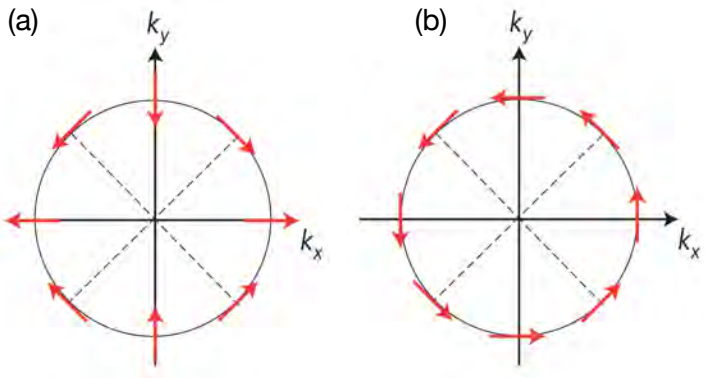

Figure 34: Effective magnetic field direction for linear (a) Dresselhaus and (b) Rashba, [24] with respect to the direction of the carrier wavevector.

In p-type systems, such as the 2D hole band at the surface of diamond considered here, the introduction of terms that are cubic in k modifies the direction of the effective magnetic field vector to give $\Omega_R^3 = \Omega_R(\pm\sin 3\theta \mp \cos 3\theta)$; note that $\pm$ corresponds to the direction of spin. In this case the vector rotates 3 times in the plane as k rotates once (Figure 35) [26]. Note Whereas, in k-linear it only rotates once and always remains perpendicular to the k-vector and that is why k-cube influence all the phenomena that is induced by spin-orbit interactions [25-27].

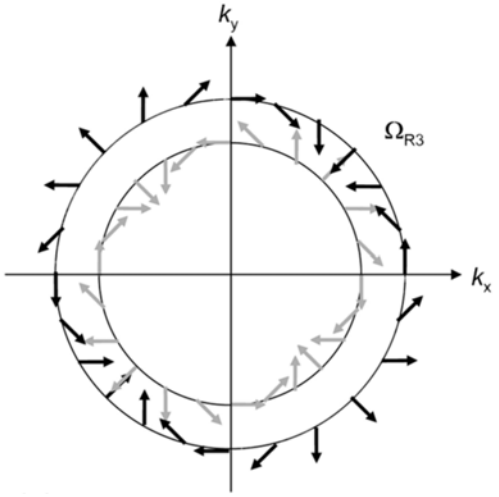

Figure 35: Schematic of the effective magnetic field vector for the cubic Rashba effect. It demonstrates that there are 3θ rotations in k-space around the Fermi circle in both spin configurations [26].

The theoretical model describing the effect of the Dresselhaus mechanism on the conductance (2.16) was initially developed by Dresselhaus *et al.* [10, 28] and cubic-k Rashba theory (2.17) by Knap *et al.* [29]. Using the Hikami formula, in the absence of that magnetic scattering ($B_s = 0$ T) and with $G_0 = e^2/2\pi^2\hbar$, these can be expressed as

$$\Delta\sigma = -G_0\left[\Psi\left(\frac{1}{2}+\frac{B_{tr}+B_{so}}{B}\right)-\frac{3}{2}\Psi\left(\frac{1}{2}+\frac{4/3B_{so}+B_\phi}{B}\right)+\frac{1}{2}\Psi\left(\frac{1}{2}+\frac{B_\phi}{B}\right)-ln\left(\frac{1}{2}+\frac{B_{tr}+B_{so}}{B}\right)+\frac{3}{2}ln\left(\frac{1}{2}+\frac{4/3B_{so}+B_\phi}{B}\right)-\frac{1}{2}ln\left(\frac{1}{2}+\frac{B_\phi}{B}\right)\right], \quad (2.16)$$

for the case of the Dresselhaus effect and

$$\Delta\sigma = G_0\left[\Psi\left(\frac{1}{2}+\frac{B_\phi+B_{so}}{B}\right)+\frac{1}{2}\Psi\left(\frac{1}{2}+\frac{B_\phi+2B_{so}}{B}\right)-\frac{1}{2}\Psi\left(\frac{1}{2}+\frac{B_\phi}{B}\right)-ln\left(\frac{1}{2}+\frac{B_\phi+B_{so}}{B}\right)-\frac{1}{2}ln\left(\frac{1}{2}+\frac{B_\phi+2B_{so}}{B}\right)+\frac{1}{2}ln\left(\frac{1}{2}+\frac{B_\phi}{B}\right)\right], \quad (2.17)$$

for the Rashba effect.

In both cases, the third and last terms correspond to singlet states and depend only on the phase coherence field $B_\phi = \hbar/4eD\tau_\phi$, where τ_ϕ is the inelastic phase relaxation time, that is the lifetime of a charge carrier in a momentum eigenstate [10, 11]. The other terms contribute to triplet states as they depend not only on the parameter B_ϕ and the dephasing

rate, but also on the spin-orbit field $B_{so} = \hbar/4eD\tau_{so}$ where τ_{so} is the spin relaxation time, that is the lifetime of the charge carrier in an energy eigenstate [10, 11].

We shall discuss these two theories more in chapter 3 and determine which mechanism is dominant in the 2D hole system on diamond devices.

2.8 Effect of an applied in-plane magnetic field on the WAL: probing the Zeeman interaction and microroughness of the quantum well

As we have described above, magnetoconductance measurements in a magnetic field applied perpendicular to the 2D plane provides information about phase relaxation rates and the strength of spin orbit coupling as mainly orbital motion of charge carriers affects the anomalous magnetoresistance. The addition of an in-plane magnetic field, applied parallel to the plane of a 2D carriers, provides access to additional information about the spin properties of the 2D carrier band. In this section, we shall discuss the role of an applied in-plane magnetic field on the 2D heterostructures. In this case the Zeeman splitting, which describes the response of carrier spins to an applied magnetic field becomes important. Mal'shukov *et al.* were the first to point out that the Zeeman splitting due to addition of an in-plane field can overcome spin orbit coupling and break the time reversal symmetry [30, 31]. This leads to a mixing of the singlet and triplet components of the Hikami equation. When both perpendicular and in-plane fields are applied the relative strengths of spin orbit coupling and Zeeman effect depends upon the resulting direction of the magnetic field vector. The addition of an in-plane magnetic field gives rise to a suppression of the WAL. Gougam *et al.* [32], Minkov *et al.* [11], Meijer *et al.* [33] and Cabanas *et al.* [34] have all observed this weak anti-localization suppression experimentally and compared it with theoretical models. Glazov and Golub *et al.* have also discussed two mechanisms by which an applied in-plane magnetic field can effect a 2D carrier band; we expand on these below [15].

2.8(a). Zeeman Splitting

The first mechanism that we will discuss is the Zeeman energy splitting, $E_z = g\mu_B B_{\|}$ where g is the gyromagnetic factor of the charge carriers (in our case holes), μ_B is the Bohr magnetic moment and $B_{\|}$ the in-plane magnetic field [34]. This splitting affects both weak localization and weak anti-localization and it reduces the depth of the weak anti-

localization resistivity minimum close to $B = 0\ T$. The Hamiltonian representing Zeeman splitting is given by

$$H_z = \frac{\hbar}{2}\boldsymbol{\sigma}.\Delta, \tag{2. 18}$$

where $\Delta = \widehat{\boldsymbol{g}}\mu_B \boldsymbol{B}_{\parallel}/\hbar$ [15].

The complete Hamiltonian in the presence of both spin-orbit coupling and Zeeman splitting then becomes

$$H = H_0 + \hbar\boldsymbol{\sigma}.\boldsymbol{\Omega}(\boldsymbol{k}) + \frac{1}{2}\boldsymbol{\sigma}.\widehat{\boldsymbol{g}}\mu_B \boldsymbol{B}_{\parallel}, \tag{2. 19}$$

where the first term, H_0, is the Hamiltonian in the absence of spin effects. The second term $\hbar\boldsymbol{\sigma}.\boldsymbol{\Omega}(\boldsymbol{k})$ represents the spin orbit coupling of carrier spin $\boldsymbol{s} = (\hbar/2)\,\boldsymbol{\sigma}$ and the internal magnetic field $\boldsymbol{\Omega}(\boldsymbol{k})$. The last term $\frac{1}{2}\boldsymbol{\sigma}.\widehat{\boldsymbol{g}}\mu_B \boldsymbol{B}_{\parallel}$ represents the Zeeman interaction of carriers with the external in-plane magnetic field [30, 31].

2.8(b). Interface Microroughness

The second mechanism arises from interfacial microroughness which, in the presence of an in-plane magnetic field, may also decrease the depth of the WAL minimum. This mechanism is purely orbital, and it effects both singlet and triplet states in the Hikami equation in the same manner [11]. This parameter can provide information about imperfections of the quantum well interfaces as a result of spatial shifts of the carriers as they move along the quantum well. This random shift in a perpendicular direction which gives rise to the longitudinal magnetoresistivity [11]. Quantitatively, as a result of an applied in-plane field the characteristic phase relaxation field acquires an additional dephasing term, $B_\phi(B_\parallel) = B_\phi(0) + \Delta_r(B_\parallel)$. In the presence of weak localization effect there is contribution to the conductance curve as a result of constructive interference of electrons in the closed loops. As it is explained earlier in the section 2.6(b), this effect is suppressed as perpendicular field is increased. Later in Chapter 4 and 5 we show the effects of an in-plane field due to the interface roughness.

2.8(c). The Rashba effect in the presence of Zeeman splitting and microroughness

The Zeeman splitting and microroughness of the hole confinement potential for surface conducting diamond are explored in detail in Chapters 4 and 5. A quantitative analysis of the WL and WAL signatures in magnetoconductance curves obtained in the presence of an in-plane magnetic field was undertaken to probe the gyromagnetic ratio in the 2D hole band for the first time and to explore the extent of microroughness in the hole confinement potential, which may be expressed in terms of fluctuations in the quantum well width. Furthermore, by gating the surface with an ionic liquid gate, changes to the gyromagnetic ratio and well width fluctuations are probed as a function of hole carrier density. As the applied in-plane field is increased, Zeeman splitting destroys WAL and reduces the spin orbit coupling term. This is due to mixing of the singlets and triplets by an applied in-plane field that leads to reduction in the conductivity until it overcomes the spin orbit coupling at very high fields [15]. However, at high in-plane magnetic fields equation (2.14) is not valid as the Zeeman interaction mixes the singlet and triplet terms and breaks the time reversal symmetry [31]. However, if the applied in-plane field is not too strong and the condition $g\mu_B B_{\|} < \hbar/\tau_{so}$ is met, only the singlet terms are affected by the Zeeman interaction.

Following the approach by Minkov *et al.* [11] the Hikami equation (2.14) can be adapted to include correction terms in the form of additional phase breaking fields due to the Zeeman interaction and well width fluctuations; this takes the form

$$\Delta\sigma = \frac{e^2}{2\pi^2\hbar}\left[\Psi\left(\frac{1}{2}+\frac{B_\phi+B_{so}+\Delta_r}{B_\perp}\right)+\frac{1}{2}\Psi\left(\frac{1}{2}+\frac{B_\phi+2B_{so}+\Delta_r}{B_\perp}\right)-\frac{1}{2}\Psi\left(\frac{1}{2}+\frac{B_\phi+\Delta_S+\Delta_r}{B_\perp}\right)-\ln\left(\frac{B_\phi+B_{so}+\Delta_r}{B_\perp}\right)-\frac{1}{2}\ln\left(\frac{B_\phi+2B_{so}+\Delta_r}{B_\perp}\right)+\frac{1}{2}\ln\left(\frac{B_\phi+\Delta_S+\Delta_r}{B_\perp}\right)\right]. \quad (2.20)$$

The term $\Delta_r = \frac{\sqrt{\pi}}{2}\frac{e}{\hbar}\frac{d^2L}{I}B_{\|}^2$ is the correction due to well width fluctuations, of rms magnitude *d* over a spatial correlation length of *L*; this correction is added to the singlet and the triplet terms in the Hikami formula. The correction $\Delta_s = \frac{\tau_{so}}{4e\hbar D}(g\mu_B B_{\|})^2$ is the Zeeman splitting parameter that is applied only to the singlet terms in the Hikami formula. In principle, and as we shall explore in Chapter 4, both mechanisms are present and the relative contributions can be obtained by fitting experimental magnetoconductance

curves to (2.20) with Δ_r and Δ_s as fitting parameters while maintaining the requirement that both terms should be proportional to $(B_{\parallel})^2$.

2.9 Hole-Hole Interaction (HHI)

The hole-hole interaction is another scattering process that needs to be considered in 2D hole gas on hydrogen terminated diamond and, in fact, extracted from the Drude conductivity in order to quantitatively explore the phase coherent WL and WAL effects. The HHI correction is due to the self-interaction of the holes and results from the interaction between two different holes while they diffuse in a closed scattering loop. For instance, if two holes with the same momentum and energy diffuse from point $\vec{r}$ to point $\vec{r}'$, their transport takes longer when there is attraction between them. Note that the interaction between the two holes is a quantum effect and not the classical Coulomb repulsion [12]. The correlated electrons that transport together alters the HHI correction. HHI is enhanced in a diffusive transport regime, where $k_B T < \hbar/\tau_{tr}$ and is dependent on temperature [35, 36]. Altshuler and Aronov [35] developed the original framework describing HHI and Goh *et al.* [36] developed four methods that can be used to extract HHI from the temperature dependent Drude conductivity; in this thesis, as we show later, we exploit one of these methods to extract the HHI from all transport measurements in order to accurately access spin properties of the 2D hole band from the WL and WAL. The logarithmic temperature correction to the Drude conductivity due to the HHI is given by

$$\Delta\sigma_{HHI} = K_{hh} G_0 \ln\left(\frac{k_b T \tau}{\hbar}\right), \qquad (2.21)$$

where $G_0 = e^2/\pi h$, K_{hh} is the dimensionless HHI strength, T is the temperature and $\tau = \sigma_D m^*/pe^2$ is the transport relaxation time with p the areal hole density and m^* the effective hole mass for dispersion in the plane of the 2D system [36]. In this thesis, we adopted the value $m^* = 0.208 m_0$ for the 2D heavy hole mass [37]. As previously mentioned, the Drude conductivity σ_D can be determined either via a measurement of the conductivity at a sufficiently high temperature or at a high magnetic field, in either case the quantum interference effects (WL and WAL) must be completely suppressed. In this thesis, we measured the conductivity σ_{xx} at 20 and 30 K and used these measurements to define σ_D and hence to determine the transport relaxation time τ from the longitudinal conductivity. The complete method and explanation of the experimental determination of

$\Delta\sigma_{HHI}$, including the subsequent matrix manipulation required to extract σ_{xx} and σ_{xy} from measured values of ρ_{xx} and ρ_{xy} are described in details in Chapter 3 and its supplementary information.

All quantum corrections to the Drude conductivity that are explored in this thesis are described by three correction terms – $\Delta\sigma_{WL}$ due to weak localization, $\Delta\sigma_{WAL}$ due to weak anti-localization, and the HHI correction term $\Delta\sigma_{HHI}$:

$$\Delta\sigma(B) = \Delta\sigma_{WL}(B) + \Delta\sigma_{WAL}(B) + \Delta\sigma_{HHI}. \quad (2.\ 22)$$

References

1. *Research and Prototype Foundry* Available from: https://sydney.edu.au/research/facilities.html.
2. Madou, M.J., *Manufacturing techniques for microfabrication and nanotechnology*. Vol. 2. 2011: CRC press.
3. Robinson, J.A., et al., *Contacting graphene.* Applied Physics Letters, 2011. **98**(5): p. 053103.
4. Tsugawa, K., et al., *Schottky barrier heights, carrier density, and negative electron affinity of hydrogen-terminated diamond.* Physical Review B, 2010. **81**(4): p. 045303.
5. Wang, W., et al., *Palladium ohmic contact on hydrogen-terminated single crystal diamond film.* Diamond and Related Materials, 2015. **59**: p. 90-94.
6. Ignat'ev, N., et al., *New ionic liquids with tris (perfluoroalkyl) trifluorophosphate (FAP) anions.* Journal of Fluorine Chemistry, 2005. **126**(8): p. 1150-1159.
7. Balshaw, N., *Practical cryogenics. And introduction to laboratory cryogenics.* 1996.
8. Woodcraft, A.L., *An introduction to cryogenics.* Institute for Astronomy, Edinburgh University, Blackford Hill, Edinburgh, 2007.
9. Willems van Beveren, L., et al., *Overlapping-gate architecture for silicon Hall bar field-effect transistors in the low electron density regime.* Applied Physics Letters, 2010. **97**(15): p. 152102.
10. Bergmann, G., *Weak localization in thin films: a time-of-flight experiment with conduction electrons.* Physics Reports, 1984. **107**(1): p. 1-58.
11. Minkov, G., et al., *Weak antilocalization in quantum wells in tilted magnetic fields.* Physical Review B, 2004. **70**(15): p. 155323.
12. Jobst, J., *Quantum transport in epitaxial graphene on silicon carbide (0001)*. 2012, Universität Erlangen-Nürnberg: Germany.
13. Schäpers, T., *Semiconductor Spintronics*. 2016: Walter de Gruyter GmbH & Co KG.
14. Aharonov, Y. and D. Bohm, *Significance of electromagnetic potentials in the quantum theory.* Physical Review, 1959. **115**(3): p. 485.
15. Glazov, M. and L. Golub, *Spin–orbit interaction and weak localization in heterostructures.* Semiconductor Science and Technology, 2009. **24**(6): p. 064007.
16. Iordanskii, S., Y.B. Lyanda-Geller, and G. Pikus, *Weak localization in quantum wells with spin-orbit interaction.* ZhETF Pisma Redaktsiiu, 1994. **60**: p. 199.
17. Pikus, F. and G. Pikus, *Conduction-band spin splitting and negative magnetoresistance in A 3 B 5 heterostructures.* Physical Review B, 1995. **51**(23): p. 16928.
18. Bergmann, G., *Weak anti-localization—an experimental proof for the destructive interference of rotated spin 12.* Solid State Communications, 1982. **42**(11): p. 815-817.
19. Hikami, S., A.I. Larkin, and Y. Nagaoka, *Spin-orbit interaction and magnetoresistance in the two dimensional random system.* Progress of Theoretical Physics, 1980. **63**(2): p. 707-710.
20. Al'Tshuler, B., et al., *Anomalous magnetoresistance in semiconductors.* Sov. Phys. JETP, 1981. **54**(2): p. 411-419.
21. McPhail, S., et al., *Weak localization in high-quality two-dimensional systems.* Physical Review B, 2004. **70**(24): p. 245311.

22. Dresselhaus, G., *Spin-orbit coupling effects in zinc blende structures.* Physical Review, 1955. **100**(2): p. 580.
23. D'yakonov, M., *Spin relaxation of two-dimensional electrons in noncentrosymmetric semiconductors.* Sov. Phys. Semicond., 1986. **20**(1): p. 110-112.
24. Manchon, A., et al., *New perspectives for Rashba spin-orbit coupling.* Nature materials, 2015. **14**(9): p. 871-882.
25. Winkler, R., et al., *Spin orientation of holes in quantum wells.* Semiconductor science and technology, 2008. **23**(11): p. 114017.
26. Nakamura, H., T. Koga, and T. Kimura, *Experimental evidence of cubic Rashba effect in an inversion-symmetric oxide.* Physical review letters, 2012. **108**(20): p. 206601.
27. Moriya, R., et al., *Cubic rashba spin-orbit interaction of a two-dimensional hole gas in a strained-Ge/SiGe quantum well.* Physical review letters, 2014. **113**(8): p. 086601.
28. Dresselhaus, P., et al., *Observation of spin precession in GaAs inversion layers using antilocalization.* Physical review letters, 1992. **68**(1): p. 106.
29. Knap, W., et al., *Weak antilocalization and spin precession in quantum wells.* Physical Review B, 1996. **53**(7): p. 3912.
30. Mal'shukov, A., K. Chao, and M. Willander, *Magnetoresistance of a weakly disordered III-V semiconductor quantum well in a magnetic field parallel to interfaces.* Physical Review B, 1997. **56**(11): p. 6436.
31. Mal'shukov, A., V. Shlyapin, and K. Chao, *Effect of the spin-orbit geometric phase on the spectrum of Aharonov-Bohm oscillations in a semiconductor mesoscopic ring.* Physical Review B, 1999. **60**(4): p. R2161.
32. Gougam, A., et al., *Electron localization and anisotropic magnetoconductivity in GaAs-AlAs superlattices.* Physical Review B, 1999. **59**(23): p. 15308.
33. Meijer, F., et al., *Competition between spin-orbit interaction and Zeeman coupling in Rashba two-dimensional electron gases.* Physical Review B, 2004. **70**(20): p. 201307.
34. Cabañas, S., et al., *Suppression of weak antilocalization in an Al x Ga 1− x N/ Ga N two-dimensional electron gas by an in-plane magnetic field.* Physical Review B, 2007. **75**(19): p. 195329.
35. Altshuler, B.L. and A.G. Aronov, *Electron–electron interaction in disordered conductors*, in *Modern Problems in condensed matter sciences*. 1985, Elsevier. p. 1-153.
36. Goh, K., M. Simmons, and A. Hamilton, *Electron-electron interactions in highly disordered two-dimensional systems.* Physical Review B, 2008. **77**(23): p. 235410.
37. Edmonds, M.T., et al., *Spin–Orbit Interaction in a Two-Dimensional Hole Gas at the Surface of Hydrogenated Diamond.* Nano letters, 2014. **15**(1): p. 16-20.

3

Strong and Tunable Spin-Orbit Coupling in a Two-Dimension Hole Gas in Ionic-Liquid Gated Diamond Devices

3.1 Introduction

As we have discussed, hydrogen-terminated diamond at its surface exhibits a p-type conductivity with a 2D hole band, providing an opportunity to study the spin properties of holes. In this chapter, we engineered a device with strong spin-orbit interaction and developed and characterised a method of gating, using an ionic liquid, to control the hole sheet density and spin orbit coupling. By tuning hole sheet density, and the extent of asymmetric of the hole confinement potential, spin orbit coupling strength can be engineered. The spin properties of the hole band are probed by performing low temperature manetotransport measurements. Spin orbit splitting is determined through the observation of the phase coherent back scattering effects in the form of weak localization and weak anti-localization.

In this chapter we particularly focused on modulating the spin orbit splitting using ionic liquid which, at high gate bias, gives a spin splitting that greatly exceeds other 2D hole systems in terms of magnitude and tunability, and is comparable in strength to the best 2D electron systems. As we shall discuss, this is as a result of the Rashba effect which arises due to the highly asymmetric confinement potential.

The chapter is presented as a journal article and its supplementary information which was published in *Nano Letters* 16 (6), 3768-3773 (2016), "*Strong and Tunable Spin-Orbit Coupling in a Two-Dimensional Hole Gas in ionic-liquid gated Diamond Devices*", written by *G. Akhgar, O. Klochan, L. H. Willems van Beveren, M. T. Edmonds, F. Maier, B. J. Spencer, J. C. McCallum, L. Ley, A. R. Hamilton, C. I. Pakes*.

Author Contribution:

Akhgar led all stages of this work, from experimental planning, to device fabrication and measurement, analysis and modelling of the results and preparation of the manuscript. Spencer assisted with the design of the device photolithography mask and Edmonds and McCallum with the operation of the facilities required to fabricate the device. Maier prepared the ionic liquid. Klochan and Willems van Beveren assisted with the operation of the cryogenic refrigerator and the collection of data. Pakes, Hamilton and Ley assisted with the analysis of the results and preparation of the manuscript.

3.2 Journal Article (*Nano letters* 16.6 (2016): 3768-3773).

Strong and Tunable Spin-Orbit Coupling in a Two-Dimensional Hole Gas in Ionic-Liquid Gated Diamond Devices

Golrokh Akhgar*[1], Oleh Klochan[2], Laurens H. Willems van Beveren[3], Mark T. Edmonds[4], Florian Maier[5], Benjamin J. Spencer[1], Jeffrey C. McCallum[3], Lothar Ley[1,6], Alex R. Hamilton[2], and Christopher I. Pakes[§1]

[1] Department of Chemistry and Physics, La Trobe University, Victoria 3086, Australia

[2] School of Physics, University of New South Wales, Sydney, New South Wales 2052, Australia

[3] School of Physics, The University of Melbourne, Victoria 3010, Australia

[4] School of Physics, Monash University, Victoria 3800, Australia

[5] Chair of Physical Chemistry II, Universität Erlangen-Nürnberg, Egerlandstr. 3, D-91058 Erlangen, Germany

[6] Institute of Condensed Matter Physics, Universität Erlangen-Nürnberg, Staudt-Str. 1, D-91058 Erlangen, Germany

Hydrogen-terminated diamond possesses due to transfer doping a quasi two-dimensional (2D) hole accumulation layer at the surface with a strong, Rashba-type spin-orbit coupling that arises from the highly asymmetric confinement potential. By modulating the hole concentration and thus the potential using an electrostatic gate with an ionic-liquid dielectric architecture the spin-orbit splitting can be tuned from 4.6 - 24.5 meV with a concurrent spin relaxation length of 33 – 16 nm and hole sheet densities of up to 7.23×10^{13} cm^{-2}. This demonstrates a spin-orbit interaction of

unprecedented strength and tunability for a 2D hole system at the surface of a wide band-gap semiconductor. With a spin relaxation length that is experimentally accessible using existing nanofabrication techniques, this result suggests that hydrogen-terminated diamond has great potential for the study and application of spin transport phenomena.

The development of electronic materials and devices in which the spin-orbit interaction can be engineered is central to the realization of schemes for the study of spin-coherent transport and its application [1, 2]. Electronic materials with a quasi two-dimensional (2D) band-structure are well suited to this purpose on account of the high spin-orbit coupling that a number of 2D systems possesses due to their reduced symmetry and the ability to couple the system to an electrostatic gate. For example, spin-orbit effects due to Rashba or Dresselhaus coupling have been studied in InGaAs-based quantum wells and nanowires [3-10] and exploited to develop spin field effect transistors based on 2D electron systems [4, 11-16]. By comparison, there are far fewer investigations of 2D hole systems and the spin orbit coupling in these systems is generally far smaller than for electrons [17-19]. Here we report on a 2D hole system that surpasses in terms of the magnitude of spin splitting and its tunability even the best electron systems studied so far.

Diamond, when functionalised with hydrogen and exposed to moist air or to strongly electron accepting molecules, exhibits a sub-surface hole accumulation layer with carrier densities of the order of 10^{13} cm^{-2} induced by surface transfer doping [20, 21]. Recent improvements in diamond bulk and surface quality have permitted low disorder hydrogen-terminated samples to be fabricated which support metallic *p*-type conduction in the accumulation layer to low temperatures, consistent with a 2D Fermi liquid [22]. This has permitted the observation of spin-orbit interaction through the identification of phase

coherent quantum transport effects [23], motivating the study and application of spin phenomena in diamond. As a wide band-gap semiconductor, diamond benefits from well-developed semiconductor device architectures and fabrication techniques, along with the possibility of manipulating spin using electrostatic and magnetic fields. Due to the high chemical and electrochemical stability of the hydrogen-terminated surface, surface-conducting diamond devices are well suited to schemes for gating with an ionic liquid. Ionic liquids (ILs) – ionic melts with a melting point below 100°C - have been widely adopted for carrier control in field effect devices. Their high capacitance in the form of electric double layers at the IL-solid interface combined with their physical and chemical stability, low vapor pressure, and wide electrochemical window make them ideal to induce charge carrier densities as high as 10^{15} cm^{-2} in favorable cases [24-27].

In this paper we demonstrate that the spin-orbit interaction can be engineered in the 2D hole gas of a hydrogen-terminated (100) diamond device using an ionic-liquid gate to modulate the hole concentration in a Hall bar geometry. The variation in spin-orbit coupling is due to the asymmetry induced Rashba effect where the asymmetry is due to the high electric field perpendicular to the plane of the 2D accumulation layer accompanying the nearly triangular potential well that confines the holes to a thin (<1nm) subsurface layer [28]. Low-temperature magnetotransport measurements are employed to determine the spin-orbit coupling strength through the observation of weak anti-localization. Using the electrostatic gate, the hole carrier density could be varied between 1.1 and 7.23×10^{13} cm^{-2} with a concurrent variation in spin splitting due to spin-orbit interaction of 4.6 to 24.5 meV.

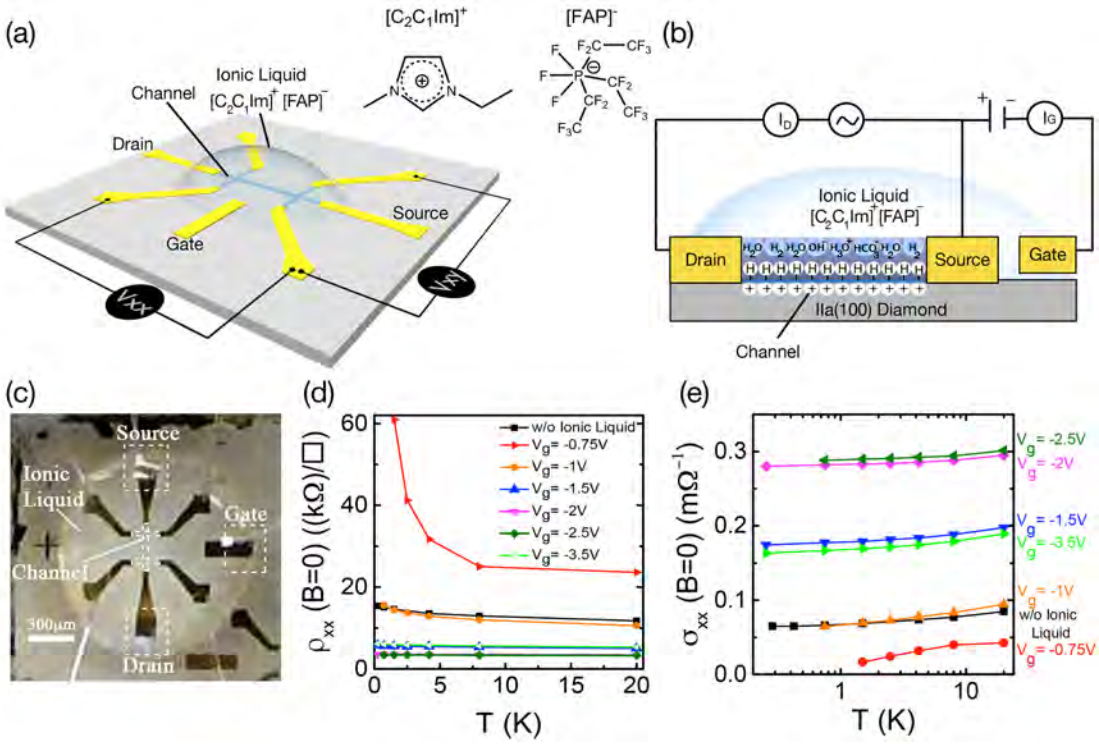

Figure 1: (a,b) device schematic; (c) optical image of the device; (d) temperature dependence of the zero-field resistivity, ρ_{xx}, recorded for different gate biases and without ionic liquid; (e) temperature dependence of $\sigma_{xx}(B = 0)$, with and without ionic liquid gating.

A commercial (Element 6) IIa (100) diamond single crystal sample was hydrogen-terminated in a microwave hydrogen plasma operating with a power of 1700 W at 850 °C for 10 minutes and rendered surface conducting via subsequent exposure to air. Hall bar devices with a width/length of 40μm/320μm were fabricated using standard photolithography and lift-off processing techniques. The Hall bar channel and contact regions are hydrogen terminated while the remainder of the sample was oxygen terminated via exposure to a 50W room temperature oxygen plasma for 10 minutes, rendering it insulating. Ti/Pt/Au (10/10/100 nm) layers were used to make Ohmic contacts to the Hall device and to form an isolated gate electrode separated from the device channel. Magnetotransport measurements were performed on the device both with and without an ionic liquid gate dielectric applied to the sample. For the latter case, a drop of the ionic liquid 1-ethyl-3-methyl-imidazolium tris (pentafluoroethyl) trifluorophosphate

$[C_2C_1Im]^+[FAP]^-$ was applied on top of the Hall bar device contacting the Hall channel and the gate electrode. Prior to measurements the IL was degassed in vacuum at RT for 24 hours. The complete device is depicted in Figures. 1(a-c). Magnetotransport measurements in vacuum were performed in the temperature range 0.25 - 20 K using an Oxford Instruments Heliox ^{3}He refrigerator with a 2 T superconducting magnet. Standard low-frequency ac lock-in techniques were employed to measure simultaneously the longitudinal voltage V_{xx} and transverse voltage V_{xy} in order to determine the corresponding resistivities ρ_{xx} and ρ_{xy} as a function of temperature, magnetic field strength, and gate bias, V_g. In order to insure full gate bias potential at the channel, V_g was applied above the IL's freezing temperature of 236 K when the ions are mobile before the sample was cooled to measurement temperature [29].

Figure. 1(d) shows the measured temperature dependence of the zero-field sheet resistivity. Previous studies of the surface conductivity in hydrogen-terminated diamond have shown carrier freeze-out at low temperatures and a thermally activated sheet conductivity, which were taken as indicative for localized band edge states and large scale potential fluctuations, respectively [30, 31]. For our sample, however, metallic conductivity prevails down to 250 mK as illustrated in Figure 1(d) for the bare device (without ionic liquid). With the ionic liquid in place and a low gate bias (V_g= - 0.75 V) the Hall channel is insulating at the lowest temperatures as was also observed by Yamaguchi *et al.*[22]. In this case the hole sheet density was observed to be higher than for the bare device but the hole mobility falls from 64.5cm^{2}V^{-1}s^{-1} to 23.3 cm^{2}V^{-1}s^{-1} when the ionic liquid was applied, giving the increase in ρ_{xx} shown in Figure 1(d). A reduction in mobility would result from increased disorder induced as a result of further processing of the device and due to charge inhomogeneity in the liquid layer that may arise from, for example, chemical interactions and thermal contraction of the liquid when it is frozen. A transition

back to metallic conductivity is observed with increasing gate bias. For $|V_g|$ in excess of 1 V and for the ungated device the measured zero-field conductivity, σ_{xx}, depends linearly on log(T) (Figure. 1 (e)) as it is expected for a 2D Fermi liquid [32].

Hole-hole interactions (HHI) and phase coherent back scattering (weak localization and weak anti-localization) are characteristic mechanisms that give rise to quantum corrections to the Drude conductivity in 2D systems at low temperature [33-36]. The contributions of these corrections can be separated using the fact that phase coherent backscattering does not affect the Hall resistivity, $\rho_{xy}(B)$, but causes a characteristic dependence of ρ_{xx}on magnetic field; in contrast, the HHI are independent of magnetic field but cause a ln(T) correction to the classical Drude Hall resistivity $\rho_{xy}(B)$, as shown in Figure. S1. To obtain the Drude conductivity and Hall resistance as a function of magnetic field and temperature we follow the approach of Goh *et al.*[32] to correct for HHI as described in the supplementary material. After subtracting the HHI correction from the Hall conductivity, all $\rho_{xy}(B)$ curves obtained for a given gate bias collapse onto a single, temperature independent line that represents the high temperature Drude limit. This is shown in Figure. S2. From the Drude limit of the Hall slope we obtain the hole sheet density which depends linearly on the applied gate bias (Figure. 2(a)) and is tunable from 1.1 to 7.23×10^{13} cm^{-2}. This is to our knowledge the highest air-induced 2D hole density observed so far for diamond. From the slope of the data in Figure 2a, an interfacial capacitance of 2.8 μFcm^{-2} has been deduced, which is slightly higher than the 2.1 μFcm^{-2} reported in Ref [22]. Figure. 2(b) shows that for all $V_g <$ -1 V. There is virtually no temperature dependence of the zero field resistivity ρ_{xx} after correction for HHI.

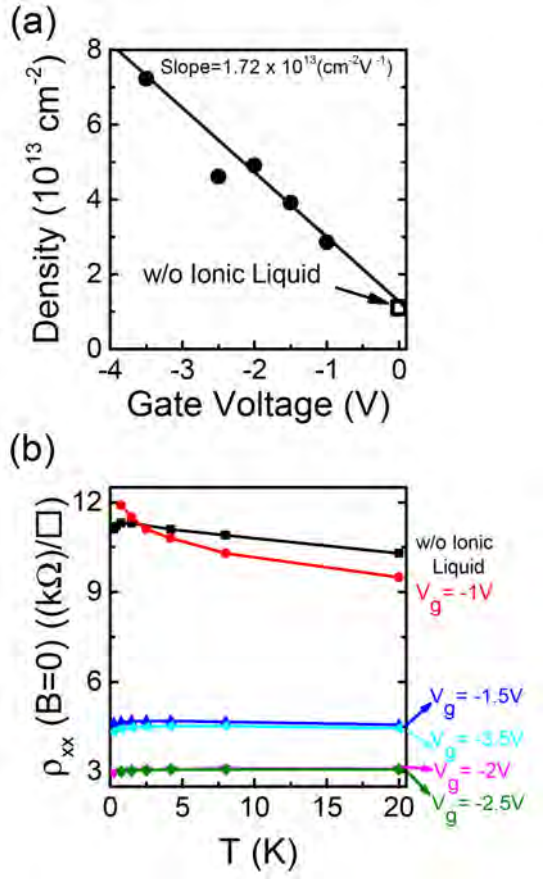

Figure 2: (a) hole sheet density obtained from the Hall resistance after subtraction of the HHI; (b) temperature dependence of ρ_{xx} after HHI correction.

To show that we can use the ionic liquid gate to tune the strength of the spin-orbit interaction, we now examine the magnetoconductivity. The magnetoconductivity $\sigma_{xx}(B)$ data before and after HHI corrections are plotted in Figure. S3 for different temperatures and in what follows we shall be only dealing with corrected quantities. Figures. 3(a-c) show for three representative temperatures and for several gate biases reduced magnetoconductivity data $\Delta\sigma = \sigma(B) - \sigma(B=0) = \rho_{xx}^{-1}(B) - \rho_{xx}^{-1}(0)$, an identity that holds for $\rho_{xx} >> \rho_{xy}$. Weak localization (WL) and weak anti-localization (WAL) cause characteristic cusps in the magnetoconductivity around $B = 0$ with negative (WL) and positive (WAL) magnetoconductivity, respectively. The change in magnetoconductivity from WL to WAL is illustrated by the upper curves in Figures. 3(a-c) for the bare Hall device (without IL) as a function of temperature. At 8 K (Figures. 3(c)) the positive

magnetoconductivity signals weak localization. As the temperature is lowered, a negative magnetoconductivity cusp develops at $B = 0$ due to weak anti-localization that is fully developed at T = 0.75 K (Figures. 3(a)). This is what had been observed earlier [23]. The novelty here is that the same transition from WL to WAL can also be driven by increasing the negative gate voltage as evident for all three temperatures. Because weak anti-localization is a characteristic signature of 2D systems that possess a strong spin-orbit coupling this result demonstrates gate control of the spin orbit interaction in the 2D hole system on diamond.

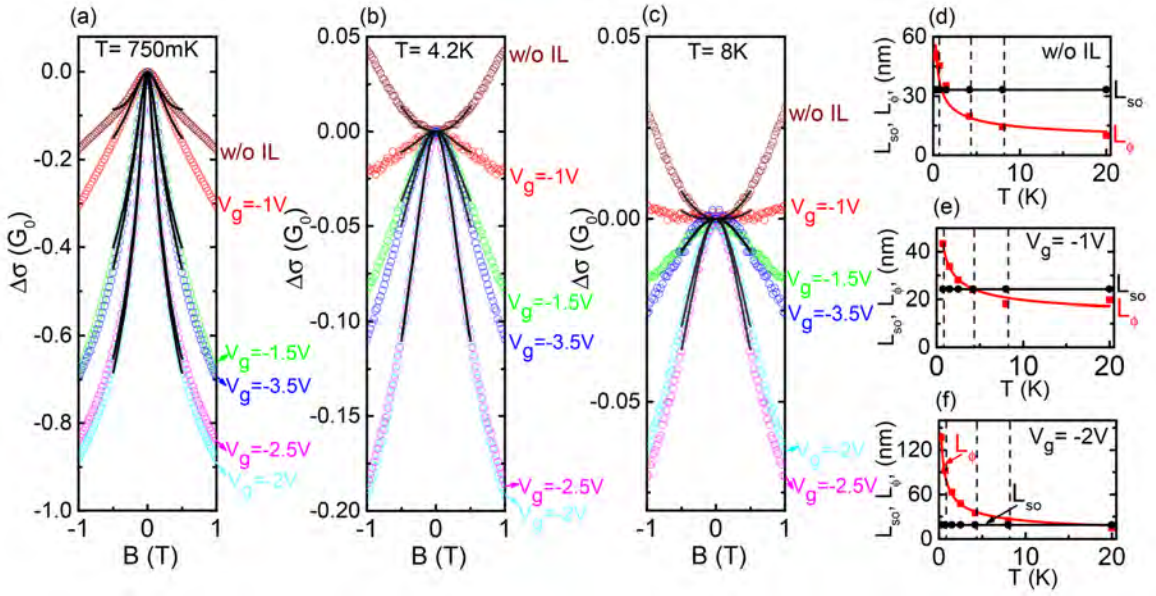

Figure 3: Reduced magnetoconductivity, $\Delta\sigma = \sigma(B) - \sigma(B = 0)$ (in units of $G_0 = e^2/\pi h$), for different temperatures and gate bias (a) 750 mK; (b) 4.2 K; (c) 8 K; the solid lines are fits to eq.1. Extracted temperature dependence of spin and phase coherence lengths L_{SO} and L_ϕ (d) without ionic liquid; (e) V_g= -1 V; (f) $V_g = -2\,V$; the vertical dashed lines are lines of constant temperature (750 mK, 4.2 K and 8 K).

WAL may arise from either a lack of inversion symmetry inherent in the underlying crystal structure (Dresselhaus mechanism) or from the asymmetry imposed by the electric field perpendicular to the 2D plane that is accompanying the triangular 2D confining potential for the holes (Rashba mechanism). For diamond with its inherent inversion symmetry only

the surface could contribute to the Dresselhaus splitting. Furthermore, the Dresselhaus splitting depends on the intrinsic atomic spin-orbit interaction, which in carbon is next to boron the smallest of all elements. On the other hand, the high hole sheet densities achieved here imply very strong electric fields perpendicular to the surface of 3.4 to 23×10^6 V/cm for hole concentrations of 1.1 to 7.23×10^{13} cm^{-2}. We therefore assume that Rashba driven WAL is the dominant mechanism. Following the discussion of Winkler *et al*.[37] and previous work on 2D hole systems in Ge [18, 19] we have fitted the experimental magnetoconductivity data to the expression for Rashba splitting proportional to the third power in the parallel wave vector *k*.[38, 39]

$$\Delta\sigma = -\frac{e^2}{2\pi^2\hbar}\left[\Psi\left(\frac{1}{2}+\frac{B_\phi+B_{so}}{B}\right)+\frac{1}{2}\Psi\left(\frac{1}{2}+\frac{B_\phi+2B_{so}}{B}\right)-\frac{1}{2}\Psi\left(\frac{1}{2}+\frac{B_\phi}{B}\right)-\ln\left(\frac{B_\phi+B_{so}}{B}\right)-\frac{1}{2}\ln\left(\frac{B_\phi+2B_{so}}{B}\right)+\frac{1}{2}\ln\left(\frac{B_\phi}{B}\right)\right], \quad (1)$$

where Ψ is the digamma function. From the fits (solid black lines in Figures. 3(a-c)) the phase and spin coherence fields, B_ϕ and B_{SO}, have been extracted (see Supplementary Material for further information).

The corresponding phase and spin coherence lengths are given by $L_\phi = (\hbar/(4eB_\phi))^{0.5}$ and $L_{SO} = (\hbar/(4eB_{SO}))^{0.5}$ respectively; they are plotted as a function of temperature for three gate voltages in Figures. 3(d-f). The data demonstrate control of the temperature independent spin coherence length, L_{SO}, with gate bias from 33 to 16 nm. In contrast, the phase coherence length L_ϕ is primarily determined by the temperature and does not depend on gate voltage in a systematic way (see below). The plots in Figures. 3(d-f) nicely demonstrate the key aspect of our experiment: whenever the phase coherence length exceeds the spin coherence length weak anti-localization is observed due to the spin

precession destroying the coherence of the wave functions of scattered holes on their time reversed closed path. As the hole density increases by raising V_g, the reduction in L_{SO} gives rise to the stronger WAL as evident in Figures. 3(a-c). The characteristic field B_{SO} and the coherence length L_{SO} vary with hole sheet density as shown in Figure. 4. B_{SO} increases linearly with hole sheet density, and it follows that L_{SO} is proportional to the inverse square-root of the hole density and both quantities are independent of temperature, as shown in Figures. 4(b,d).

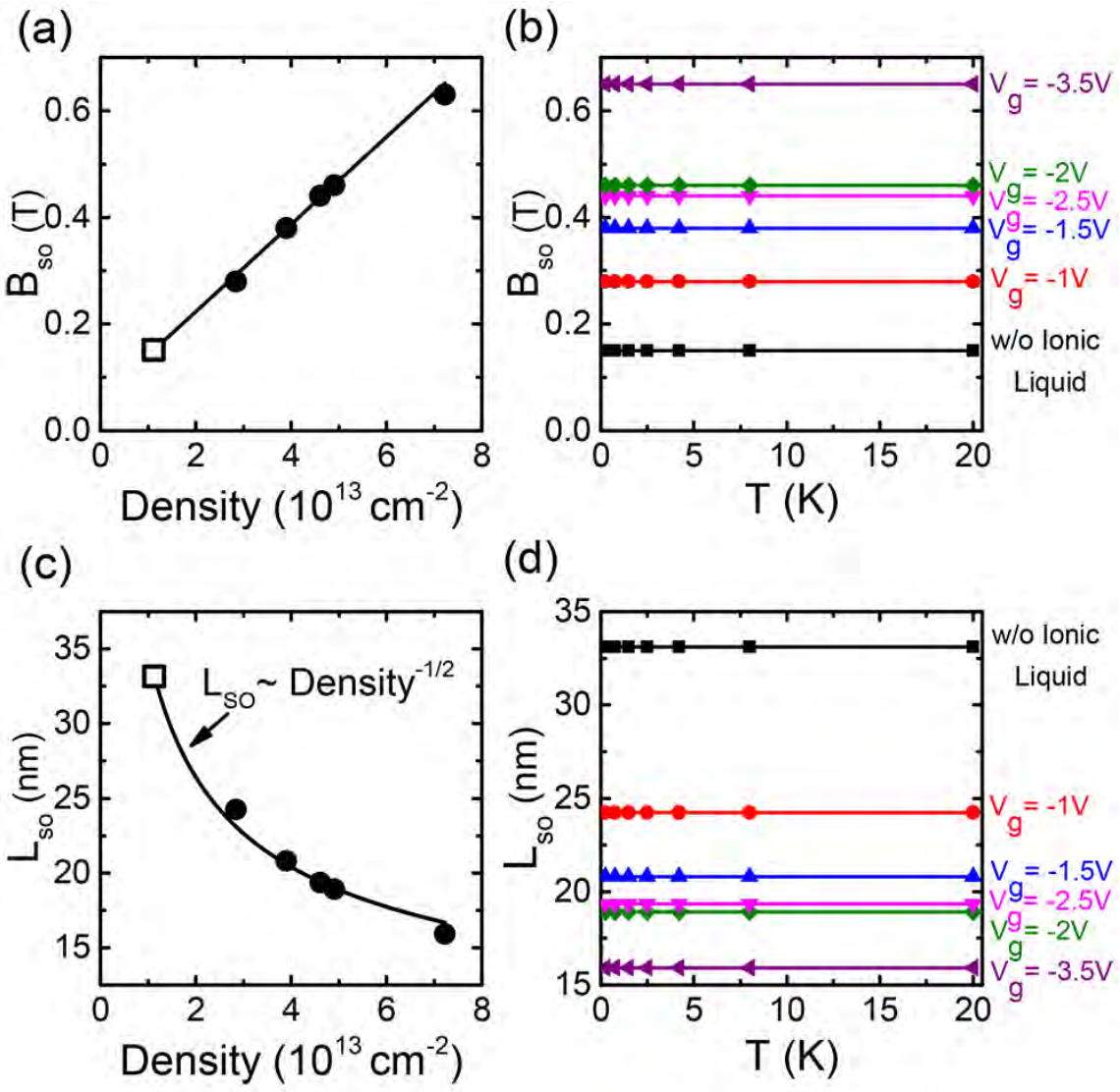

Figure 4: (a) Spin coherence field B_{so} as a function of hole density; (b) temperature dependence of B_{so} with gate voltage as parameter; (c) spin coherence length L_{so} as a function of hole density; (d) temperature dependence of L_{so} with gate voltage as parameter.

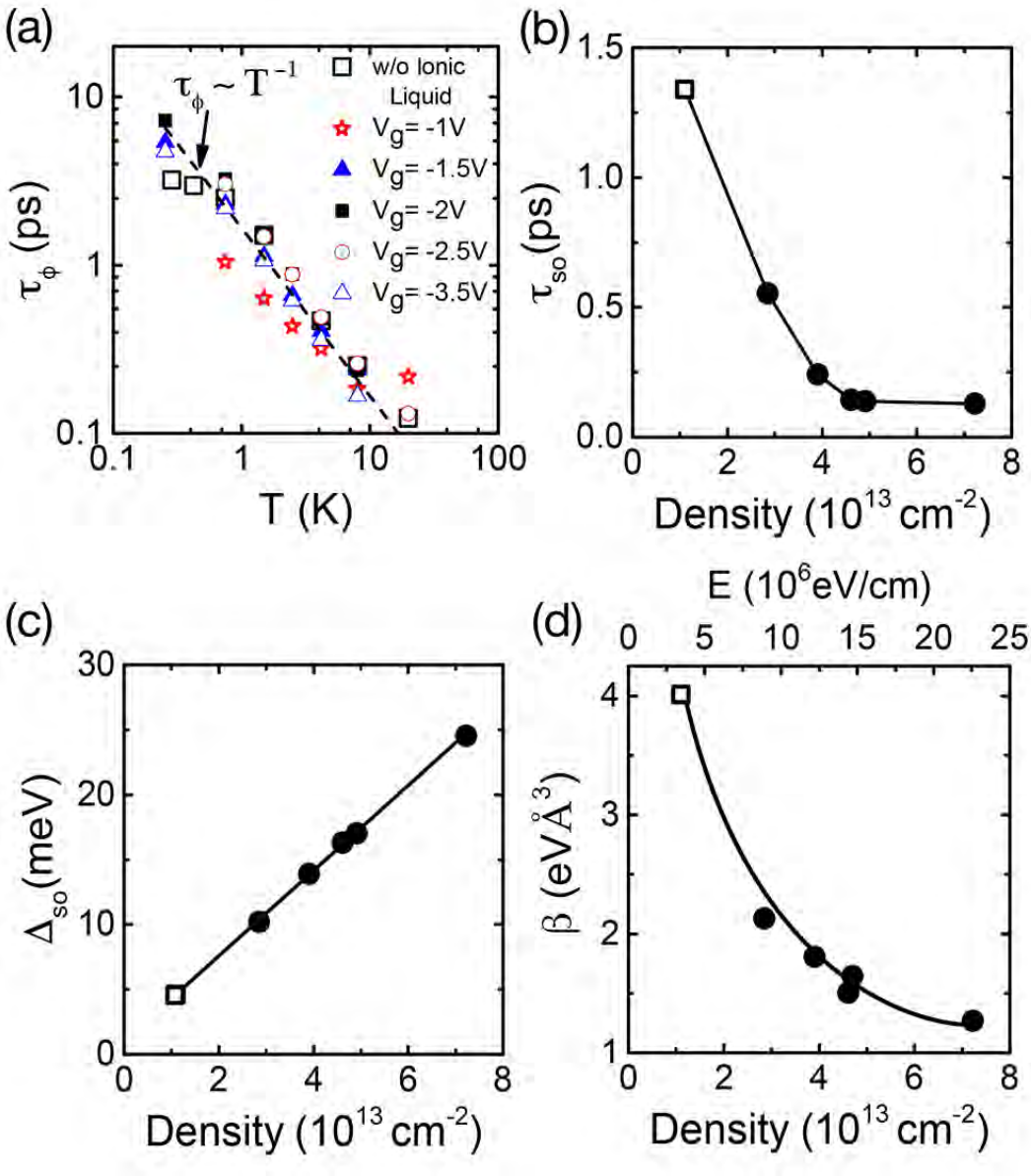

Figure 5: (a) Temperature dependence of the dephasing time (τ_ϕ) plotted at different gate biases; the broken line indicates $\tau_\phi \sim T^{-1}$ consistent with Nyquist dephasing; (b) dependence of the spin relaxation time (τ_{SO}) on hole density; the line is a guide to the eye; (c) tuning of the spin-orbit splitting strength, Δ_{SO}, with hole sheet density; the solid line is a linear fit to the data; (d) variation of k^3 Rashba coefficient, β, with hole sheet density; the line is a guide to the eye. The open squares represent the data obtained for the un-gated device in all figures.

Finally, we consider what effect tuning the hole sheet density has on the phase and spin-orbit relaxation times. The phase relaxation time $\tau_\phi = \hbar/(4eDB_\phi)$, illustrated in Figure. 5(a), scales as $\tau_\phi \sim T^{-1}$, with no systematic dependence on V_g. We take that as evidence

for a scattering mechanism consistent with Nyquist dephasing as expected in a weakly disordered 2D system despite the fact that Nyquist dephasing depends on the resistivity as well [32, 40]. In our experiments, however, T varies over two orders of magnitude, whereas the gate voltage induced change in resistivity covers a mere factor of four, so that the temperature dependence of τ_ϕ dominates. These results confirm that external noise and heating due to the applied source-drain current were kept to a minimum during the measurements at low temperature [41].

The spin relaxation time is given by $\tau_{SO} = \hbar/(4eDB_{SO})$, where the diffusion coefficient, D, depends on the hole density as described in the Supplementary Material. This yields a spin relaxation time $\tau_{SO} = 1.33$ ps for the un-gated device, which decreases by one order of magnitude as the spin-orbit interaction is strengthened in response to an increased hole sheet density (Figure. 5(b)). The corresponding spin-orbit splitting is given by Δ_{SO}=$\hbar/(2\tau\tau_{SO})^{1/2}$, where τ is the transport relaxation time, which is found to vary with gate bias in the range 2.8 – 7.6 fs (see Supplementary Material). The dependence of Δ_{SO} on hole density is illustrated in Figure. 5(c), demonstrating that the spin-orbit splitting can be tuned over a five-fold range from 4.6 - 24.5 meV by varying the gate voltage. Since we assume that the dominant spin-orbit interaction mechanism is k^3 Rashba-like we extract β, the spin orbit interaction strength, from the identity $4\beta^2 k_F^6 = \Delta_{so}^2 = \frac{2e\hbar D}{\tau} B_{so}$ where $k_F = (2\pi p)^{1/2}$ is the Fermi wave vector, p the areal hole concentration, and $m^* = 0.208\, m_0$ the effective heavy hole mass (assumed to be isotropic) for k in the (100) plane of the 2D hole gas [23]. The result as shown in Figure. 5(d) is at first sight surprising; instead of increasing with the symmetry breaking electric field E, β actually decreases with E. This, however, is not without precedent as it has been observed in other 2D hole systems and goes under the name of anomalous Rashba splitting or negative differential Rashba

splitting [42, 43]. The linear increase in Δ_{SO} with hole density and electric field is, of course, due to the overwhelming third power of k_F.

The values of the spin - orbit splitting Δ_{SO} derived here for a 2D hole system far outstrip other 2D hole systems reported so far in terms of magnitude and tunability. Spin splittings in the range of 0.1 to 0.4 meV and a tunability by gate voltage of about one tenth of that have been reported for strained InGaAs-type quantum wells [44] and in strained Ge quantum wells [18] while a spin-orbit splitting of 1.4 meV was achieved by Morrison *et al.* again in a strained Ge quantum well [19]. Even more important, our results exceed the spin splittings and the tuning range achieved in 2D electron systems realized for the most part in InGaAs – type quantum wells which cover the range from 1 to 10 meV [4-10]. Spin splitting of a magnitude comparable to ours albeit in a 2D electron system has only been reported for a HgTe quantum well where large intrinsic spin-orbit coupling, a small band gap, and an inverted band structure concur to bring about a spin splitting of up to 30 meV [45].

In summary, the results presented here show that surface-conducting hydrogen-terminated diamond possesses a 2D hole gas with a spin-orbit coupling that is among the strongest measured so far. It arises from the highly asymmetric surface confinement potential of the holes. By modulating the carrier concentration via an ionic-liquid based gate, a hole sheet density of up to 7.23×10^{13} cm^{-2} was achieved, with a concurrent spin-orbit splitting of 24.5 meV, along with the ability to tune the spin-orbit splitting over a five-fold dynamic range. The ability to engineer the spin-orbit interaction, coupled to the fact that existing nanofabrication techniques can be used to make devices on the scale of the spin and phase coherence lengths reported here, suggest that spin-coherent transport devices such as spin-FET [1, 46], may be experimentally accessible in hydrogen-terminated diamond.

Corresponding Authors

*Email: g.akhgar@latrobe.edu.au; §Email: c.pakes@latrobe.edu.au

Supporting Information

Technical information and figures on the hole-hole interaction correction and fitting the magnetoconductivity data to 2D localization theory.

Acknowledgments

This work was supported by the Australian Research Council under the Discovery Project (DP150101673) and Discovery Early Career Research Awards (DE140100775) schemes. This work was performed in part at the University of Sydney: Bandwidth Foundry International, part of the OptoFab node of the Australian National Fabrication Facilities.

References

1. Awschalom, D.D. and M.E. Flatté, *Challenges for semiconductor spintronics.* Nature Physics, 2007. **3**(3): p. 153-159.
2. Manchon, A., et al., *New perspectives for Rashba spin-orbit coupling.* Nature materials, 2015. **14**(9): p. 871-882.
3. Liang, D. and X.P. Gao, *Strong tuning of Rashba spin–orbit interaction in single InAs nanowires.* Nano letters, 2012. **12**(6): p. 3263-3267.
4. Koo, H.C., et al., *Control of spin precession in a spin-injected field effect transistor.* Science, 2009. **325**(5947): p. 1515-1518.
5. Nitta, J., et al., *Gate Control of Spin-Orbit Interaction in an Inverted I n 0.53 G a 0.47 As/I n 0.52 A l 0.48 As Heterostructure.* Physical Review Letters, 1997. **78**(7): p. 1335.
6. Koga, T., et al., *Rashba spin-orbit coupling probed by the weak antilocalization analysis in InAlAs/InGaAs/InAlAs quantum wells as a function of quantum well asymmetry.* Physical review letters, 2002. **89**(4): p. 046801.
7. Akabori, M., et al., *Realization of In0. 75Ga0. 25As two-dimensional electron gas bilayer system for spintronics devices based on Rashba spin-orbit interaction.* Journal of Applied Physics, 2012. **112**(11): p. 113711.
8. Kim, K.-H., et al., *Gate-Controlled Spin-Orbit Interaction in InAs High-Electron Mobility Transistor Layers Epitaxially Transferred onto Si Substrates.* ACS nano, 2013. **7**(10): p. 9106-9114.
9. Park, Y.H., et al., *Observation of gate-controlled spin—orbit interaction using a ferromagnetic detector.* Journal of Applied Physics, 2012. **111**(7): p. 07C317.
10. Zhou, Y., et al., *Experimental approaches to zero-field spin splitting in a gated high-mobility In 0.53 Ga 0.47 As/InP quantum well structure: Weak antilocalization and beating pattern.* Journal of Applied Physics, 2010. **107**: p. 053708.
11. Caviglia, A., et al., *Tunable Rashba spin-orbit interaction at oxide interfaces.* Physical review letters, 2010. **104**(12): p. 126803.
12. Balakrishnan, J., et al., *Colossal enhancement of spin-orbit coupling in weakly hydrogenated graphene.* Nature Physics, 2013. **9**(5): p. 284-287.
13. Chuang, P., et al., *All-electric all-semiconductor spin field-effect transistors.* Nature nanotechnology, 2015. **10**(1): p. 35-39.
14. Zhang, S., et al., *Generation of Rashba Spin–Orbit Coupling in CdSe Nanowire by Ionic Liquid Gate.* Nano letters, 2015. **15**(2): p. 1152-1157.
15. Chang, J., et al., *Injection, detection and gate voltage control of spins in the spin field effect transistor.* Journal of Applied Physics, 2011. **109**(10): p. 102405.
16. Kum, H., et al., *Electric field control of magnetoresistance in a lateral InAs quantum well spin valve.* Applied Physics Letters, 2009. **95**(21): p. 2503.
17. Hu, B., et al., *High mobility two-dimensional hole system on hydrogen-terminated silicon (111) surfaces.* Applied Physics Letters, 2012. **100**(25): p. 252107.
18. Moriya, R., et al., *Cubic rashba spin-orbit interaction of a two-dimensional hole gas in a strained-Ge/SiGe quantum well.* Physical review letters, 2014. **113**(8): p. 086601.
19. Morrison, C., et al., *Observation of Rashba zero-field spin splitting in a strained germanium 2D hole gas.* Applied Physics Letters, 2014. **105**(18): p. 182401.
20. Maier, F., et al., *Origin of surface conductivity in diamond.* Physical review letters, 2000. **85**(16): p. 3472.
21. Strobel, P., et al., *Surface transfer doping of diamond.* Nature, 2004. **430**(6998): p. 439-441.

22. Yamaguchi, T., et al., *Low-Temperature Transport Properties of Holes Introduced by Ionic Liquid Gating in Hydrogen-Terminated Diamond Surfaces.* Journal of the Physical Society of Japan, 2013. **82**(7): p. 074718.
23. Edmonds, M.T., et al., *Spin–Orbit Interaction in a Two-Dimensional Hole Gas at the Surface of Hydrogenated Diamond.* Nano letters, 2014. **15**(1): p. 16-20.
24. Fujimoto, T. and K. Awaga, *Electric-double-layer field-effect transistors with ionic liquids.* Physical Chemistry Chemical Physics, 2013. **15**(23): p. 8983-9006.
25. Yuan, H., et al., *High-Density Carrier Accumulation in ZnO Field-Effect Transistors Gated by Electric Double Layers of Ionic Liquids.* Advanced Functional Materials, 2009. **19**(7): p. 1046-1053.
26. Taniguchi, K., et al., *Electric-field-induced superconductivity at 9.4 K in a layered transition metal disulphide MoS2.* Applied Physics Letters, 2012. **101**(4): p. 042603.
27. Ono, S., et al., *High-performance n-type organic field-effect transistors with ionic liquid gates.* Appled Physics Letters, 2010. **97**: p. 143307.
28. Edmonds, M., C. Pakes, and L. Ley, *Self-consistent solution of the Schrödinger-Poisson equations for hydrogen-terminated diamond.* Physical Review B, 2010. **81**(8): p. 085314.
29. Ignat'ev, N., et al., *New ionic liquids with tris (perfluoroalkyl) trifluorophosphate (FAP) anions.* Journal of Fluorine Chemistry, 2005. **126**(8): p. 1150-1159.
30. Nebel, C., et al., *Hydrogen-induced transport properties of holes in diamond surface layers.* Applied physics letters, 2001. **79**(27): p. 4541-4543.
31. Garrido, J., T. Heimbeck, and M. Stutzmann, *Temperature-dependent transport properties of hydrogen-induced diamond surface conductive channels.* Physical Review B, 2005. **71**(24): p. 245310.
32. Goh, K., M. Simmons, and A. Hamilton, *Electron-electron interactions in highly disordered two-dimensional systems.* Physical Review B, 2008. **77**(23): p. 235410.
33. Al'Tshuler, B., et al., *Anomalous magnetoresistance in semiconductors.* Sov. Phys. JETP, 1981. **54**(2): p. 411-419.
34. Bychkov, Y.A. and E.I. Rashba, *Oscillatory effects and the magnetic susceptibility of carriers in inversion layers.* Journal of physics C: Solid state physics, 1984. **17**(33): p. 6039.
35. Dresselhaus, P., et al., *Observation of spin precession in GaAs inversion layers using antilocalization.* Physical review letters, 1992. **68**(1): p. 106.
36. Bergmann, G., *Weak localization in thin films: a time-of-flight experiment with conduction electrons.* Physics Reports, 1984. **107**(1): p. 1-58.
37. Winkler, R., et al., *Spin orientation of holes in quantum wells.* Semiconductor science and technology, 2008. **23**(11): p. 114017.
38. Lyanda-Geller, Y.B. and G. Pikus, *Weak localization in quantum wells with spinorbit interaction.* JETP Lett, 1994. **60**(3).
39. Knap, W., et al., *Weak antilocalization and spin precession in quantum wells.* Physical Review B, 1996. **53**(7): p. 3912.
40. Altshuler, B.L., A. Aronov, and D. Khmelnitsky, *Effects of electron-electron collisions with small energy transfers on quantum localisation.* Journal of Physics C: Solid State Physics, 1982. **15**(36): p. 7367.
41. Hao, X.-J., et al., *Strong and Tunable Spin− Orbit Coupling of One-Dimensional Holes in Ge/Si Core/Shell Nanowires.* Nano letters, 2010. **10**(8): p. 2956-2960.

42. Winkler, R., et al., *Anomalous Rashba spin splitting in two-dimensional hole systems.* Physical Review B, 2002. **65**(15): p. 155303.
43. Habib, B., et al., *Negative differential Rashba effect in two-dimensional hole systems.* Applied physics letters, 2004. **85**: p. 3151.
44. Minkov, G., et al., *Antilocalization and spin-orbit coupling in the hole gas in strained Ga As/ In x Ga 1− x As/ Ga As quantum well heterostructures.* Physical Review B, 2005. **71**(16): p. 165312.
45. Gui, Y., et al., *Giant spin-orbit splitting in a HgTe quantum well.* Physical Review B, 2004. **70**(11): p. 115328.
46. Datta, S. and B. Das, *Electronic analog of the electro-optic modulator.* Applied Physics Letters, 1990. **56**(7): p. 665-667.

3.3 Supplementary Information

Strong and Tunable Spin-Orbit Coupling in a Two-Dimensional Hole Gas in Ionic-Liquid Gated Diamond Devices

Golrokh Akhgar*[1], Oleh Klochan[2], Laurens H. Willems van Beveren[3], Mark T. Edmonds[4], Florian Maier[5], Benjamin J. Spencer[1], Jeffrey C. McCallum[3], Lothar Ley[1,6], Alex R. Hamilton[2], and Christopher I. Pakes[§1]

[1] Department of Chemistry and Physics, La Trobe University, Victoria 3086, Australia

[2] School of Physics, University of New South Wales, Sydney, New South Wales 2052, Australia

[3] School of Physics, The University of Melbourne, Victoria 3010, Australia

[4] School of Physics, Monash University, Victoria 3800, Australia

[5] Chair of Physical Chemistry II, Universität Erlangen-Nürnberg, Egerlandstr. 3, D-91058 Erlangen, Germany

[6] Institute of Condensed Matter Physics, Universität Erlangen, Staudt-Str. 1, 91058 Erlangen, Germany

1. $[C_2C_1Im]^+[Fab]^-$ Ionic Liquid Chemistry

$[C_2C_1Im]^+[FAP]^-$ as gating ionic-liquid was used because of its very hydrophobic, stable, non-coordinating $[FAP]^-$ anion [1], and its wide electrochemical window for gold electrodes of about 5 V [2].

2. Hole-hole interaction correction and K_{hh} extraction

In 2D systems at low temperatures quantum corrections to the Drude conductivity are due to weak localization (WL), weak anti-localization (WAL) and hole-hole interactions (HHI). The effect of these corrections can be separated using the fact that phase coherent backscattering does not affect the Hall resistivity, $\rho_{xy}(B)$, but causes a characteristic dependence of ρ_{xx} on magnetic field; in contrast, the HHI are independent of magnetic field but cause a $\ln(T)$ correction $\Delta\sigma_{HHI}$ to the classical Drude conductivity, σ_D:

$$\Delta\sigma_{HHI} = K_{hh}G_0 \ln\left(\frac{k_b T\tau}{\hbar}\right), \tag{S1}$$

where $G_0 = e^2/\pi\mathrm{h}$, K_{hh} is the dimensionless Coulomb interaction strength, T the temperature and $\tau = \sigma_D m^*/pe^2$ is the transport relaxation time with p the areal hole density and m^* the effective hole mass for dispersion in the plane of the 2D system. We adopt the value $m^* = 0.208m_0$ for the 2D heavy hole mass [3], and equate σ_D to $\sigma_{xx}(20\,K)$ to obtain τ from the longitudinal conductivity. The values of σ_D and τ for different gate voltages are listed in Table SI.

We follow method II as described by Goh *et al.*[4] for determining a first approximation for K_{hh} by noting that K_{hh} is a factor in the $\ln(T)$ dependence of the HHI correction, ∂R_H, to the Hall resistance R_H as well. When ∂R_H is replaced by $\Delta R_H(T) = (R_H(T) - R_H(20\ \mathrm{K}))/R_H(20\ \mathrm{K})$ under the assumption that at $20K$ the Hall resistance approaches its Drude limit, K_{hh} is directly given by the slope of ΔR_H vs. $\ln(T)$ as shown in Figure. S1:

$$K_{hh} = -\frac{Hall\ slope \times \sigma_{xx}(20K)}{2G_0} \tag{S2}$$

Once τ and K_{hh} are determined, the B independent $\Delta\sigma_{HHI}$ is calculated from equation (S1) for all temperatures at each gate voltage. Then the corrected conductivity without HHI, $\sigma_{xx}^{Corrected}(B,T,V_g)$, is calculated by subtracting the $\Delta\sigma_{HHI}(B,T,V_g)$ from the original $\sigma_{xx}^{Measured}(B,T,V_g) \approx {1}/{\rho_{xx}^{Measured}(B,T,V_g)}$ (in the limit $\rho_{xy} \ll \rho_{xx}$ which holds in all cases here). After subtraction, a new $\rho_{xy}^{Corrected}(B,T,V_g) = \frac{\sigma_{xy}^{Measured}}{\sigma_{xx}^{2\,Corrected}}$, is calculated. The $\rho_{xy}^{Corrected}(B,T,V_g)$ vs. B traces for a given V_g should collapse onto one single trace to ensure the complete correction; if not, K_{hh} is systematically adjusted and $\Delta\sigma_{HHI}$ recalculated until they do collapse onto a single trace for each V_g. This process corrects for the approximation made earlier, namely that at $T = 20$ K the Drude limit without any HHI is reached. Figure. S2 shows the successful HHI removal by collapsing all the $\rho_{xy}^{Corrected}(B,T)$ traces onto one curve and the corresponding K_{hh} are collected in Table SI.

Figure. S3 shows the corresponding magnetoresistivity data before (solid lines) and after (dashed lines) HHI removal. The removal of the hole-hole interactions greatly reduces the temperature dependence of $\rho_{xx}^{Corrected}(B = 0)$, as shown in Figure. 2(b) of the main text.

The remaining parameters in Table SI are the hole mean free path, $l = ((2\pi)^{1/2}\hbar\sigma_D)/(e^2 p^{1/2})$, the diffusion constant, $D = l^2/(2\tau)$, and the transport magnetic field, $B_{tr} = \hbar/(2el^2)$.

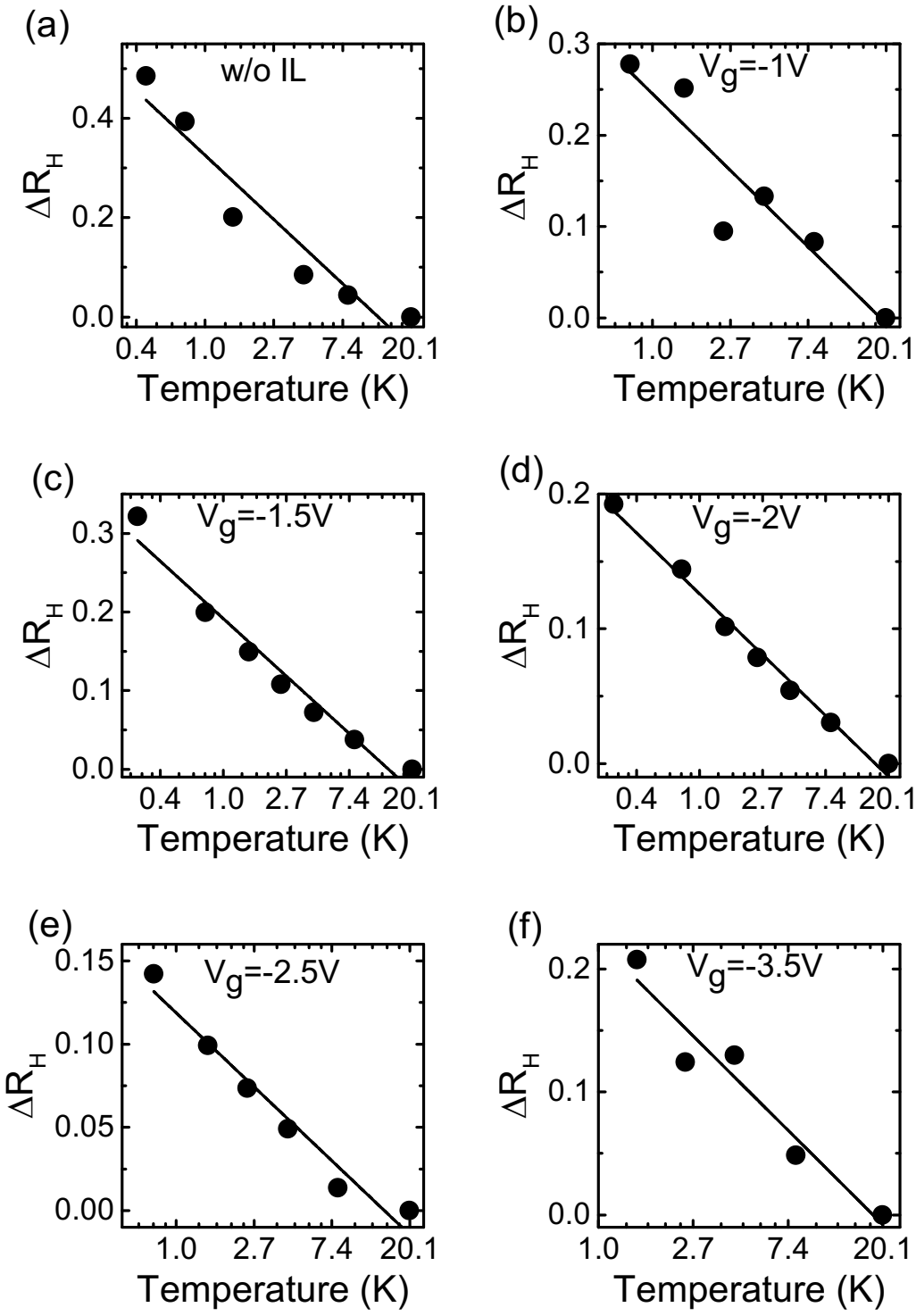

Figure S1: ΔR_H plotted as a function of temperature, showing logarithmic dependence on *T*. The value of K_{hh} is calculated from the slope as explained in the text.

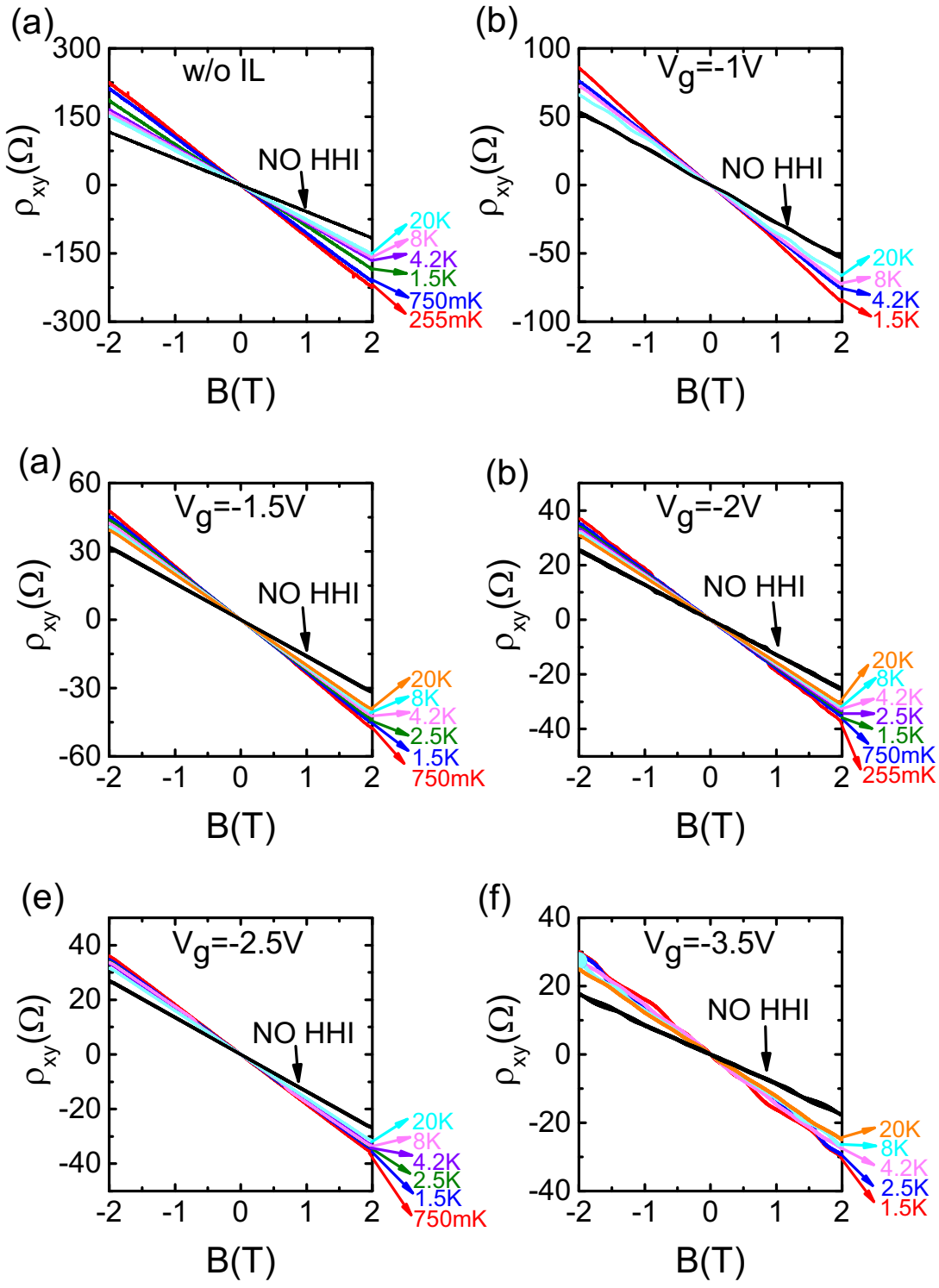

Figure S2: $\rho_{xy}(B)$ before and after HHI removal. $\rho_{xy}^{Corrected}(B)$ traces of all temperatures are collapsed onto one trace (black trace labeled as "NO HHI") after successful removal of $\Delta\sigma_{HHI}$ from the magnetotransport data.

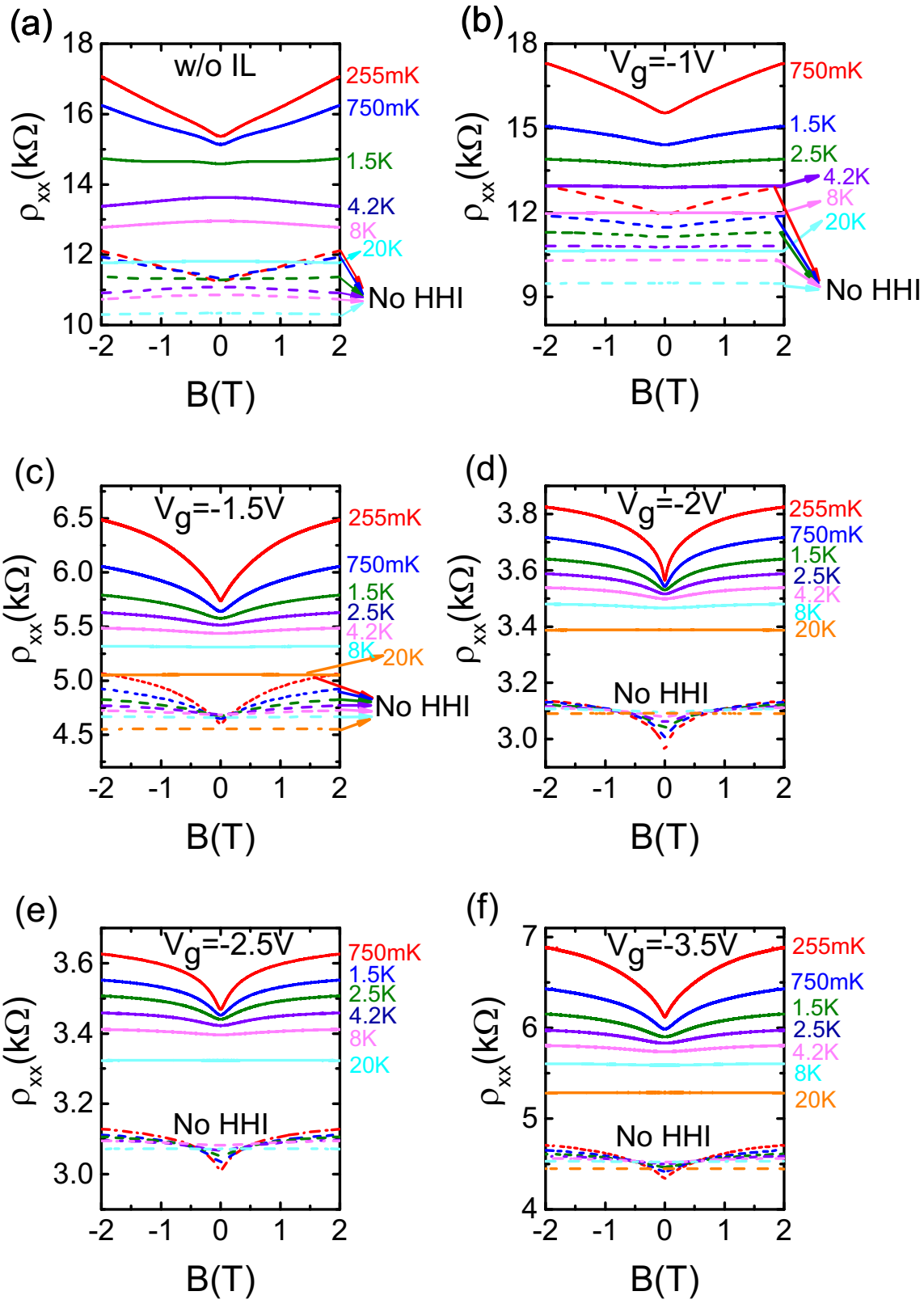

Figure S3: $\rho_{xx}(B)$ before (solid lines) and after (broken lines) successful removal of $\Delta\sigma_{HHI}$ from the magnetotransport data.

Table SI: Summary of calculated parameters during HHI correction

Gate Voltage V_g[V]	w/o IL	-1	-1.5	-2	-2.5	-3.5
Estimated Interaction strength, K_{hh}, obtained from the slope of $\Delta R_H(T)$ vs. $\ln(T)$	0.44	0.32	0.58	0.54	0.54	0.59
Interaction strength, K_{hh}, obtained from collapsing all $\rho_{xy}^{Measured}(B)$ onto one curve ($\rho_{xy}^{Corrected}(B)$)	0.25±0.01	0.20±0.01	0.400±0.001	0.540±0.001	0.475±0.001	0.59±0.01
hole density, *p,* before HHI removal $[10^{13}cm^{-2}]$ (20K)	0.82	1.84	3.13	3.91	3.91	4.96343
hole density, *p,* after HHI removal $[10^{13}cm^{-2}]$	1.10	2.85	3.91	4.91	4.61	7.23
Drude conductivity σ_D $[10^{-4}\Omega^{-1}]$ (20K)	1.14	1.47	2.47	3.61	3.55	2.75
transport relaxation time τ $[fs]$	7.61	3.76	4.6	5.43	5.69	2.81
mean free path l $[nm]$	3.53±0.05	2.83±0.09	4.07±0.02	5.31±0.03	5.39±0.02	3.34±0.04
diffusion coefficient D $[10^{-3}m^2s^{-1}]$	0.82±0.02	1.06±0.07	1.80±0.01	2.60±0.02	2.60±0.02	1.98±0.05
characteristic transport field B_{tr} $[T]$	26.4±0.7	41±1	19.9±0.2	11.7±0.1	11.33±0.08	29.6±0.7

3. Fitting the magnetoconductivity to obtain spin relaxation times and spin splitting

Figure. S4 shows the reduced magnetoconductivity data ($\Delta\sigma = \sigma_{xx}^{Corrected}(B) - \sigma_{xx}^{Corrected}(B=0)$) for different temperatures at each gate voltage. The solid black lines are fits of the data to the theoretical model for k^3-Rashba spin-orbit interaction for 2D holes [5, 6]:

$$\Delta\sigma = -\frac{e^2}{2\pi^2\hbar}\left[\Psi\left(\frac{1}{2}+\frac{B_\phi+B_{so}}{B}\right)+\frac{1}{2}\Psi\left(\frac{1}{2}+\frac{B_\phi+2B_{so}}{B}\right)-\frac{1}{2}\Psi\left(\frac{1}{2}+\frac{B_\phi}{B}\right)-\ln\left(\frac{B_\phi+B_{so}}{B}\right)-\frac{1}{2}\ln\left(\frac{B_\phi+2B_{so}}{B}\right)+\frac{1}{2}\ln\left(\frac{B_\phi}{B}\right)\right], \quad \text{(S3)}$$

where the meaning of the symbols have been explained in the main text.

The characteristic spin coherence field (B_{SO}) and phase coherence field (B_ϕ) are extracted from the fits. The magnetotransport data are fitted only in range of 0.5 T to -0.5 T, since equation S3 is only valid in the low-field diffusive limit. For a given curve, B_{SO} and B_ϕ turned out to be somewhat correlated. On the other hand, best fits for a given gate voltage gave B_{SO} values that varied randomly by only a few percent as a function of temperature. We therefore kept B_{SO} fixed at its average value for each gate voltage in a second run to determine the final B_ϕ values. The final B_{SO} and B_ϕ values, extracted from fits with a typical reduced chi-squared in the range 0.00001 to 0.04, are plotted as a function of temperature in Figure. S5. The errors in B_{SO} and B_ϕ associated with the fitting procedure are typically 0.003 T and 0.02 T respectively. B_ϕ decreases linearly with temperature and approaches zero as T→0 due to Nyquist dephasing [7, 8]. The spin coherence length ($L_{SO} = (\hbar/(4eB_{SO}))^{0.5}$) and phase coherence length ($L_\phi = (\hbar/(4eB_\phi))^{0.5}$) are plotted as a

function temperature in Figure. S6. L_ϕ varies with temperature according to $L_\phi \sim T^{-0.5}$, with an exponent that is expected for a 2D in contrast to a 3D system [7].

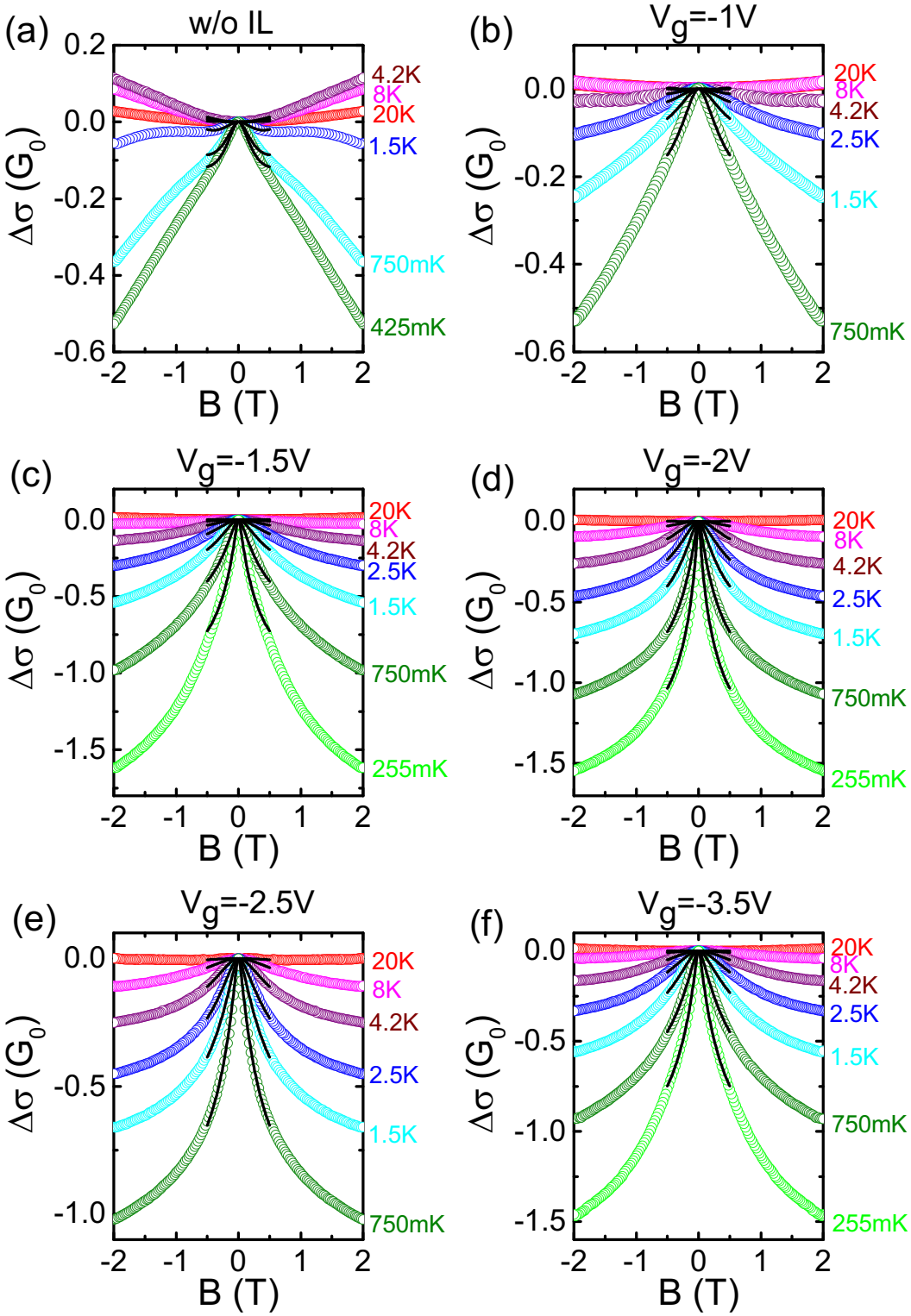

Figure S4: Reduced magnetoconductivity (in units of $G_0 = e^2/\pi h$), at different temperatures for all gate voltages. The black solid lines correspond to fits to equation S3.

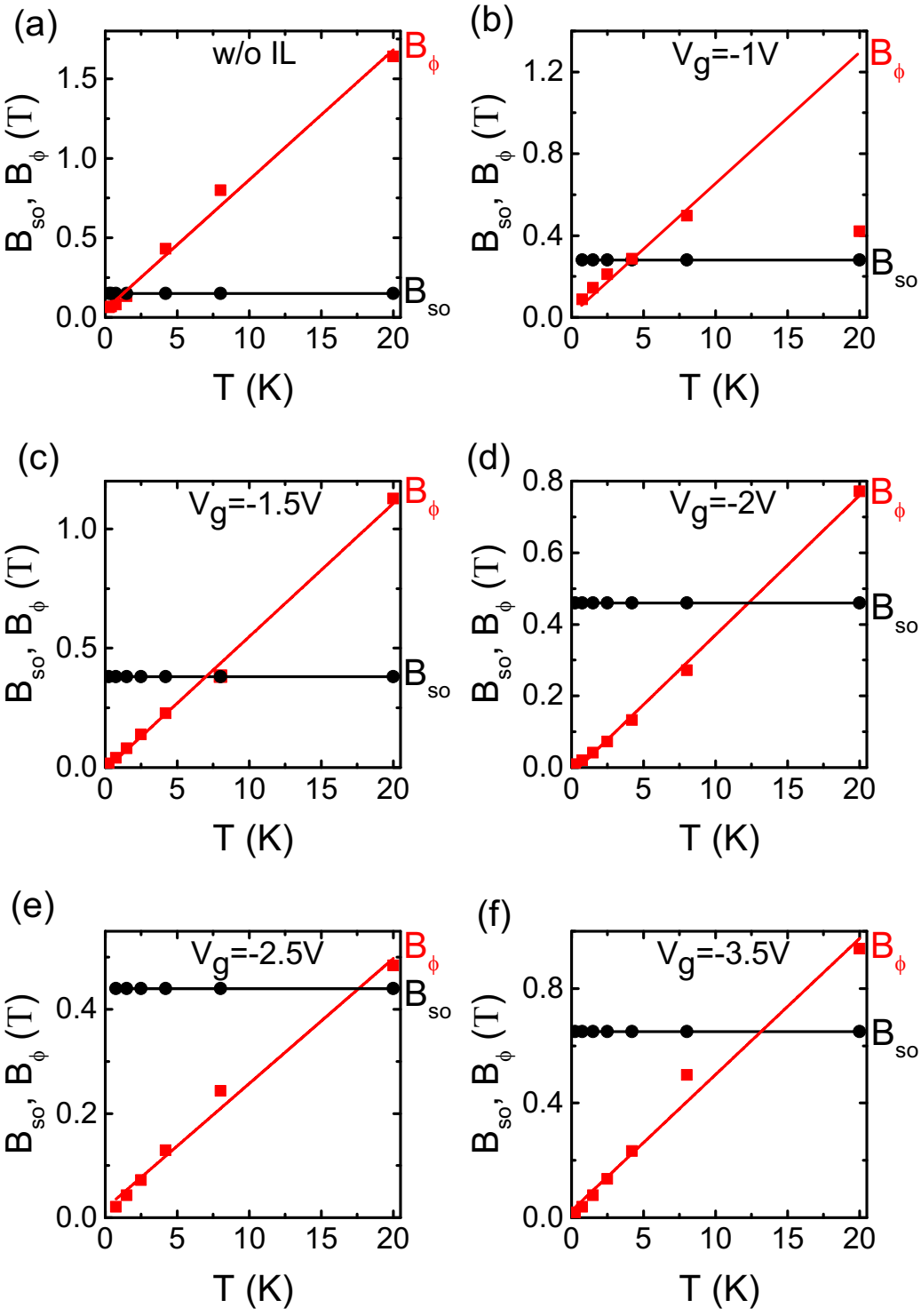

Figure S5: Temperature dependence of the characteristic spin coherence fields, B_{SO}, (black circle) and phase coherence fields, B_{ϕ}, (red square) with gate voltage V_g as parameter. The lines are linear fits to the data.

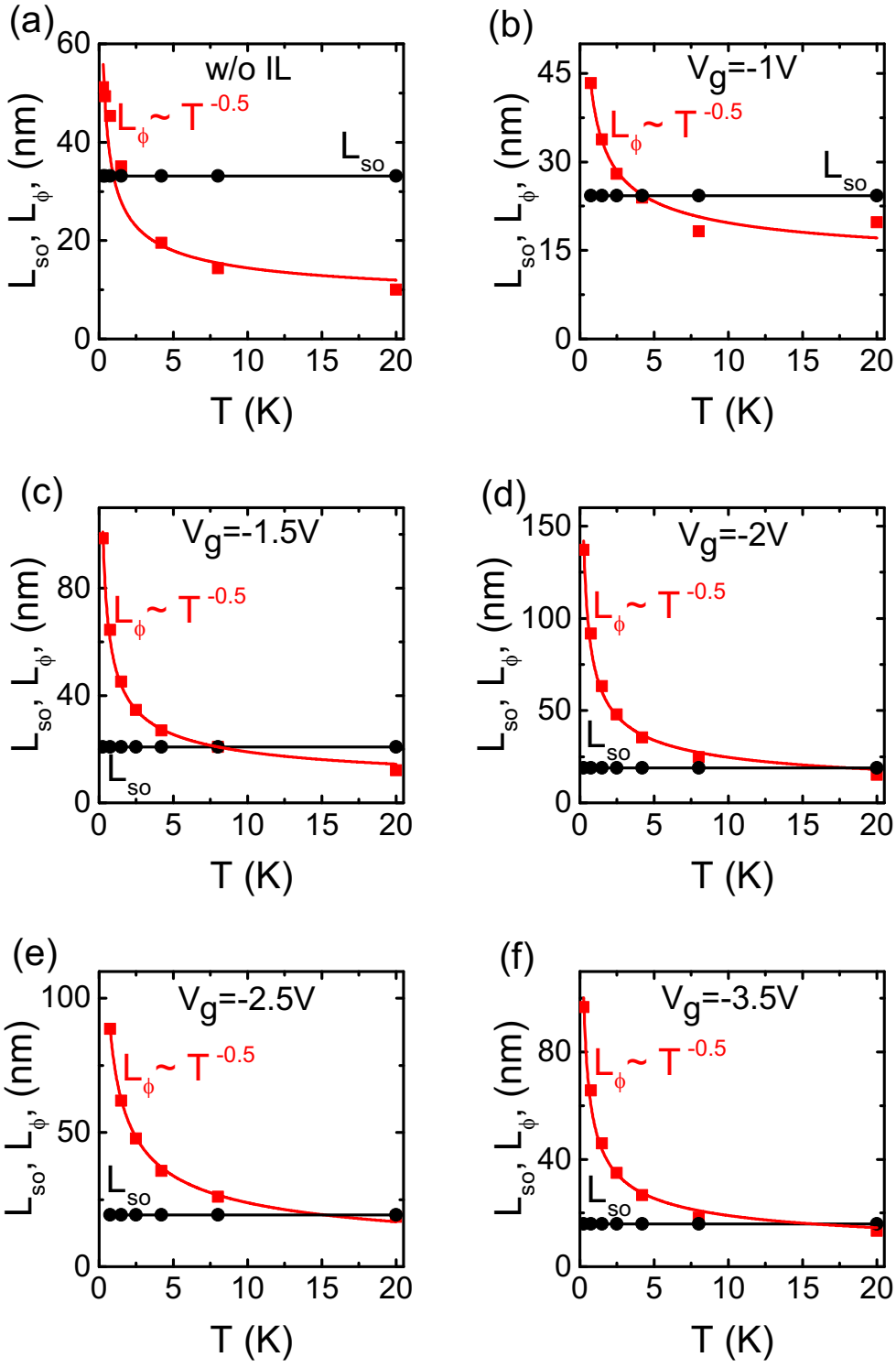

Figure S6: Temperature dependence of the characteristic spin coherence lengths, L_{SO}, (black circle) and phase coherence lengths, L_ϕ, (red square) with gate voltage V_g as parameter. The lines represent a linear fit to the data for L_{SO} and $T^{-0.5}$ fit for L_ϕ.

4. Fitting the magnetoconductivity to obtain spin relaxation times assuming Dresselhaus spin-orbit interaction

While we are convinced that the proper spin-orbit coupling mechanism is of k^3-Rashba type, we realized that fits of comparable quality could also be obtained assuming a Dresselhaus spin-orbit interaction [3]:

$$\Delta\sigma = -\frac{e^2}{2\pi^2\hbar}\left[\Psi\left(\frac{1}{2}+\frac{B_{tr}+B_{so}}{B}\right)+\frac{1}{2}\Psi\left(\frac{1}{2}+\frac{B_\phi}{B}\right)-\frac{3}{2}\Psi\left(\frac{1}{2}+\frac{B_\phi}{B}+\frac{4B_{so}}{3B}\right)-\ln\left(\frac{B_{tr}+B_{so}}{B}\right)-\frac{1}{2}\ln\left(\frac{B_\phi}{B}\right)+\frac{3}{2}\ln\left(\frac{B_\phi}{B}+\frac{4B_{so}}{3B}\right)\right]. \quad \text{(S4)}$$

The extracted phase coherence fields, B_ϕ, are very similar in fits to both models. The spin coherence fields, B_{so}, extracted from k^3-Rashba and Dresselhaus fits are compared in Figure. S7. In both cases B_{so} scales linearly with carrier density albeit with a slightly different slope.

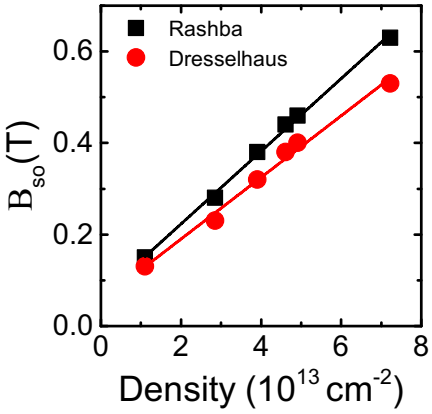

Figure S7: B_{SO} as a function of density using Rashba (eq. S3) and Dresselhaus (eq. S4) expressions to fit the magnetoconductivity data.

Corresponding Authors

*Email: g.akhgar@latrobe.edu.au; §Email: c.pakes@latrobe.edu.au

References

1. Ignat'ev, N., et al., *New ionic liquids with tris (perfluoroalkyl) trifluorophosphate (FAP) anions.* Journal of Fluorine Chemistry, 2005. **126**(8): p. 1150-1159.
2. Borisenko, N., S. Zein El Abedin, and F. Endres, *An in Situ STM and DTS study of the extremely pure [EMIM] FAP/Au (111) interface.* ChemPhysChem, 2012. **13**(7): p. 1736-1742.
3. Edmonds, M.T., et al., *Spin–Orbit Interaction in a Two-Dimensional Hole Gas at the Surface of Hydrogenated Diamond.* Nano letters, 2014. **15**(1): p. 16-20.
4. Goh, K., M. Simmons, and A. Hamilton, *Electron-electron interactions in highly disordered two-dimensional systems.* Physical Review B, 2008. **77**(23): p. 235410.
5. Lyanda-Geller, Y.B. and G. Pikus, *Weak localization in quantum wells with spinorbit interaction.* JETP Lett, 1994. **60**(3).
6. Knap, W., et al., *Weak antilocalization and spin precession in quantum wells.* Physical Review B, 1996. **53**(7): p. 3912.
7. Altshuler, B.L., A. Aronov, and D. Khmelnitsky, *Effects of electron-electron collisions with small energy transfers on quantum localisation.* Journal of Physics C: Solid State Physics, 1982. **15**(36): p. 7367.
8. Lee, P.A. and T. Ramakrishnan, *Disordered electronic systems.* Reviews of Modern Physics, 1985. **57**(2): p. 287.

4

G-factor and Well Width Variations for the Two-Dimensional Hole Gas in Surface Conducting Diamond

4.1 Introduction

In this Chapter, we quantified the Zeeman splitting and micro-roughness of the 2D hole gas at the hydrogen-terminated surface of diamond. Low temperature magnetotransport measurements are used as a powerful probe of phase coherent backscattering in the form of weak localization and weak anti-localization. By performing these measurements in the presence of an in-plane magnetic field additional dephasing mechanisms arising from Zeeman splitting and fluctuations in the 2D well width are probed.

From a systematic study of suppression of the weak anti-localization as the in-plane magnetic field is increased, the gyromagnetic ratio of the carriers in the 2D hole channel and the extent of fluctuations in the 2D confining well are determined. To our knowledge, these are the first published values of either for this system.

The results of this work have been published in *Applied Physics Letters* 112, 042102 (2018), *"G-factor and well width variations for the two-dimensional hole gas in surface conducting diamond", written by G. Akhgar, D. L. Creedon, L. H. Willems van Beveren, A. Stacey, D. I. Hoxley, J. C. McCallum, L. Ley, A. R. Hamilton, and C. I. Pakes.*

Author Contribution:

Akhgar led all stages of this work, from experimental planning, to device fabrication and measurement including atomic force microscopy imaging of the diamond surface, analysis and modelling of the results and preparation of the manuscript. Stacey prepared the hydrogen-terminated diamond surface. Creedon and Willems van Beveren assisted with the operation of the cryogenic refrigerator and the collection of data. Hoxley assisted with operation of the atomic force microscope. Pakes, Hamilton, McCallum and Ley assisted with the analysis of the results and preparation of the manuscript.

4.2 Journal Article (*Applied Physics Letters* 112.4 (2018): 042102).

G-factor and well width variations for the two-dimensional hole gas in surface conducting diamond

Golrokh Akhgar,*[1] Daniel L. Creedon,[2] Laurens H. Willems van Beveren,[2,3] Alastair Stacey,[2] David I. Hoxley,[1] Jeffrey C. McCallum,[2] Lothar Ley,[1,4] Alex R. Hamilton,[5] and Christopher I. Pakes§[1]

[1] Department of Chemistry and Physics, La Trobe University, Bundoora, Victoria 3086, Australia

[2] School of Physics, The University of Melbourne, Parkville, Victoria 3010, Australia

[3] National Measurement Institute, Lindfield, New South Wales 2070, Australia

[4] Institute of Condensed Matter Physics, Universität Erlangen, Staudt-Str. 1, 91058 Erlangen, Germany

[5] School of Physics, University of New South Wales, Sydney, New South Wales 2052, Australia

Hydrogen-terminated diamond possesses a quasi two-dimensional, sub-surface hole accumulation layer with a strong and tunable spin-orbit coupling due to surface transfer doping. We report a magnetoresistance study of the phase coherent backscattering (weak localization and antilocalization) at low temperatures. The response to an external magnetic field is highly anisotropic, confirming the 2D nature of the carriers despite the short mean free path. By simultaneously applying perpendicular and parallel magnetic fields we are able to probe the Zeeman interaction, and microroughness of the quantum well at the diamond surface. From a quantitative analysis of magnetoresistance curves at 2.5 K we derive a hole g-factor of 2.6 ± 0.1 and rms fluctuations in the width of the hole quantum well of about 3 nm over the phase coherence length of 33 nm. Well width fluctuations are ascribed to surface roughness and to lateral fluctuations in carrier density which self-consistently determines the width of the confining potential.

The spin properties of semiconductor materials with band structures of reduced dimensionality have attracted great interest on account of the high spin orbit coupling that

a number of these systems possess and their relevance to the development of devices for spin manipulation and transport [1, 2]. Studies in n-type InGaAs nanowires and two-dimensional (2D) quantum wells, for example, have shown spin orbit coupling due to Rashba or Dresselhaus effects [2-8], which have been exploited to develop spin field effect transistor devices [3, 6]. Diamond, when functionalized with hydrogen and exposed to moist air exhibits a subsurface 2D p-type accumulation layer induced by surface transfer doping [9]. The hole accumulation layer supports carrier densities up to $7x10^{13}$ cm^{-2} within a highly asymmetric quantum well that drives a strong spin-orbit interaction through the Rashba effect [10]. Low-temperature magnetoresistance measurements allow the observation of spin-orbit interaction through its effect on phase coherent quantum transport that leads to weak localization (WL) and weak anti-localization (WAL), respectively [10, 11]. The spin-orbit splitting is tunable through a variation in carrier density by a gate, for example, and is an order of magnitude greater than in other semiconductor 2D hole systems at its maximum [10]. What is missing for a complete characterization of the spin properties of the carriers in the hole accumulation layer is their g-factor which determines the coupling strength of the spins with an external magnetic field. As has been shown by Minkov et al.[12] this information is also available from the analysis of low temperature magnetoresistance (mr) data provided a magnetic field ($B_{\|}$) parallel to the plane of the 2D hole system is applied in addition to the perpendicular field used for the localization measurements. However, in addition to the Zeeman effect due to the parallel field, the combination of $B_{\|}$ and thickness variations of the 2D confining potential also influence the magnetoresistance. By performing systematic magnetoresistance measurements with $B_{\|}$ as a parameter we were able to extract both the hole g-factor and the rms well width variations of the 2D hole system in diamond from our data.

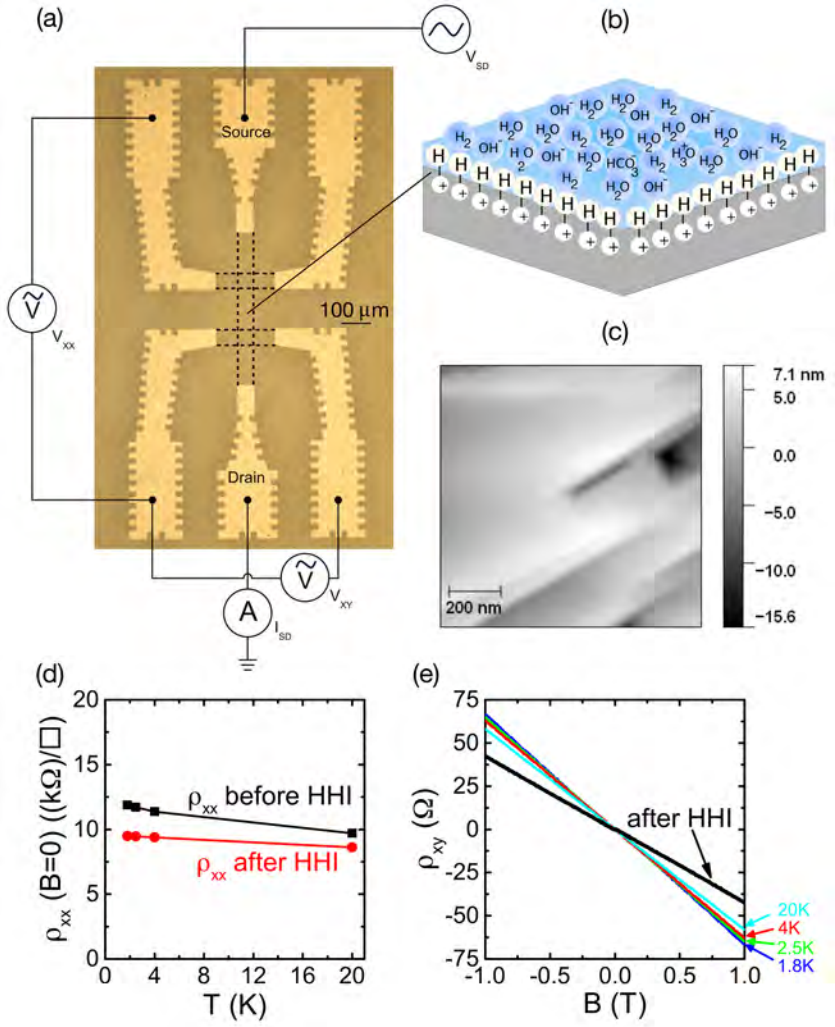

Figure. 1. (a) Optical image of the Hall bar showing the measurement schematic; (b) Surface doping scheme due to the presence of an adsorbed water layer on the hydrogen-terminated surface; (c) Atomic force microscopy image of the hydrogenated diamond surface; (d) Temperature dependence of ρ_{xx} (B=0) before and after subtraction of the HHI; (e) ρ_{xy} (B) before and after HHI removal. After subtraction of HHI, ρ_{xy} (B) traces of all temperature are collapse onto a single trace (labeled as "after HHI").

Surface conducting devices were fabricated using a commercial Type-IIa single crystal (100) diamond from Element Six. The sample was hydrogen terminated in a microwave hydrogen plasma using a power of 1500 W at 850 °C for 10 minutes, and then left in air for several days in order to create surface hole conduction through charge transfer doping with an adsorbed water layer. Water-based doping was chosen, rather than a synthetic acceptor layer from amongst the recently studied transition metal oxides [13], or fullerenes [14], because it permits a simpler device fabrication process which retains a high quality hydrogenated surface with reproducible hole densities maintained at low temperature [11]. A Hall bar device was fabricated (Figure 1a) with a 40 µm channel

width and 200 μm length using standard photolithography and lift-off processing techniques. The Hall bar channel and contact regions are hydrogen terminated and rendered conducting upon exposure to moist air (Figure 1b), while the rest of the substrate was oxygen terminated, and thus rendered insulating, via exposure to a 50 W room-temperature oxygen plasma. Palladium contact pads were then evaporated onto the conducting regions to form Ohmic contacts with a contact resistance of 1 kΩ at cryogenic temperatures. The edges of the contacts are perforated to improve adhesion of the Pd to the underlying diamond. Magnetotransport measurements were performed in the temperature range $1.8 - 20$ K using a Leiden Cryogenics dry dilution refrigerator with an integrated 9-1-1T superconducting vector magnet. The longitudinal resistivity ρ_{xx} and the Hall resistivity ρ_{xy} were measured using standard low-frequency ac lock-in techniques. Measurements were performed by sweeping the perpendicular magnetic field, B, from –1 to 1 T. The effect of an in-plane magnetic field, $B_{\|}$, was explored at temperatures of 4 K and 2.5 K using the vector magnet to apply a fixed in-plane magnetic field while sweeping the perpendicular field.

Figure 1(d) illustrates the temperature dependence of the zero-field sheet resistivity, showing almost temperature independent conductivity. The transport characteristics of this device match closely those of similar devices prepared in our laboratory and exhibit behaviour typical of a two-dimensional Fermi liquid [10, 11]. In such systems, hole-hole interactions (HHI) and phase coherent backscattering (weak localization (WL) and weak anti-localization (WAL)) give rise to quantum corrections to the classical Drude conductivity at low temperature. To study the effect of an applied magnetic field on the phase coherent backscattering it is necessary to first remove corrections due to HHI that are independent of magnetic field but introduce a temperature dependence in both ρ_{xx} and ρ_{xy}. This was achieved using the fact that HHI affects the Hall resistivity, $\rho_{xy}(B)$, whilst phase coherent backscattering does not. To remove the effects of HHI, the approach described by Goh *et.al.* [15]·[10] was employed to obtain the classical temperature-independent $\rho_{xy}(B)$ curve (Figure 1(e)). From this temperature independent Hall slope a corrected hole sheet density of $p = 1.45 \times 10^{13}\,\mathrm{cm}^{-2}$ and a mobility of $\mu = 50.1\,\mathrm{cm}^2\mathrm{V}^{-1}\mathrm{s}^{-1}$ is obtained without HHI interactions. Applying the same HHI correction to the longitudinal resistivity ρ_{xx} results in a further reduced temperature dependence as illustrated by the lower curve in Figure 1(d). The Drude conductivity at

20K was found to be $\sigma_D = 1.03 \times 10^{-4}\Omega^{-1}$, giving a mean free path $l = \frac{(2\pi)^{0.5}\hbar\sigma_D}{e^2 p^{0.5}} =$ 2.78 nm, and a characteristic transport field $B_{tr} = \frac{\hbar}{2el^2} = 42.5$ T.

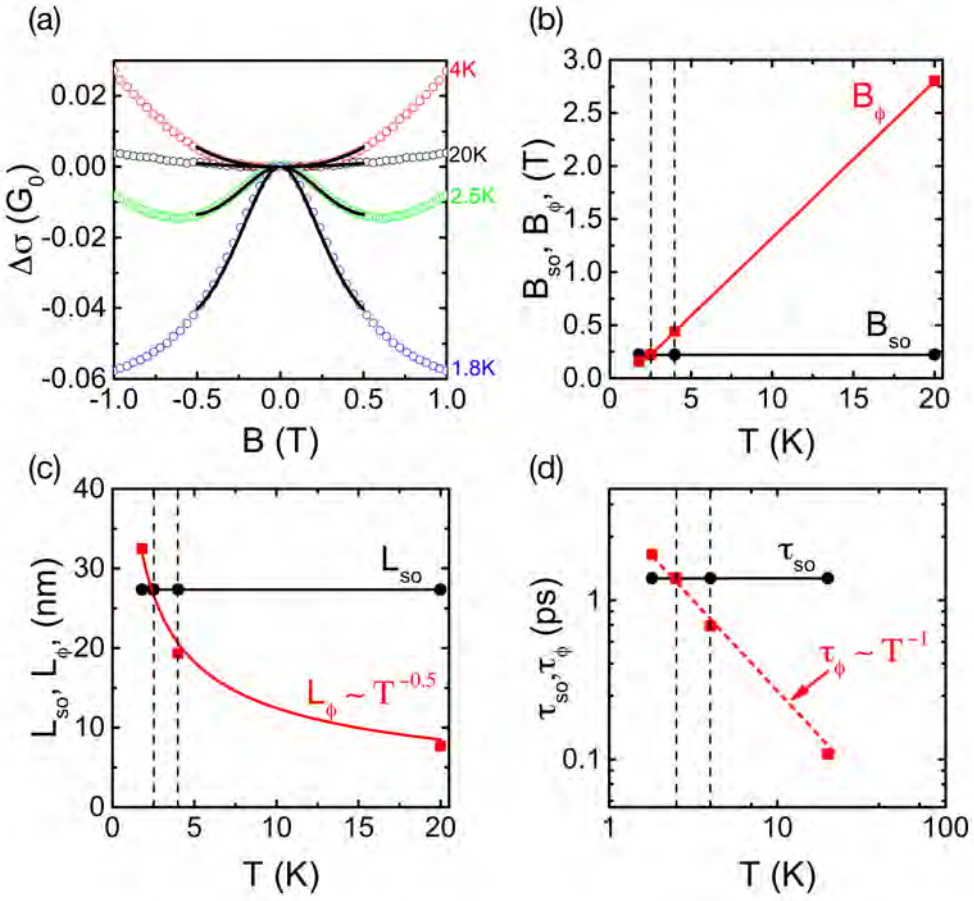

Figure. 2. (a) Reduced magnetoconductivity, $\Delta\sigma = \sigma(B) - \sigma(B = 0)$ (in units of $G_0 = e^2/\pi h$) at different temperatures for $B_{||}$= 0 T. The solid lines are fits to Rashba theory (Equation 1). (b) Extracted spin coherence fields B_{so} (circles) and phase coherence fields B_ϕ (squares) from the fits as a function of temperature. (c) Spin coherence length L_{so} (circles) and phase coherence length L_ϕ (squares) as a function of temperature. (d) Temperature dependence of spin (circles) and phase (squares) relaxation times plotted as a function of temperature. Vertical dashed lines indicate temperatures of 2.5K and 4K.

For all data presented from this point on in Figures 2-4 we have removed the HHI from the magnetoconductivity. Figure 2a shows the reduced magnetoconductivity $\Delta\sigma = \sigma(B) - \sigma(B = 0) = \rho_{xx}^{-1}(B) - \rho_{xx}^{-1}(0)$ plotted at different temperatures and in the absence of an in-plane field. The evolution of $\Delta\sigma$ as a function of temperature shows a transition from WL to WAL as the temperature is reduced. WAL is characteristic of 2D systems in the presence of spin-orbit coupling. In this case a strong spin-orbit interaction is believed to occur as a result of the Rashba mechanism [16, 17] due to the strong electric

field, $E = \frac{pe}{\varepsilon_0 \varepsilon_D} = 4.62 \times 10^6 e\text{V/cm}$ (where $\varepsilon_D = 5.70\ \text{F/m}$ is the permittivity of diamond), which accompanies the asymmetric 2D confinement potential at the diamond surface [10]. The solid curves in Figure 2a are fits to the theory (Equation 1) of Knap *et. al.* for weak anti-localization due to k^3 Rashba spin-orbit coupling (although the Rashba interaction is cubic in k for heavy holes in GaAs quantum wells, we note that the fitting parameters are rather insensitive to whether we use k or k^3 spin orbit interaction) [18, 19]:

$$\Delta\sigma = \frac{e^2}{2\pi^2\hbar}\left[\Psi\left(\frac{1}{2}+\frac{B_\phi+B_{so}}{B}\right)+\frac{1}{2}\Psi\left(\frac{1}{2}+\frac{B_\phi+2B_{so}}{B}\right)-\frac{1}{2}\Psi\left(\frac{1}{2}+\frac{B_\phi}{B}\right)-\ln\left(\frac{B_\phi+B_{so}}{B}\right)-\frac{1}{2}\ln\left(\frac{B_\phi+2B_{so}}{B}\right)+\frac{1}{2}\ln\left(\frac{B_\phi}{B}\right)\right], \quad (1)$$

Fitting parameters are the spin-orbit characteristic field, B_{so}, and the phase relaxation characteristic field, B_ϕ, as they are shown in Figure 2(b). The corresponding phase and spin coherent lengths, L_{SO} and L_ϕ, calculated using $L_\phi = (\hbar/(4eB_\phi))^{0.5}$ and $L_{SO} = (\hbar/(4eB_{SO}))^{0.5}$, are illustrated in Figure 2(c). B_{so} and L_{so} are found to be independent of temperature as expected. In contrast, B_ϕ depends linearly on temperature yielding an L_ϕ that varies with temperature according to $T^{-0.55\pm0.05}$, evidence that the holes are indeed 2D in character [20].

The spin and phase relaxation times, $\tau_{so} = \hbar/(4eDB_{so})$ and $\tau_\phi = \hbar/(4eDB_\phi)$ were also determined, as shown in Figure 2(d), where the diffusion coefficient, $D = \frac{l^2}{2\tau_{tr}} = 0.54 \times 10^{-3}\text{m}^2\text{s}^{-1}$ depends through l on the hole density p, and the transport relaxation time $\tau_{tr} = \frac{\sigma_D m_{hh}}{pe^2} = 7.1$ fs. We adopted the value of $m_{hh} = 0.208m_0$ for the effective heavy hole mass which is assumed to be isotropic for wave-vectors k in the (100) plane of the 2D hole gas [10, 11]. The spin relaxation time τ_{so} is temperature independent, while τ_ϕ scales approximately with T^{-1} consistent with scattering in the form of the Nyquist dephasing scattering mechanism as expected in a weakly disordered 2D system [15, 20].

From the relaxation times derived above we calculate the corresponding spin orbit interaction strength, $\Delta_{so} = \frac{\hbar}{(2\tau_{tr}\tau_{so})^{0.5}} = 4.71$ meV, which is assumed to vary as k^3 in wavenumber for a 2D hole band with a Rashba coefficient $\beta = \frac{\Delta_{so}}{(2k_F^6)^{0.5}} = 2.7$ eVÅ^3, where $k_F = (2\pi p)^{1/2}$ is the Fermi wave vector. These values of Δ_{so} and β are consistent

with our previous experiments using similar devices (Δ_{so}= 4.61 meV, β = 4.01 eVÅ^3) taking differences in hole concentration into account [10].

Having established the magnetoresistance in response to an applied perpendicular magnetic field, we now consider the response when a constant in-plane field is additionally applied. Figure 3 shows the evolution of the magnetoconductance curves for different values of the constant in-plane field $B_{\|}$. At a temperature of 4K where phase coherent backscattering dominates to give weak localization on account of the fact that the phase relaxation time is shorter than the spin-orbit scattering time (c.f. Fig. 2), the magnetoconductance curves are largely unaffected by the application of the in-plane magnetic field. In contrast, the magnetoconductance curves recorded at 2.5K, which are dominated by the signature of WAL for $B_{\|} = 0$ ($\tau_{so} < \tau_{\phi}$), show a dramatic dependence on the in-plane field with the WAL suppressed as $B_{\|}$ increases (Figure 3b).

The Zeeman interaction is known to destroy weak anti-localization, while microroughness present in the 2D quantum well can cause additional dephasing in the presence of an in-plane magnetic field. Both effects result in a suppression of weak anti-localization [12]. In principle, the Zeeman effect causes coupling of the singlet and triplet states in the presence of an applied in-plane magnetic field. However, as long as the condition $g\mu_B B_{\|} < \hbar/\tau_{so}$ is met, where g is the in-plane hole g factor, and μ_B the Bohr magneton, which we later show to be the case, the Zeeman interaction manifests itself in only the singlet state.

Following the approach of Minkov *et. al*.[12], we consider the relative contribution of each of these mechanisms by fitting the data to the weak anti-localization theory with the corresponding corrections applied to the singlet (dependent on B_{ϕ} only) and triplet (dependent on B_{ϕ} and B_{so}) terms.
Equation 1 now has two additional terms; Δ_S and Δ_r:

$$\Delta\sigma = \frac{e^2}{2\pi^2\hbar}\left[\Psi\left(\frac{1}{2}+\frac{B_{\phi}+B_{so}+\Delta_r}{B}\right)+\frac{1}{2}\Psi\left(\frac{1}{2}+\frac{B_{\phi}+2B_{so}+\Delta_r}{B}\right)-\frac{1}{2}\Psi\left(\frac{1}{2}+\frac{B_{\phi}+\Delta_S+\Delta_r}{B}\right)-\ln\left(\frac{B_{\phi}+B_{so}+\Delta_r}{B}\right)-\frac{1}{2}\ln\left(\frac{B_{\phi}+2B_{so}+\Delta_r}{B}\right)+\frac{1}{2}\ln\left(\frac{B_{\phi}+\Delta_S+\Delta_r}{B}\right)\right], \quad (2)$$

which has been fitted to the data in Figure 3(a).

Here $\Delta_S = \frac{\tau_{so}}{4e\hbar D}(g\mu_B B_\parallel)^2$ is the correction due to the Zeeman interaction, and $\Delta_r = \frac{\sqrt{\pi}}{2}\frac{e}{\hbar}\frac{d^2 L}{l}B_\parallel^2$, is the correction due to surface roughness, where d is the root-mean-square fluctuation of the quantum well width, L is the correlation length of the fluctuations, and l is the mean free path [12, 21, 22]. Note, that in the fits to equation 2 the only fitting parameters are Δ_S and Δ_r, since the values of B_ϕ and B_{so} are fixed from the fitting at $B_\parallel$=0 shown in Figure 2.

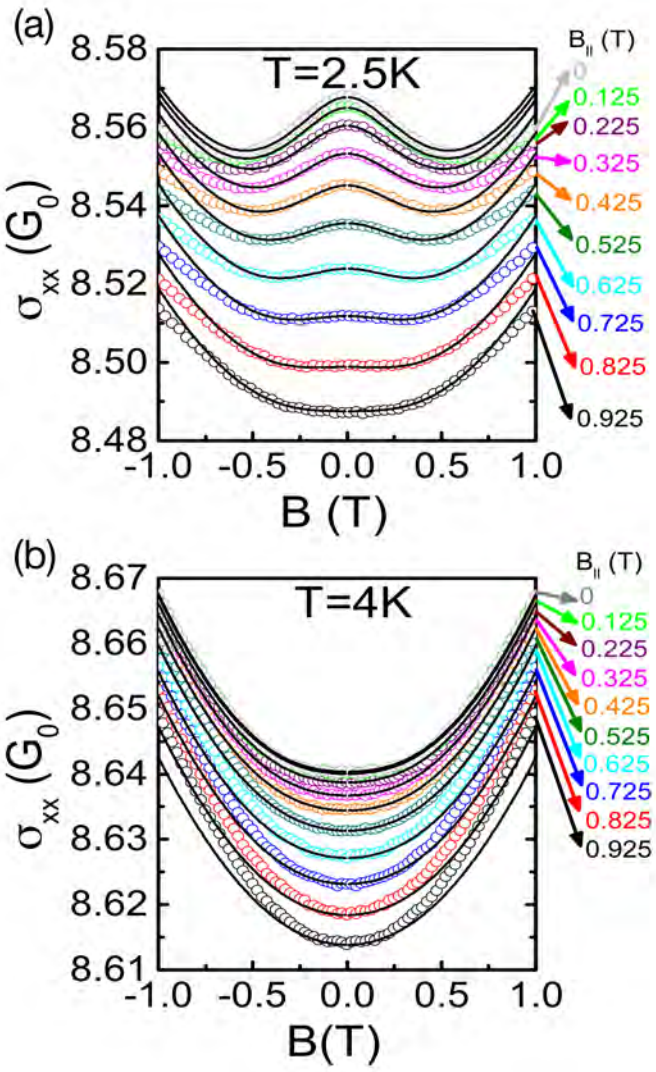

Figure. 3. Conductivity as a function of B with different applied in-plane magnetic fields (a) 2.5K and (b) 4K. The solid lines are fits to Equation 2 using as fitting parameters Δ_S and Δ_r as shown in Fig. 4b.

We first consider the limit in which surface roughness scattering is negligible. Fits to the magnetoconductance curves shown in Figure 3(a) using Equation 2 with $\Delta_r = 0$ and Δ_S as a fitting parameter yield the values shown by the lower curve in Figure 4(a). The derived values of Δ_S do not follow the expected quadratic dependence on $B_\parallel$, suggesting

that Zeeman splitting alone cannot account for the observed destruction of WAL. We also consider the limit in which microroughness is dominant. Imperfections at the near surface region may give rise to local fluctuations in confining potential causing charge carriers to shift in the direction perpendicular to the surface as they are transported through the device. In the presence of $B_{\|}$, transversely moving carriers effectively experience an additional random perpendicular field causing dephasing which introduces a correction Δ_r to B_ϕ in both the singlet and triplet terms of Equation 2. In this limit fits to the magnetoconductance curves of Figure 3(a) of identical quality yield values of Δ_r shown by the upper curve in Figure 4(a), which again do not follow the expected quadratic dependence on $B_{\|}$. Hence, from the fits alone it is not possible to extract definite and uncorrelated values for either Δ_r nor Δ_S. However, if we include both Zeeman and surface roughness effects in Equation two with the additional condition that they scale as $B_{\|}^2$, a unique set of values for Δ_S and Δ_r are obtained as illustrated in Figure 4(b). The fits are again indistinguishable from the two previous fits and are shown in Fig. 3(a) as the solid lines. While the fits are not perfect they faithfully reproduce the quenching of WAL due to $B_{\|}$. Deviation for high $B_\perp$are similar to those observed by Minkov et al.[12]. This confirms that the suppression of the WAL arises from both Zeeman splitting and dephasing related to imperfections in the hole confinement, with the latter playing the more dominant role in this system.

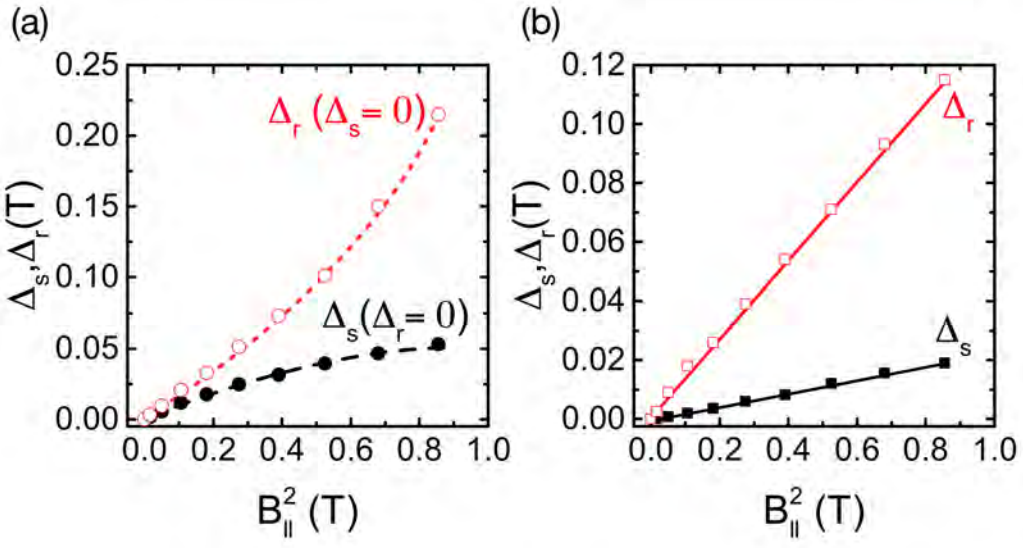

Figure. 4. Parameters Δ_S and Δ_r extracted from fitting equation 2 to the data of Fig 3a. (a) the symbols refer to cases where only Zeeman splitting (Δ_r= 0, full circles) and where only roughness (Δ_S=0, open circles) are considered. (b) Parameters Δ_S and Δ_r that correspond to the fits shown as solid lines in Fig.3.; both are linear in $B_{\|}^2$

The measured values of Δ_S and Δ_r allow us to calculate the in-plane hole g-factor and level of microroughness in the 2D hole accumulation layer. From the slope of Δ_S in Figure 4(b) we obtain for the absolute in-plane hole g-factor, $|g_{||}| = 2.6 \pm 0.1$. There are no other measurements of the g-factor for the 2D heavy hole subband of diamond available to compare our result with. We note that the condition $g\mu_B B_{\|} < \hbar/\tau_{so}$ is indeed satisfied for this value of g over the range of $B_{\|}$ fields applied here.

From the slope of Δ_r in Figure 4(b) the microroughness parameter d^2L is determined to be 280 ± 10 nm^3. The surface roughness was evaluated by imaging the surface with an atomic force microscope; a typical topographic image is shown in Figure 1(c). Images show that the hydrogenated surface is largely smooth with surface imperfections such as etch pits present with low density, typical of (100) diamond surfaces processed in a hydrogen plasma. From a large number of topographic scans the average rms surface roughness on the scale of the phase coherence length of 33 nm is determined to be 1.1 ± 0.3 nm, requiring the correlation length of the fluctuations L to be about 70 nm give the 230 nm^3 for d^2L. This value of L exceeds both the phase coherence length and the mean free path and would thus be irrelevant for the quantum interference effects probed here. Similarly, we may discount as the origin of the microroughness sub-surface damage which may remain from mechanical polishing of the diamond substrate and exists over longer length scales. One possible scenario to remedy the situation is to realize that the well width of the hole accumulation layer is self-consistently tied to the carrier concentration. Hence, local fluctuations in surface acceptor concentration (the OH^- ions) would contribute to the width fluctuations of the quantum well while going unnoticed in the AFM measurements. Therefore, restricting the correlation length to be smaller than the phase coherence length of 33nm requires d^2 to be at least 8.5 nm^2 , so that d is about 3 nm, with the additional 2.7 nm rms width fluctuations originating in lateral variations in carrier density provided the two roughnesses are uncorrelated and add geometrically. A fluctuation in well width of 3 nm, relative to an average width of about 1 nm [23], could arise from a lateral variation of an order of magnitude in carrier density. The recent observation of Shubnikov-de-Haas oscillations in this system requires the carrier density and mobility to be spatially inhomogeneous at this level [24]. The value of Hall mobility measured here is consistent with other work that shows the mobility to be dominated by Coulomb scattering from charged acceptors in the nearby water layer [13].

In summary, we have performed magnetotransport measurements of 2D holes in surface conducting diamond as a function of temperature and in-plane magnetic field. Suppression of the weak anti-localization with a magnetic field parallel to the 2D layer at 2.5 K was found to arise from a combination of dephasing contributions from Zeeman splitting and microroughness. From the microroughness we deduce the effective rms fluctuations in well width to be of the order of 3 nm. The effect of the Zeeman splitting yields a value for the gyromagnetic ratio of the carriers in the 2D hole layer of $|g_{||}| = 2.6 \pm 0.1$.

Corresponding Authors

*Email: g.akhgar@latrobe.edu.au; §Email: c.pakes@latrobe.edu.au

Acknowledgments

This work was supported by the Australian Research Council under the Discovery Project (DP150101673). We thank Leonid Golub for many invaluable discussions.

References

1. Awschalom, D.D. and M.E. Flatté, *Challenges for semiconductor spintronics.* Nature Physics, 2007. **3**(3): p. 153-159.
2. Datta, S. and B. Das, *Electronic analog of the electro-optic modulator.* Applied Physics Letters, 1990. **56**(7): p. 665-667.
3. Wolf, S., et al., *Spintronics: a spin-based electronics vision for the future.* Science, 2001. **294**(5546): p. 1488-1495.
4. Winkler, R., et al., *Spin-Orbit Coupling in Two-Dimensional Electron and Hole Systems*. Vol. 41. 2003: Springer.
5. Kim, K.-H., et al., *Gate-Controlled Spin-Orbit Interaction in InAs High-Electron Mobility Transistor Layers Epitaxially Transferred onto Si Substrates.* ACS nano, 2013. **7**(10): p. 9106-9114.
6. Koo, H.C., et al., *Control of spin precession in a spin-injected field effect transistor.* Science, 2009. **325**(5947): p. 1515-1518.
7. Liang, D. and X.P. Gao, *Strong tuning of Rashba spin–orbit interaction in single InAs nanowires.* Nano letters, 2012. **12**(6): p. 3263-3267.
8. Nitta, J., et al., *Gate Control of Spin-Orbit Interaction in an Inverted I n 0.53 G a 0.47 As/I n 0.52 A l 0.48 As Heterostructure.* Physical Review Letters, 1997. **78**(7): p. 1335.
9. Maier, F., et al., *Origin of surface conductivity in diamond.* Physical review letters, 2000. **85**(16): p. 3472.
10. Akhgar, G., et al., *Strong and Tunable Spin–Orbit Coupling in a Two-Dimensional Hole Gas in Ionic-Liquid Gated Diamond Devices.* Nano letters, 2016. **16**(6): p. 3768-3773.
11. Edmonds, M.T., et al., *Spin–Orbit Interaction in a Two-Dimensional Hole Gas at the Surface of Hydrogenated Diamond.* Nano letters, 2014. **15**(1): p. 16-20.
12. Minkov, G., et al., *Weak antilocalization in quantum wells in tilted magnetic fields.* Physical Review B, 2004. **70**(15): p. 155323.
13. Verona, C., et al., *Comparative investigation of surface transfer doping of hydrogen terminated diamond by high electron affinity insulators.* Journal of Applied Physics, 2016. **120**(2): p. 025104.
14. Edmonds, M., et al., *Surface transfer doping of hydrogen-terminated diamond by C60F48: Energy level scheme and doping efficiency.* The Journal of chemical physics, 2012. **136**(12): p. 124701.
15. Goh, K., M. Simmons, and A. Hamilton, *Electron-electron interactions in highly disordered two-dimensional systems.* Physical Review B, 2008. **77**(23): p. 235410.
16. Winkler, R., et al., *Anomalous Rashba spin splitting in two-dimensional hole systems.* Physical Review B, 2002. **65**(15): p. 155303.
17. Habib, B., et al., *Negative differential Rashba effect in two-dimensional hole systems.* Applied physics letters, 2004. **85**: p. 3151.
18. Bergmann, G., *Weak localization in thin films: a time-of-flight experiment with conduction electrons.* Physics Reports, 1984. **107**(1): p. 1-58.
19. Knap, W., et al., *Weak antilocalization and spin precession in quantum wells.* Physical Review B, 1996. **53**(7): p. 3912.
20. Altshuler, B.L., A. Aronov, and D. Khmelnitsky, *Effects of electron-electron collisions with small energy transfers on quantum localisation.* Journal of Physics C: Solid State Physics, 1982. **15**(36): p. 7367.
21. Mal'shukov, A., V. Shlyapin, and K. Chao, *Effect of the spin-orbit geometric phase on the spectrum of Aharonov-Bohm oscillations in a semiconductor mesoscopic ring.* Physical Review B, 1999. **60**(4): p. R2161.

22. Meyer, J.S., A. Altland, and B.L. Altshuler, *Quantum transport in parallel magnetic fields: A realization of the Berry-Robnik symmetry phenomenon.* Physical review letters, 2002. **89**(20): p. 206601.
23. Edmonds, M., C. Pakes, and L. Ley, *Self-consistent solution of the Schrödinger-Poisson equations for hydrogen-terminated diamond.* Physical Review B, 2010. **81**(8): p. 085314.
24. Takahide, Y., et al., *Quantum oscillations of the two-dimensional hole gas at atomically flat diamond surfaces.* Physical Review B, 2014. **89**(23): p. 235304.

5

G-factor and Well Width Fluctuations as a Function of Carrier Density in the 2D Hole Accumulation Layer of Transfer Doped Diamond

5.1 Introduction

Building on the results of Chapter 4, in this Chapter we presented the first systematic investigation of the change in g-factor and well width fluctuation in the hole accumulation layer as a function of carrier density. This is done by modulating the charge carrier density using an ionic liquid gate, and performing magnetotransport measurements in the presence of an in-plane magnetic field. As in the case of Chapter 4, a constant in-plane magnetic field is applied, while sweeping the perpendicular magnetic field, in order to quench the weak anti-localization. This allowed us to determine the in-plane g-factor and quantify well width fluctuations as function of density.

The results obtained here showing that magnitude in-plane g-factor increases monotonically from 1.3 to 2.3 while the fluctuation in quantum well microroughness drops by factor of three for the carrier densities in the range 2.27-4.35 $\times$ 10^{13} cm^{-2}; possible explanations for these observations are discussed.

This chapter is presented as a paper which has been submitted to *Physical Review B* (2018), *"G-factor and well width fluctuation of carrier density in the 2D hole accumulation layer of transfer doped diamond", written by G. Akhgar, L. Ley, D. L. Creedon, A. Stacey, J. C. McCallum, A. R. Hamilton, and C. I. Pakes.*

Author Contribution:

Akhgar led all stages of this work, from experimental planning, to device fabrication and measurement, analysis and modelling of the results and preparation of the manuscript. Stacey prepared the hydrogen-terminated diamond surface. Creedon assisted with the operation of the cryogenic refrigerator and the collection of data. Pakes, Hamilton, McCallum and Ley assisted with the analysis of the results and preparation of the manuscript.

5.2 Journal Article (Physical Review B (Submitted October 2018)).

G-Factor and Well-Width Fluctuations as a Function of Carrier Density in the 2D Hole Accumulation Layer of Transfer Doped Diamond

Golrokh Akhgar,*[1] Lothar Ley,[1,2], Daniel L. Creedon,[3] Alastair Stacey,[3] Jeffrey C. McCallum,[3] Alex R. Hamilton[4] and Christopher I. Pakes§[1]

[1] Department of Chemistry and Physics, La Trobe University, Victoria 3086, Australia

[2] Institute of Condensed Matter Physics, Universität Erlangen, Staudt-Str. 1, 91058 Erlangen, Germany

[3] School of Physics, The University of Melbourne, Victoria 3010, Australia

[4] School of Physics, University of New South Wales, Sydney, New South Wales 2052, Australia

Abstract

The two-dimensional (2D) hole gas at the surface of transfer doped diamond shows quantum mechanical interference effects in magnetoresistance in the form of weak localization (WL) and weak anti-localization (WAL) at temperatures below about 5 K. Here we use the quenching of the WAL by an additional magnetic field applied parallel to the 2D plane to extract the magnitude of the in-plane g-factor of the holes and fluctuations in the well width as a function of carrier density. Carrier densities are varied between 1.71 and 4.35 x 10^{13} cm^{-2} by gating a Hall bar device with an ionic liquid. Over this range, calculated values of $|g|$ vary between 1.6 and 2.3 and the extracted well width variation drops from 3 to 1.3 nm rms over the phase coherence length of 33 nm for a fixed geometrical surface roughness of about 1 nm as measured by atomic force microscopy. Possible mechanisms for the extracted variations in the presence of the ionic liquid are discussed.

I. Introduction

Undoped diamond is a bona fide insulator. However, when the surface is terminated with hydrogen and exposed to air it develops a pronounced *p*-type surface conductivity through a process that is termed transfer doping [1]. Transfer doping involves an electrochemical reaction between diamond and the ever-present water layer that leaves holes in the diamond valence bands and compensating OH^- ions at the surface [2]. As space charges, the holes are confined by a strong upward band bending to a narrow two dimensional (2D) well right below the surface. Typical carrier concentrations are 10^{12} to 10^{13} cm^{-2} and the width of the well depends self consistently on carrier density and lies in the range of 1 to 10 nm [3]. Because transfer doping does not involve the activation of an acceptor there is no carrier freeze-out and metallic conductivity is maintained down to at least 250 mK. Low temperature magnetoresistance measurements show that electrical transport in the hole accumulation layer exhibits quantum phenomena that are characteristic for a 2D quantum system and lead to a deviation from classical Drude conductivity. They are Shubnikov-de-Haas oscillations [4], a strong hole-hole interaction (HHI), quantum interference effects that show up as weak localization (WL) [5], and weak anti-localization (WAL) due to strong spin-orbit interaction [5]. Using an ionic liquid (IL) as a gate dielectric we were able to increase the carrier density from 1.1 to 7.23 x 10^{13} cm^{-2} with a proportional increase in spin-orbit splitting from 4.6 to 24.5 meV [6]. This is the largest spin-orbit splitting observed to date for a 2D hole system and by far exceeds the atomic spin-orbit splitting of the valence electrons in diamond ($\Delta_{atomic} = 8\, meV$) [7]. Because the electric field in the highly asymmetrical confining potential increases with carrier density the enhanced spin-orbit splitting was ascribed to the Rashba effect. In particular, here it is ascribed to the Rashba effect cubic in wave vector *k* for reasons explained in ref. [8].

With a strong spin-orbit interaction the holes in diamond are potential candidates for spin manipulation. While the Rashba effect provides the coupling of the carrier spin to an electric field, the strength of the coupling to a magnetic field, i.e. the carrier g-factor, was still missing. That gap was recently closed by us following Minkov *et al*. [9] and measuring the low temperature magnetoresistance as a function of a magnetic field perpendicular to the 2D hole gas with an additional parallel field as a parameter [10]. The analysis of the data yields for the magnitude of the g-factor a value of 2.6± 0.1. In

addition, the data showed additional effects due to variations in effective well width of 3 nm mean square roughness over a distance of about 30 nm [10].

Here we extend these measurements to hole concentrations that are tuned by an ionic liquid gate over the range from 1.71 to 4.35 x 10^{13} cm^{-2}. The analysis gives a monotonically rising g-factor while the effective well width variation decreases with increasing carrier concentration. Mechanisms are discussed to rationalize these observations.

II. Experiment

A commercial IIa single crystal (001) diamond face was used to fabricate the Hall bar device. The surface was hydrogen terminated at approximately 850 °C in a microwave hydrogen plasma with a power of 1500 W for 10 minutes. In order to achieve saturation charge transfer doping, the sample was left in air for several days following the termination. A Hall bar with channel length and width of 200 μm and 40 μm, respectively, and palladium contacts was fabricated using standard photolithography and lift-off processing. The conducting regions are isolated from the rest of the surface by oxygen plasma exposure. The Hall bar device was gated using the ionic liquid 1-ethyl-3-methyl-imidazolium tris(pentafluoroethyl) trifluorophosphate $[C_2C_1Im]^+[FAP]^-$ as a high capacity gate insulator. The IL is dropped on the channel of the device using a micropipette, ensuring coverage on the gate contact as well (Figure 1a). The gate bias is applied above the IL melting point of 236 K in order to ensure the full IL polarisation. After cooling below the melting point the polarisation is maintained and potentials on any of the contacts have no influence on the effective gate voltage. Magnetotransport measurements are performed using a Leiden Cryogenics dry dilution refrigerator with an integrated 9-1-1 T superconducting vector magnet. Longitudinal and Hall resistivity are measured at temperatures from 1.5 K to 20 K for perpendicular magnetic fields, $B_\perp$ up to 1T and gate biases between 0 and -3.0 V. Zeeman splitting and micro-roughness for each gate voltage are derived from magnetoresistance measurements at 2.5 K when in addition to $B_\perp$ a constant in plane field $B_\parallel$ between 0 to 1 T is applied in steps of 0.2 T.

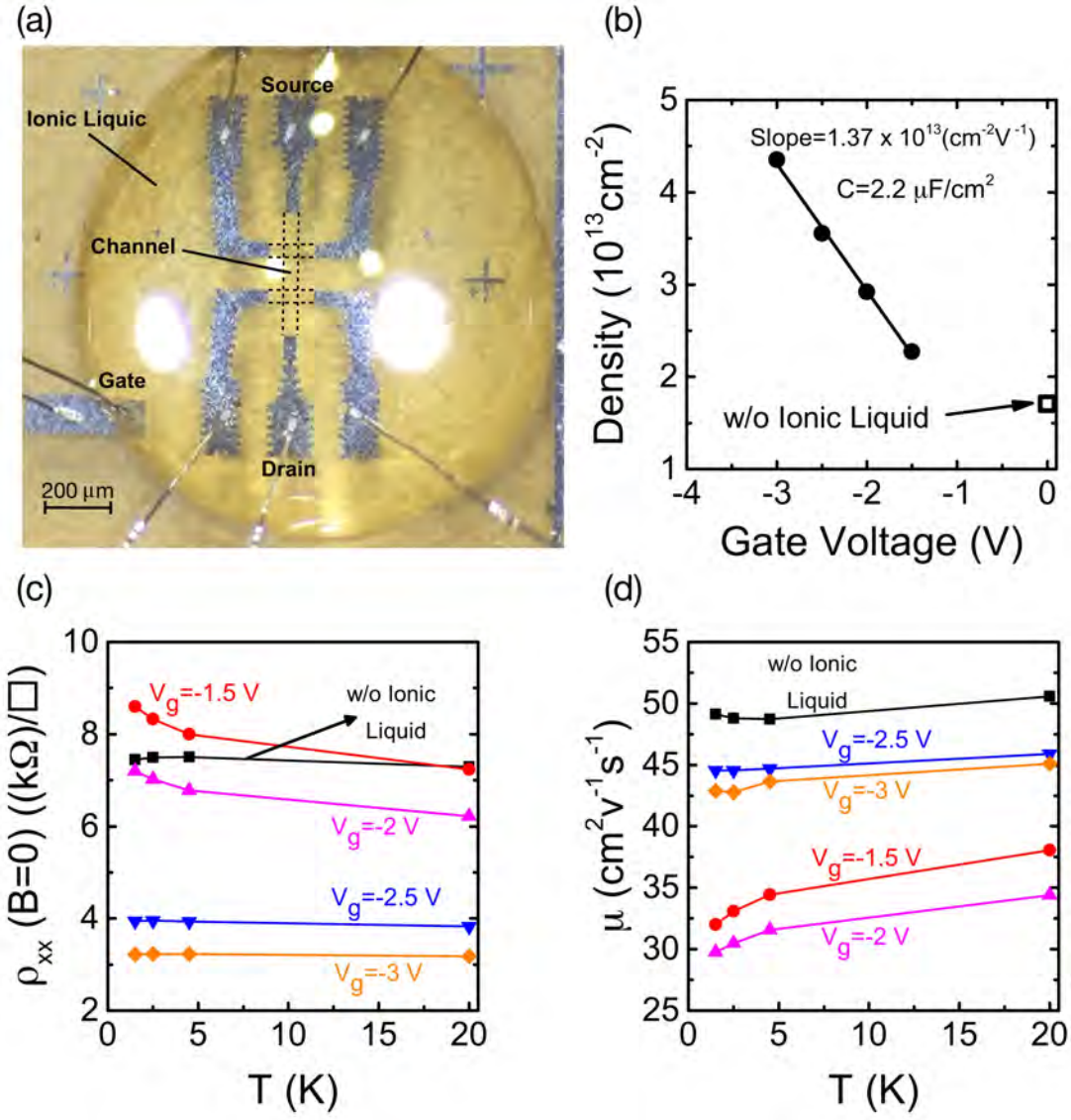

Figure 1: (a) Optical image of the ionic liquid gated hall bar device. The two bright spots are reflections of the overhead light on the surface of the ionic liquid. (b) Hole sheet density as a function of gate voltage. (c) and (d) Hole sheet resistivity and mobility, respectively, as a function of temperature with gate voltage as parameter.

III. Results

The analysis of the data follows the one used in our previous publications [5, 6, 10]. As a first step, hole-hole interaction (HHI) is removed from ρ_{xx} and ρ_{xy} by applying a correction to the measured data according to Goh et al. [11] and the procedure is explained in the supporting information (SI). From this corrected data the longitudinal conductivity σ_{xx}, carrier concentration, and mobility, all as a function of gate voltage, are derived in the usual way. The sample exhibits metallic conductivity down to the lowest temperatures except for gate voltages of -1.5 and -2.0 V where a slight increase in longitudinal sheet

resistivity is observed (Figure. 1c). For these two gate voltages the mobilities are noticeably lower than for the remainder of the gate voltages (Figure.1d) where mobilities are within the range reported consistently for air induced surface conductivity [12, 13]. Since mobility and longitudinal resistivity are back to normal at -3.0 V gate voltage there is no apparent deterioration in sample properties with increasing gate voltage and no peculiar behaviour in magnetoresistance has been detected either. As intended, the carrier concentration increases linearly with gate voltage albeit with a slightly smaller slope compared to our earlier work as reflected in the ionic liquid capacitance of 2.2 F/cm^2 vs the previous 2.8 F/cm^2 [6]. Other salient quantities such as diffusion constant, elastic scattering times, and mean free path are collected in the supplementary information.

We turn now to the magnetoconductance data without application of a field component parallel to the 2D plane (see the σ_{xx} vs B curves for $B_{\parallel} = 0$ in Figure. 2). For the lowest carrier density without ionic liquid (w/o IL) the magnetoconductivity exhibits the drop in σ_{xx} around $B_{\perp} = 0$ characteristic of weak localization that is modified by the central, cusp-like peak due to weak anti-localization. The WAL feature increases with gate voltage and thus carrier concentration until it is the dominant feature of the magnetoconductivity starting at Vg = -2.0 V.

WAL is due to spin-orbit interaction which destroys the constructive interference necessary for WL. Spin-orbit interaction can ultimately even lead to a conductivity that exceeds the Drude conductivity due to the destructive interference of time reversed backscattering loops [14]. WL is partly restored by coupling the spins to the external magnetic field which accounts for the cusp-like appearance of WAL in the spectra. The magnetoconductance curves are fitted to the expression derived by Hikami *et al*. [15] as given by Knap *et al*. [16] for k^3 Rashba spin-orbit interaction. From the fits crucial parameters such as the phase and spin coherence lengths of the carriers and their spin-orbit splitting Δ_{so} are derived. These quantities are collected in the supplementary information and Δ_{so} exhibits a linear increase with carrier density reported previously [6]. The increase is characteristic for spin-orbit interaction due to the Rashba effect because there is a direct connection between carrier density and electric field strength in the carrier confining quantum well on account of Gauss's law: higher carrier densities result in more asymmetric quantum wells.

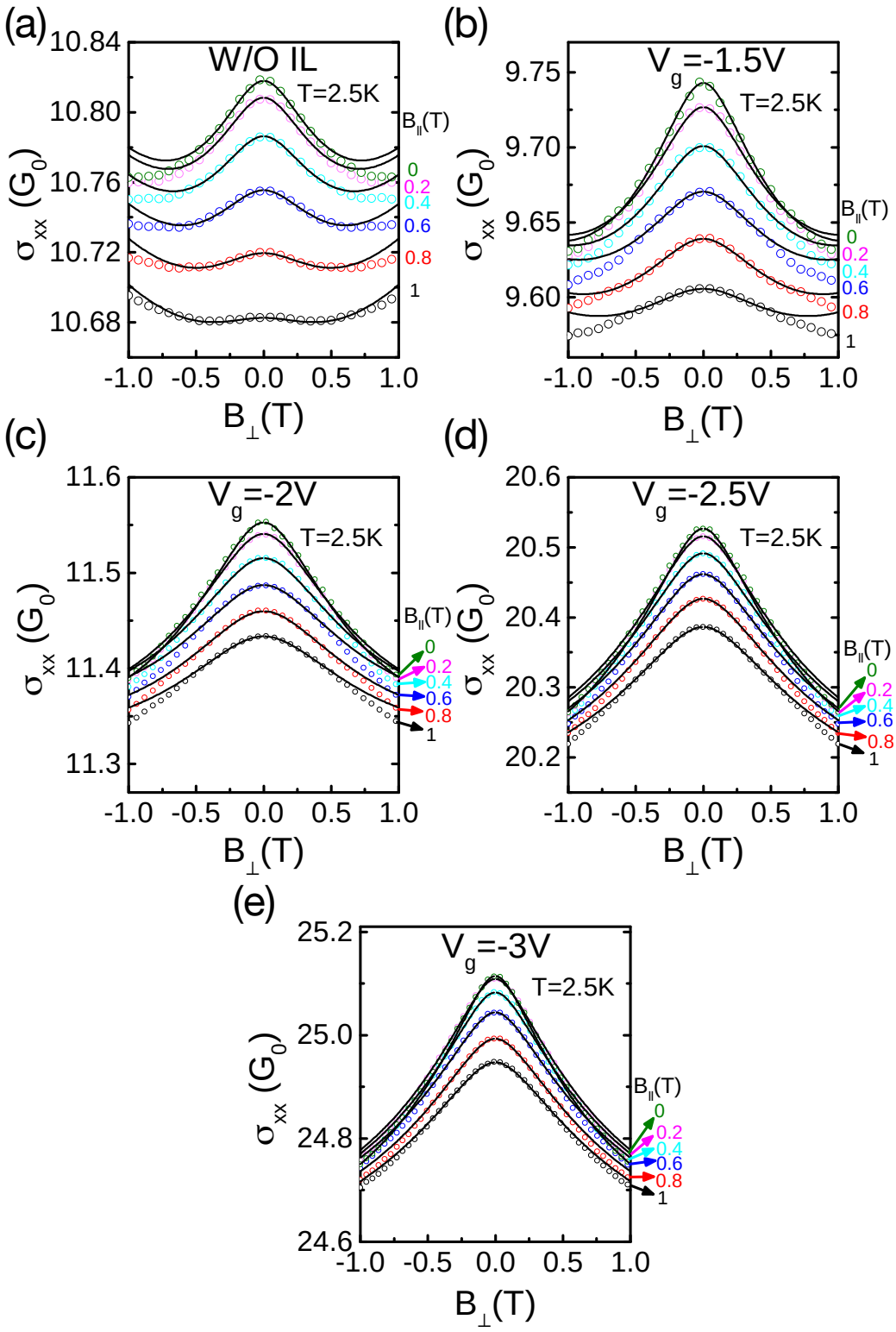

Figure 2: Longitudinal conductivity σ_{xx} as a function of $B_{\perp}$with different applied in-plane fields $B_{\parallel}$; (a) when the device is ungated, without ionic liquid; (b) to (e) with gate biases of -1.5 V, -2 V, -2.5 V, and -3 V, respectively. The open circles are the data points and the lines are the fits.

Turning to the traces with parallel field component we observe a quenching of the WAL feature with increasing $B_{\parallel}$. This is most apparent for the lowest carrier densities where

WAL is still rather weak in the absence of $B_{\|}$. Two factors contribute to this reduction, fluctuations in effective well width and the Zeeman effect [17, 18]. They are accounted for in the Hikami formula for the change in conductance $\Delta\sigma$ by two additional parameters Δ_r and Δ_s [9]:

$$\Delta\sigma = \frac{e^2}{2\pi^2\hbar}\left[\Psi\left(\frac{1}{2}+\frac{B_\phi+B_{so}+\Delta_r}{B_\perp}\right)+\frac{1}{2}\Psi\left(\frac{1}{2}+\frac{B_\phi+2B_{so}+\Delta_r}{B_\perp}\right)-\frac{1}{2}\Psi\left(\frac{1}{2}+\frac{B_\phi+\Delta_S+\Delta_r}{B_\perp}\right)-\ln\left(\frac{B_\phi+B_{so}+\Delta_r}{B_\perp}\right)-\frac{1}{2}\ln\left(\frac{B_\phi+2B_{so}+\Delta_r}{B_\perp}\right)+\frac{1}{2}\ln\left(\frac{B_\phi+\Delta_S+\Delta_r}{B_\perp}\right)\right], \quad (1)$$

Here, Ψ is the digamma function and B_ϕ and B_{so} are characteristic fields that scale with the phase breaking inelastic scattering rate $1/\tau_\phi$ and the spin relaxation rate $1/\tau_{so}$ due to spin-orbit interaction according to $1/\tau_\phi = 4eDB_\phi/\hbar$ and $1/\tau_{so} = 4eDB_{so}/\hbar$ where D is the diffusion constant.

Fluctuations in the well width means carriers that are backscattered and interfere after traversing time reversed loops are no longer confined strictly to a plane and will therefore be susceptible to a magnetic field parallel to the 2D plane. This allows an additional Aharonov-Bohm phase to be involved. Hence $\Delta_r = \frac{\sqrt{\pi}}{2}\frac{e}{\hbar}\frac{d^2L}{l}B_{\|}^2$ is added to B_ϕ in the above formula as an additional phase-breaking effective field that scales with $\frac{d^2L}{l}$, the product of the mean square well width fluctuations d^2 and the correlation length of the fluctuations L divided by l, the elastic mean free path.

The term $\Delta_s = \frac{\tau_{so}}{4e\hbar D}(g\mu_B B_{\|})^2$ scales with the square of the in-plane Zeeman splitting $g\mu_B B_{\|}$ where g and μ_B are the g-factor of the carriers and the Bohr magneton, respectively. The correction Δ_s is applied only to the singlet term (dependent on B_ϕ only) and not the triplet term (dependent on B_ϕ and B_{so}) in eq. 1 [9].

All magnetoconductivity curves for $B_{\|} = 0$ were first fitted to eq. 1 with Δ_r, Δ_s set to zero. From these fits the characteristic fields B_ϕ and B_{so} are derived which in turn yield the inelastic and spin-orbit scattering times and the spin-orbit splitting as a function of gate voltage and hence carrier density. All these values are collected in the supplementary information and they are in agreement with earlier data derived from the magnetoconductivity of the hole gas in diamond in the absence of $B_{\|}$ [5, 6].

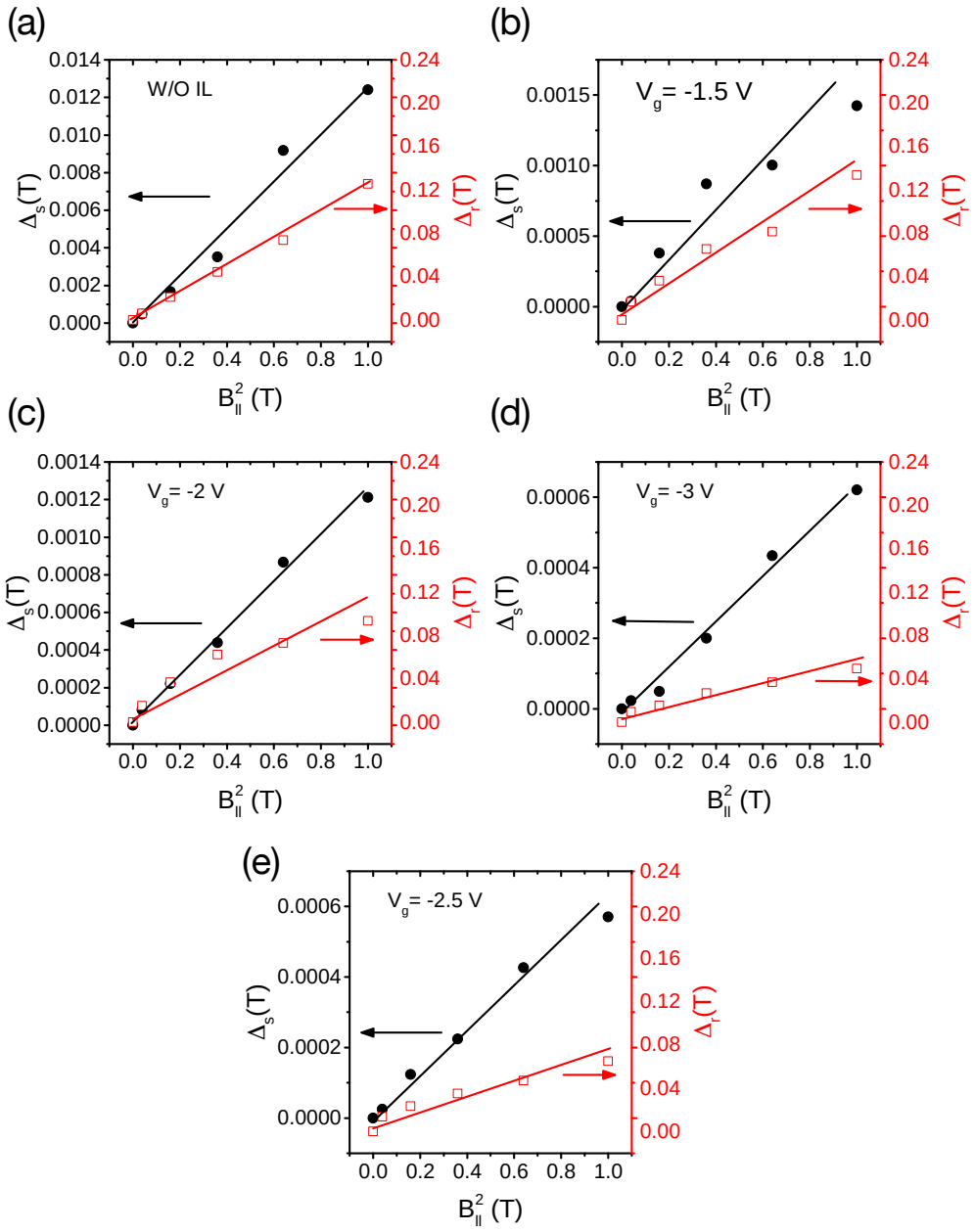

Figure 3: Parameters Δ_s and Δ_r as extracted from fits to the magnetoconductivity curves in Figure. 2 plotted vs $B_{\parallel}^2$ for the gate voltages indicated in each frame; W/O IL: without ionic liquid. The lines are linear regressions to the data points.

Next, Δ_r and Δ_s were varied in eq 1. to fit the curves for finite $B_{\parallel}$ while keeping $B_{\phi}$and B_{so} fixed at the value previously determined for each gate voltage in the absence of $B_{\parallel}$. Satisfactory fits were obtained as demonstrated by the solid lines in Figure. 2. for a selection of gate voltages. In Figure. 3, Δ_r and Δ_s so obtained are plotted vs $B_{\parallel}^2$. Both scale – the latter with some scatter – linearly with $B_{\parallel}^2$ as required for eq. 1 to be applicable. From the slopes of linear regressions, the factors d^2L and g are calculated according to the above expressions and they are plotted as a function of carrier density in Figure. 4.

The error bars were calculated using error progression from the standard deviations obtained in the fitting procedures or estimated as 5% for the diffusion constant D. D is directly traced to the Drude conductivity σ_D and this error therefore reflects the precision of the conductivity measurement. However, we ascribe a considerably larger systematic error of 20% to D that represents the uncertainty in identifying the conductivity at 30 K with the true Drude conductivity at the measurement temperature.

IV. Discussion

The use of magnetoresistance as a non-destructive method to characterize the roughness of 2D systems was pioneered by Wheeler and coworkers [19-21]. and it was taken up by Minkov *et al.* [22] and Cabanas *et al*. [23] with the theoretical underpinning provided by Mathur and Baranger [24]. In these works the attenuation of weak localization in the presence of an additional magnetic field parallel to the plane of the 2D system was taken as evidence for interface roughness in Si/SiO_2 interfaces of MOSFET structures [19-22] and of well width fluctuations in an AlGaAs heterostructure [19]. In all cases the interpretation follows the one given here, namely the addition of a $B_{\|}$ dependent phase breaking rate when the time reversed electron loops deviate from a strictly planar path and thus expose open loops to $B_{\|}$ as well. Interface roughness or well width variations are extracted analoguously to the procedure described above and qualitative [21] as well as quantitative [22] agreement between the interface roughness determined by magnetoresistance and atomic force microscopy has been reported. In one case, the interface roughness parameter was determined as a function of carrier density in the inversion channel of a gated MOSFET device [20]. Here, despite an unchanged topological roughness, the apparent magnetoresistance roughness increased about twofold for an increase in carrier density by a factor of three. The authors ascribe that to the fact that the electron wavefunction is brought closer to the interface as the confining potential narrows with increasing carrier density and hence becomes more susceptible to the interface roughness. This is the opposite of what we observe and we shall come back to it below.

The first to study the effect of interface roughness and Zeeman splitting on weak anti-localization in the presence of a parallel field component were Minkov *et al*. [9] and they derived g- factor and interface roughness for carriers in an InGaAs quantum well. Similar

work on the 2D electron gas induced by the intrinsic polarisation of GaN at the AlGaAs/GaN interface was performed by Cabanas *et al.* [23], for example. However, to our knowledge, this is the first instance where both interface roughness or well width variation and in-plane g-factor are systematically studied as a function of carrier density in a 2D hole gas.

We start with the result for the in-plane g-factor as given in Figure. 4a. We tacitly presuppose that we are always talking about the magnitude of the g- factor in what follows and ignore for the time being the 20% systematic uncertainty alluded to above. It is satisfying albeit to be expected that the g-factor without IL agrees with that derived previously for an ungated device of otherwise identical properties [10]. Once the IL is in place the calculated in-plane g-factor increases monotonically from 1.3 to 2.3 as the carrier density is doubled from 2.2 to 4.4 x10^{13} cm^{-2} thus bracketing the free-electron value of g = 2. Similar values were previously derived by the same method for electrons in the InGaAs quantum well (1.7 ± 0.3) [9], and 1.95 in an AlGaAs/GaN interface layer [23]. In lieu of any relevant measurements or calculations of the g-factor for the valence bands of diamond we can only speculate about the origin of the variation in g-factor. Since any deviation from g =2 has to be a band structure effect, two closely related factors come to mind: band filling and hybridisation. As shown previously [3], the carriers in the hole accumulation layer of diamond occupy the lowest 2D band based on the first quantum state derived from the heavy hole valence band in bulk diamond. The next higher, empty band is that based on the lowest quantum state derived from the light hole valence band. These two bands eventually cross for sufficiently large *k*-vectors because the "light hole band" has an effective mass that is larger than the 2D mass of the "heavy hole band" for in-plane dispersion. Hence, any filling of the "heavy hole band" moves the Fermi wavevector k_F closer to the crossing point and thus increases the hybridisation of the states that matter for transport. A change in hybridisation of the two bands as a consequence of varying carrier densities could give rise to changes in g-factor. However, there is a caveat. As the carrier density increases, the width of the confining potential decreases which in turn affects the quantisation energies of the "heavy" and "light hole" bands, i.e. their energy at k=0. That could, in principle, overcompensate the band filling effect and move the energies of the two bands at k_F apart.

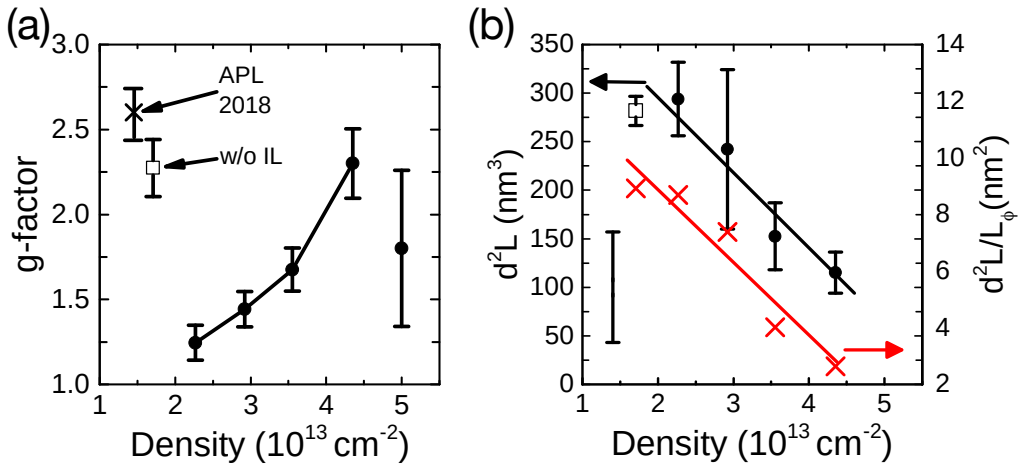

Figure 4. (a) In-plane g-factor and (b) micro-roughness parameters d^2L as calculated from the slopes of the lines in Figure 3 vs hole density. The error bars on each data point are the statistical errors. An overall 20% systematic error due to the uncertainty in the diffusion constant (see text) is indicated by the isolated error bar. The solid lines are guides to the eye and APL 2018 refers to the g-factor of ref. [10].

Using a simple band calculation, based upon a triangular well approximation [25], the 2D hole dispersion of the light hole and heavy hole bands has been estimated, as shown in the supplementary information. For the carrier densities achieved in this experiment, the Fermi wave vector is predicted to reside well below the crossing point so the extent of hybridisation of the two bands may be limited. However, the exact mechanism has to await a full calculation including the self-consistent solution of the Schrödinger and Poisson equations along the lines given in ref. [3].

We now turn to the roughness parameter d^2L as shown as a function of carrier density by the full circles in Figure. 4b. Again, our present result for the ungated device (open square) agrees with that of our previous publication (280 nm^3) [10]. Because well width fluctuations beyond the scale of the phase coherence length L_ϕ are of no relevance to the analysis presented here we show by the red crosses in Figure. 4b. the roughness parameter divided by L_ϕ. This should represent directly an effective mean square roughness and it is clear from its carrier dependence that geometrical surface roughness alone cannot explain our results because the latter would not depend on carrier density. Indeed, in ref. [10] we reported – measured by atomic force microscopy - a mean square surface roughness of $d_{AFM}^2 = 1.2 \pm 0.3$ nm^2 over a correlation length of the order of the phase coherence length L_ϕ of about 30 nm. Significantly, this is the value that our current data approaches from above as the carrier density increases. Hence it is obvious that the bulk

of the measured roughness is due to fluctuations in well width rather than surface roughness. For the ungated device a fluctuation in well width of about 3 nm would be required to obtain the measured d^2 of about 10 nm^2 provided the two contributions, surface roughness and well width fluctuations, are uncorrelated and add geometrically. Well width fluctuations of about 3 nm could arise from lateral variations in carrier density by about one order of magnitude [3]. This is in keeping with the requirement of spatially inhomogeneous carrier densities of a comparative level in order to interpret Shubnikov-de-Haas oscillations in the hole accumulation layer on (111) diamond [4]. The reduction in well width fluctuation would then be the result of a more homogeneous carrier distribution as more holes are attracted to the 2D layer with increasing gate voltage.

Lateral inhomogeneities in carrier density may be traced to the haphazard transfer doping mechanism with its statistical distribution of OH^- anions in the adsorbed water layer. We note that the above analysis does not consider the possibility that the introduction of the ionic liquid layer may modify the correlation length and magnitude of these doping fluctuations in a manner which would effect the applicability of eq. 1. In Figure. 3, a linear fit was used to describe the dependence of the correction Δ_r on $B_{\parallel}^2$, consistent with eq. 1. However, for cases where the IL is in place, the experimental data may exhibit a non-linear lineshape. Additionally, we presently have no explanation for the substantial drop in g-factor as the IL is placed on the device despite the very small change in carrier density. The above analysis considers only well width fluctuations that are short range, where $L \sim l$, which introduce an additional dephasing on the WAL but do not effect the lineshape of the corresponding magnetoconductance curves. It is possible that the introduction of the IL may modify the distribution of OH^- anions, for example due to the distortion that may arise in the IL as it is cooled, causing deviations in the short-range fluctuations. The introduction of long-range correlations in the doping distribution would give rise to changes in the lineshape of the WAL magnetoconductance curves in a way that would modify the analysis presented here. The correlation length of doping fluctuations in the IL requires a more detailed investigation but this mechanism may illuminate the differing behaviour of the data obtained with and without the IL in place.

V. Summary

We have presented here what we believe to be the first systematic investigation of g-factor and well width fluctuations in the hole accumulation layer of diamond as a function

of carrier density. The results were obtained by analysing the quenching of the weak anti-localization feature in the low temperature magnetoresistance as a function of a magnetic field component parallel to the 2D hole gas while the carrier density was varied by an ionic liquid gate. For carrier densities between 2.27 and 4.35 x10^{13} cm^{-2} the magnitude of the in-plane g-factor increases monotonically from 1.3 to 2.3. The roughness parameter derived from the same measurements drops by a factor of three over the same range of densities and it is evident that initially the geometrical surface roughness as measured by atomic force microscopy contributes only marginally. The main contribution comes from variations in well width traced to lateral inhomogeneities in carrier density. The carrier inhomogeneity is smoothed out as more holes are pulled in by the gate voltage and the roughness parameter approaches within a factor of two the geometrical surface roughness. Variation of the correlation length of fluctuations in the doping distribution in the presence of an ionic liquid, and indeed other commonly used adlayer materials such as transition metal oxides or gate dielectrics, are likely to influence the spin transport properties in the underlying hole gas.

Corresponding Authors

*Email: g.akhgar@latrobe.edu.au; §Email: c.pakes@latrobe.edu.au

Acknowledgments

This work was supported by the Australian Research Council under the Discovery Project (DP150101673).

References:

1. C.I. Pakes, J.A. Garrido, H. Kawarada, *MRS Bulletin*, **39** (6), 542 (2014).
1. Pakes, C.I., J.A. Garrido, and H. Kawarada, *Diamond surface conductivity: Properties, devices, and sensors.* MRS Bulletin, 2014. **39**(6): p. 542-548.
2. Maier, F., et al., *Origin of surface conductivity in diamond.* Physical review letters, 2000. **85**(16): p. 3472.
3. Edmonds, M., C. Pakes, and L. Ley, *Self-consistent solution of the Schrödinger-Poisson equations for hydrogen-terminated diamond.* Physical Review B, 2010. **81**(8): p. 085314.
4. Takahide, Y., et al., *Quantum oscillations of the two-dimensional hole gas at atomically flat diamond surfaces.* Physical Review B, 2014. **89**(23): p. 235304.
5. Edmonds, M.T., et al., *Spin–Orbit Interaction in a Two-Dimensional Hole Gas at the Surface of Hydrogenated Diamond.* Nano letters, 2014. **15**(1): p. 16-20.
6. Akhgar, G., et al., *Strong and Tunable Spin–Orbit Coupling in a Two-Dimensional Hole Gas in Ionic-Liquid Gated Diamond Devices.* Nano letters, 2016. **16**(6): p. 3768-3773.
7. Kuemmeth, F., et al., *Coupling of spin and orbital motion of electrons in carbon nanotubes.* Nature, 2008. **452**(7186): p. 448.
8. Winkler, R., et al., *Spin-Orbit Coupling in Two-Dimensional Electron and Hole Systems*. Vol. 41. 2003: Springer.
9. Minkov, G., et al., *Weak antilocalization in quantum wells in tilted magnetic fields.* Physical Review B, 2004. **70**(15): p. 155323.
10. Akhgar, G., et al., *G-factor and well width variations for the two-dimensional hole gas in surface conducting diamond.* Applied Physics Letters, 2018. **112**(4): p. 042102.
11. Goh, K., M. Simmons, and A. Hamilton, *Electron-electron interactions in highly disordered two-dimensional systems.* Physical Review B, 2008. **77**(23): p. 235410.
12. Garrido, J., T. Heimbeck, and M. Stutzmann, *Temperature-dependent transport properties of hydrogen-induced diamond surface conductive channels.* Physical Review B, 2005. **71**(24): p. 245310.
13. Nebel, C., et al., *Hydrogen-induced transport properties of holes in diamond surface layers.* Applied physics letters, 2001. **79**(27): p. 4541-4543.
14. Bergmann, G., *Weak anti-localization—an experimental proof for the destructive interference of rotated spin 12.* Solid State Communications, 1982. **42**(11): p. 815-817.
15. Hikami, S., A.I. Larkin, and Y. Nagaoka, *Spin-orbit interaction and magnetoresistance in the two dimensional random system.* Progress of Theoretical Physics, 1980. **63**(2): p. 707-710.
16. Knap, W., et al., *Weak antilocalization and spin precession in quantum wells.* Physical Review B, 1996. **53**(7): p. 3912.
17. Mal'shukov, A., K. Chao, and M. Willander, *Magnetoresistance of a weakly disordered III-V semiconductor quantum well in a magnetic field parallel to interfaces.* Physical Review B, 1997. **56**(11): p. 6436.
18. Mal'shukov, A., V. Shlyapin, and K. Chao, *Effect of the spin-orbit geometric phase on the spectrum of Aharonov-Bohm oscillations in a semiconductor mesoscopic ring.* Physical Review B, 1999. **60**(4): p. R2161.
19. Mensz, P., et al., *Determination of spatial potential fluctuations in Si and GaAs inversion layers by weak localization.* Applied physics letters, 1987. **50**(10): p. 603-605.
20. Mensz, P. and R. Wheeler, *Magnetoconductance due to parallel magnetic fields in silicon inversion layers.* Physical Review B, 1987. **35**(6): p. 2844.

21. Anderson, W.R., et al. *Determination of Si/SiO/sub 2/interface roughness using weak localization*. in *VLSI Technology, Systems, and Applications, 1993. Proceedings of Technical Papers. 1993 International Symposium on*. 1993. IEEE.
22. Minkov, G., et al., *Transverse negative magnetoresistance of two-dimensional structures in the presence of a strong in-plane magnetic field: Weak localization as a probe of interface roughness.* Physical Review B, 2004. **70**(3): p. 035304.
23. Cabañas, S., et al., *Suppression of weak antilocalization in an Al x Ga 1− x N/ Ga N two-dimensional electron gas by an in-plane magnetic field.* Physical Review B, 2007. **75**(19): p. 195329.
24. Mathur, H. and H.U. Baranger, *Random Berry phase magnetoresistance as a probe of interface roughness in Si MOSFET's.* Physical Review B, 2001. **64**(23): p. 235325.
25. Ando, T., A.B. Fowler, and F. Stern, *Electronic properties of two-dimensional systems.* Reviews of Modern Physics, 1982. **54**(2): p. 437.

5.3 Supplementary Information

G-Factor and Well-Width Fluctuations as a Function of Carrier Density in the 2D Hole Accumulation Layer of Transfer Doped Diamond

Golrokh Akhgar,*[1] Lothar Ley,[1,2], Daniel L. Creedon,[3] Alastair Stacey,[3] Jeffrey C. McCallum,[3] Alex R. Hamilton[4] and Christopher I. Pakes§[1]

[1] Department of Chemistry and Physics, La Trobe University, Victoria 3086, Australia

[2] Institute of Condensed Matter Physics, Universität Erlangen, Staudt-Str. 1, 91058 Erlangen, Germany

[3] School of Physics, The University of Melbourne, Victoria 3010, Australia

[4] School of Physics, University of New South Wales, Sydney, New South Wales 2052, Australia

1. Determining the hole-hole interaction correction

In 2D samples quantum corrections are due to the weak localization and weak anti-localization and Hole-hole interaction (HHI). The conductivity corrections due to $\delta\sigma_{WL}$, $\delta\sigma_{WAL}$ and $\delta\sigma_{HHI}$ to the longitudinal conductivity is given by the equation below while Hall conductivity is not affected:

$$\sigma_{xx} = \delta\sigma_{WL} + \delta\sigma_{WAL} + \delta\sigma_{HHI} \quad \text{(S1)}$$

Starting with HHI correction; this intrinsic quantum correction to the resistivity does not connected to the phase coherent backscattering of electrons/holes (WL and WAL). The main comparison to magnetoconductivity effects is that HHI is independent of magnetic field and it is the interaction of two different holes instead of interaction of a hole to itself. The theoretical framework of HHI is developed by Alshuler and Aronov [1] and it is originally based on electron systems, but similar approach can be used for p-type samples. We adopt method II by Goh et al. [2] to extract hole-hole interaction strength, K_{hh}. This is done by subtraction HHI correction term $\Delta\sigma_{HHI}$ to the longitudinal conductivity from both ρ_{xx} (B) and ρ_{xy} (B) traces. This method of HHI correction is previously applied and

described on H-terminated diamond devices [3]. The HHI correction term to the Drude conductivity is given by:

$$\Delta\sigma_{HHI} = K_{hh}G_0 \ln\left(\frac{k_b T\tau}{\hbar}\right) \quad \text{(S2)}$$

Where $G_0 = e^2/\pi h$, T is the temperature, K_{hh} is the dimensionless Coulomb interaction strength, and $\tau = \sigma_D m^*/pe^2$ is the transport relaxation time with p the areal hole density, σ_D the Drude conductivity and m^* the effective hole mass for dispersion in the plane of the 2D system. We adopt the value $m^* = 0.208m_0$ for the 2D heavy hole mass, [4] and equate σ_D to $\sigma_{xx}(30\ K)$ to obtain τ from the longitudinal conductivity. The values of σ_D and τ for different gate voltages are listed in Table SI.

Figure S1 shows logarithmic dependence of the HHI correction. The K_{hh} is determined by slope of ΔR_H Vs ln (T):

$$K_{hh} = -\frac{Hall\ slope \times \sigma_{xx}(30K)}{2G_0} \quad \text{(S3)}$$

where $\Delta R_H(T) = (R_H(T) - R_H(20\ \text{K}))/R_H(20\ \text{K})$ under assumption that Hall resistivity at 20 K approaches its Drude limit.

K_{hh} for all different gate biases are listed in Table 1. As it is also explained in Ref [3] after subtraction of HHI from ρ_{xx} (B) and ρ_{xy} (B), The corrected ρ_{xy} (B) traces should collapse onto one single trance, otherwise, K_{hh} should be systematically adjusted and $\Delta\sigma_{HHI}$ should be recalculated until all ρ_{xy} (B) traces collapse onto one curve as it shows in figure S2. The corresponding adjusted K_{hh} is listed in table 1 for all gate biases.

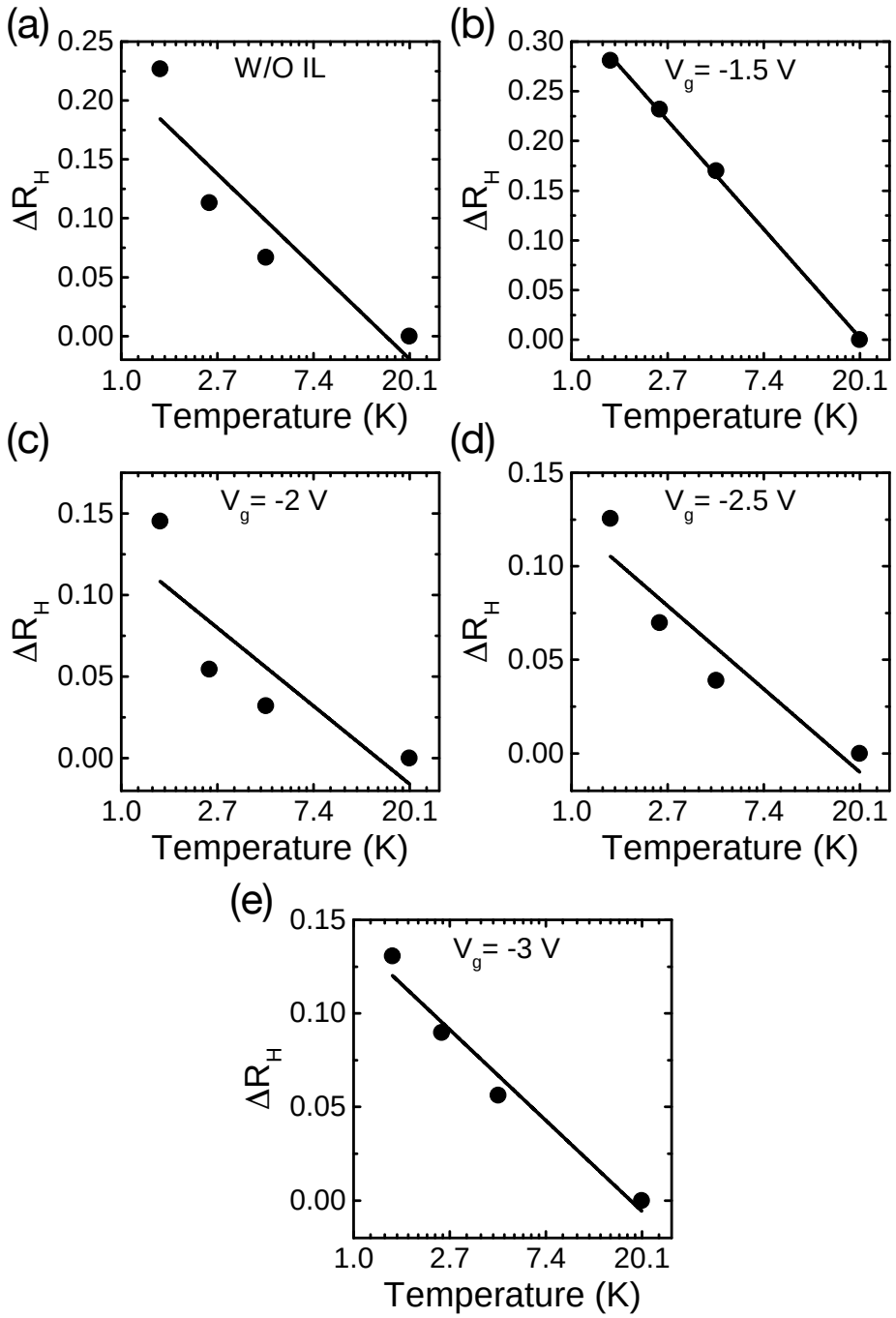

Figure S1: ΔR_H plotted as a function of temperature for all different gate biases. Demonstrating logarithmic dependence on T. The slope of these plots are used to calculate the value of K_{hh} as explained in the text.

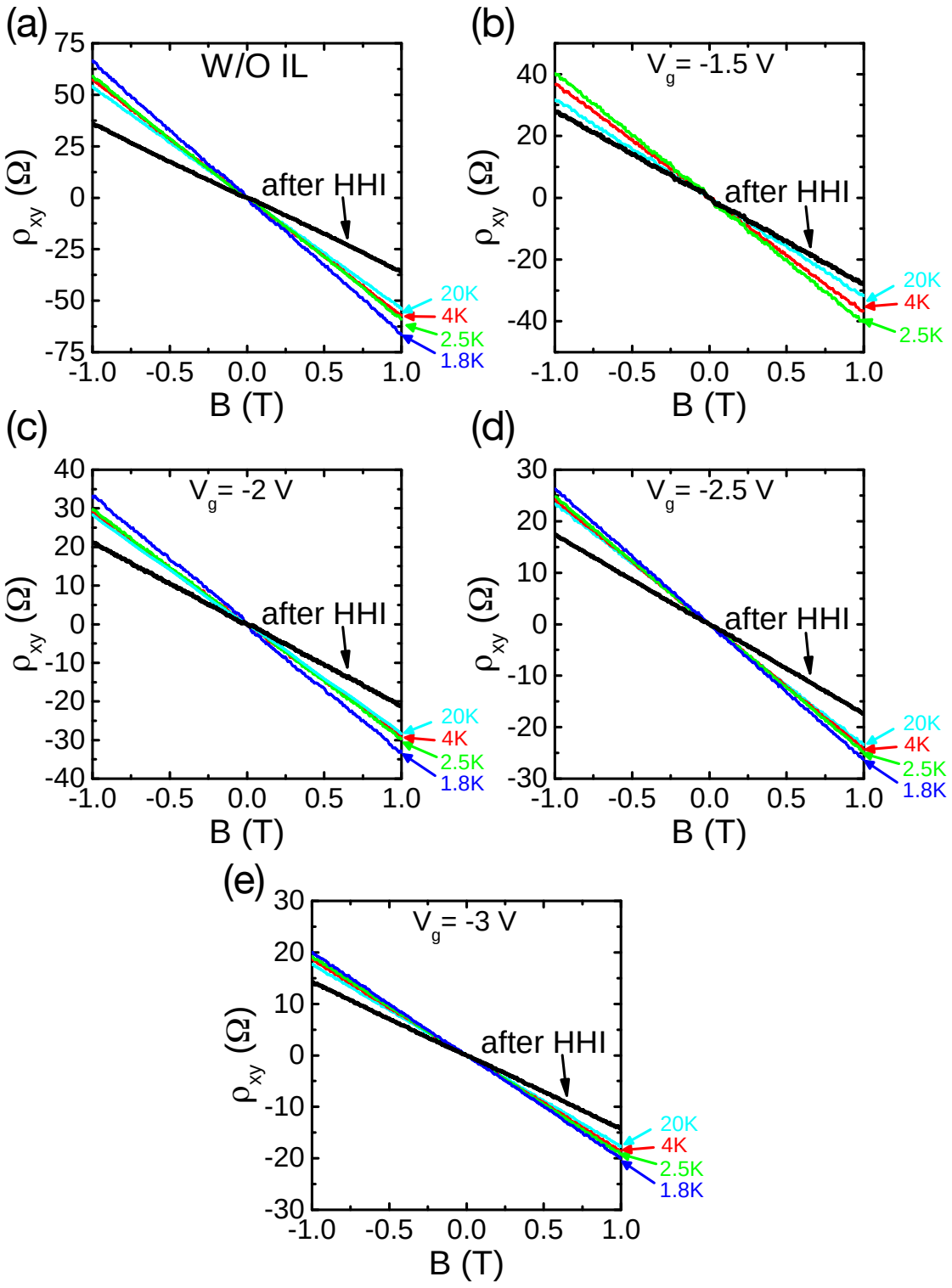

Figure S2: $\rho_{xy}(B)$ before and after HHI removal. Corrected traces of all temperatures are collapsed onto one trace after successful removal of $\Delta\sigma_{HHI}$ from the measured magnetotransport data.

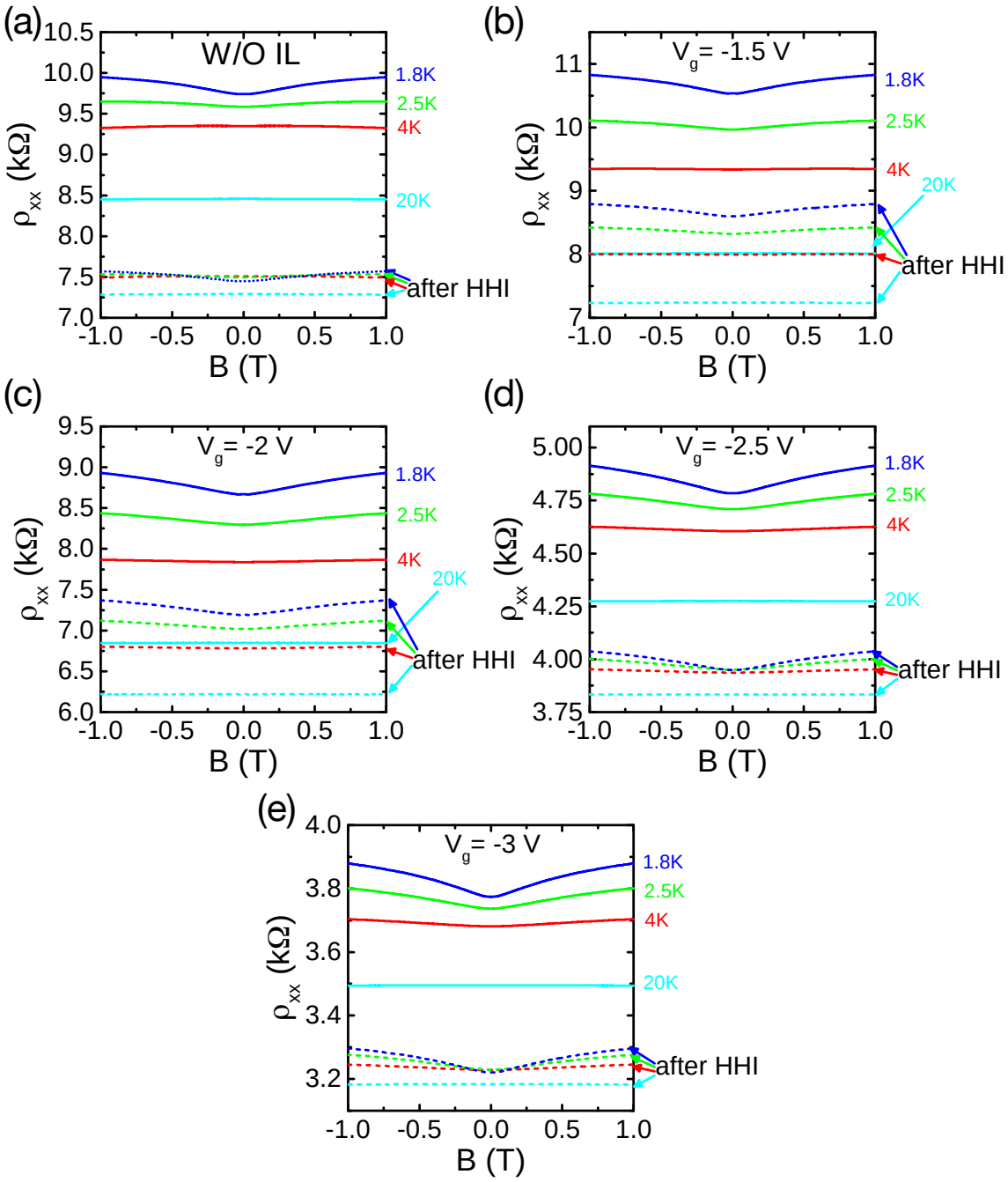

Figure S3: $\rho_{xx}(B)$ before and after successful removal of $\Delta\sigma_{HHI}$ from the measured magnetotransport data.

When the final K_{hh} is stablished for all gate voltages, a similar K_{hh} is used for HHI correction in each set of measurements with constant in-plane magnetic field.

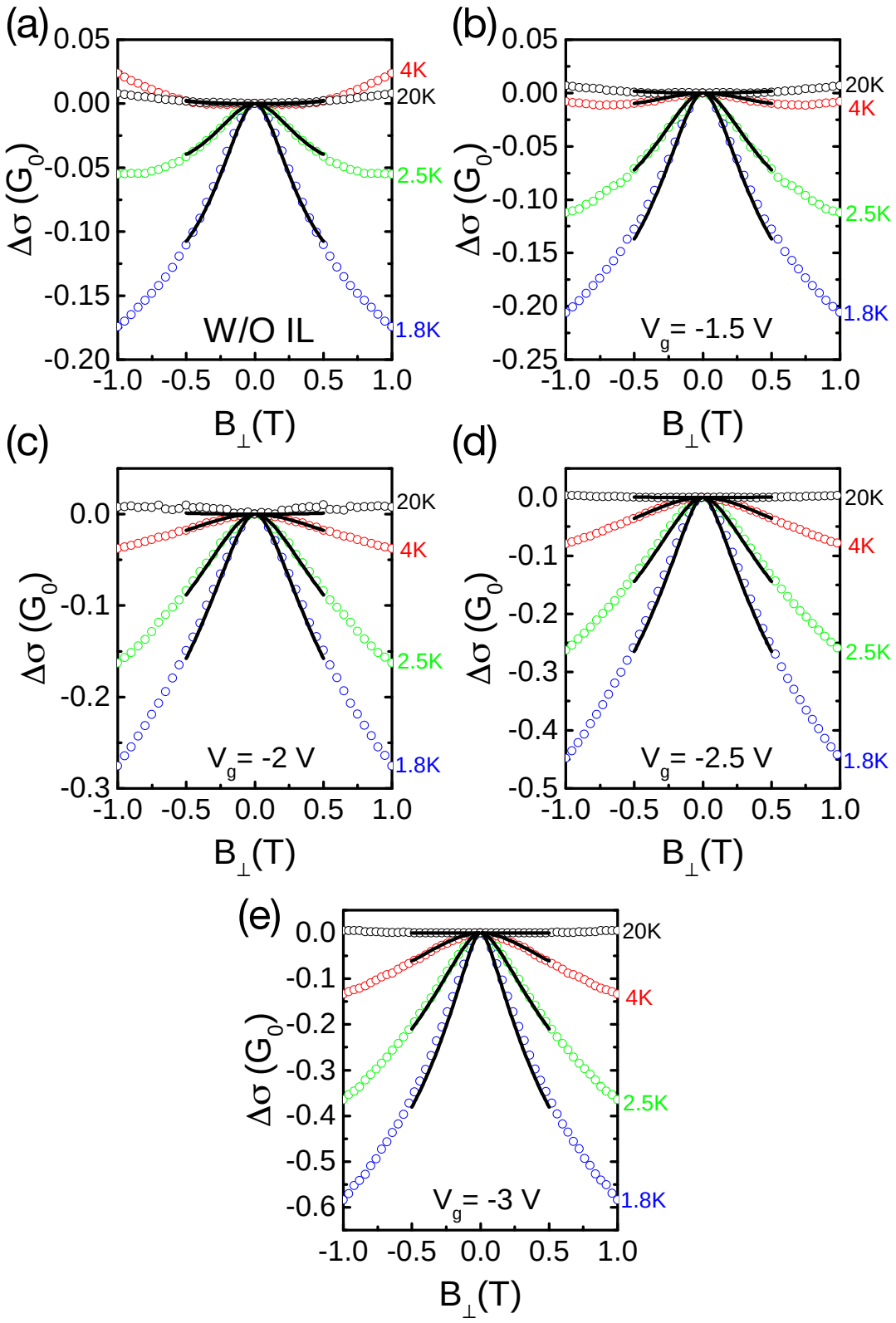

Figure S4: Reduced magnetoconductivity (in units of $G_0 = e^2/\pi h$), at different temperatures plotted for all gate voltages. The black solid lines correspond to fits to equation 4.

2. Fitting magnetoconductivity data to 2D localization theory

The dominant spin-orbit interaction mechanism is k^3 Rashba-like mechanism [5]. The corrected magnetoconductivity data $\Delta\sigma$ for different temperatures are plotted in Figure. S4 and fitted to the k^3 Rashba using eq. 4. The spin and phase characteristic fields B_{so} and B_ϕ are extracted for each gate bias from the fits. Phase and spin coherence lengths are calculated using $L_\phi = (\hbar/(4eB_\phi))^{0.5}$ and $L_{SO} = (\hbar/(4eB_{SO}))^{0.5}$ respectively and plotted in figure S5 for all gate biases. The scale $L_\phi \sim T^{-0.5}$, confirms the two dimensionality of this system.

$$\Delta\sigma = \frac{e^2}{2\pi^2\hbar}\left[\Psi\left(\frac{1}{2}+\frac{B_\phi+B_{so}}{B}\right)+\frac{1}{2}\Psi\left(\frac{1}{2}+\frac{B_\phi+2B_{so}}{B}\right)-\frac{1}{2}\Psi\left(\frac{1}{2}+\frac{B_\phi}{B}\right)-\ln\left(\frac{B_\phi+B_{so}}{B}\right)-\frac{1}{2}\ln\left(\frac{B_\phi+2B_{so}}{B}\right)+\frac{1}{2}\ln\left(\frac{B_\phi}{B}\right)\right] \quad \text{(S4)}$$

After fitting the magnetotransport data, the phase relaxation time $\tau_\phi = \hbar/(4eDB_\phi)$ calculated and plotted in figure , it shows no dependency in gate bias and scales as $\tau_\phi \sim T^{-1}$, showing the evidence for a scattering mechanism consistent with Nyquist dephasing as expected in a weakly disordered 2D system [2, 6]. The spin orbit interaction is calculated from $\Delta_{SO} = \hbar/(2\tau\tau_{SO})^{1/2}$ where $\tau_{SO} = \hbar/(4eDB_{SO})$ is the spin relaxation time. Δ_{SO} is plotted as a function of density in figure S6 (d).

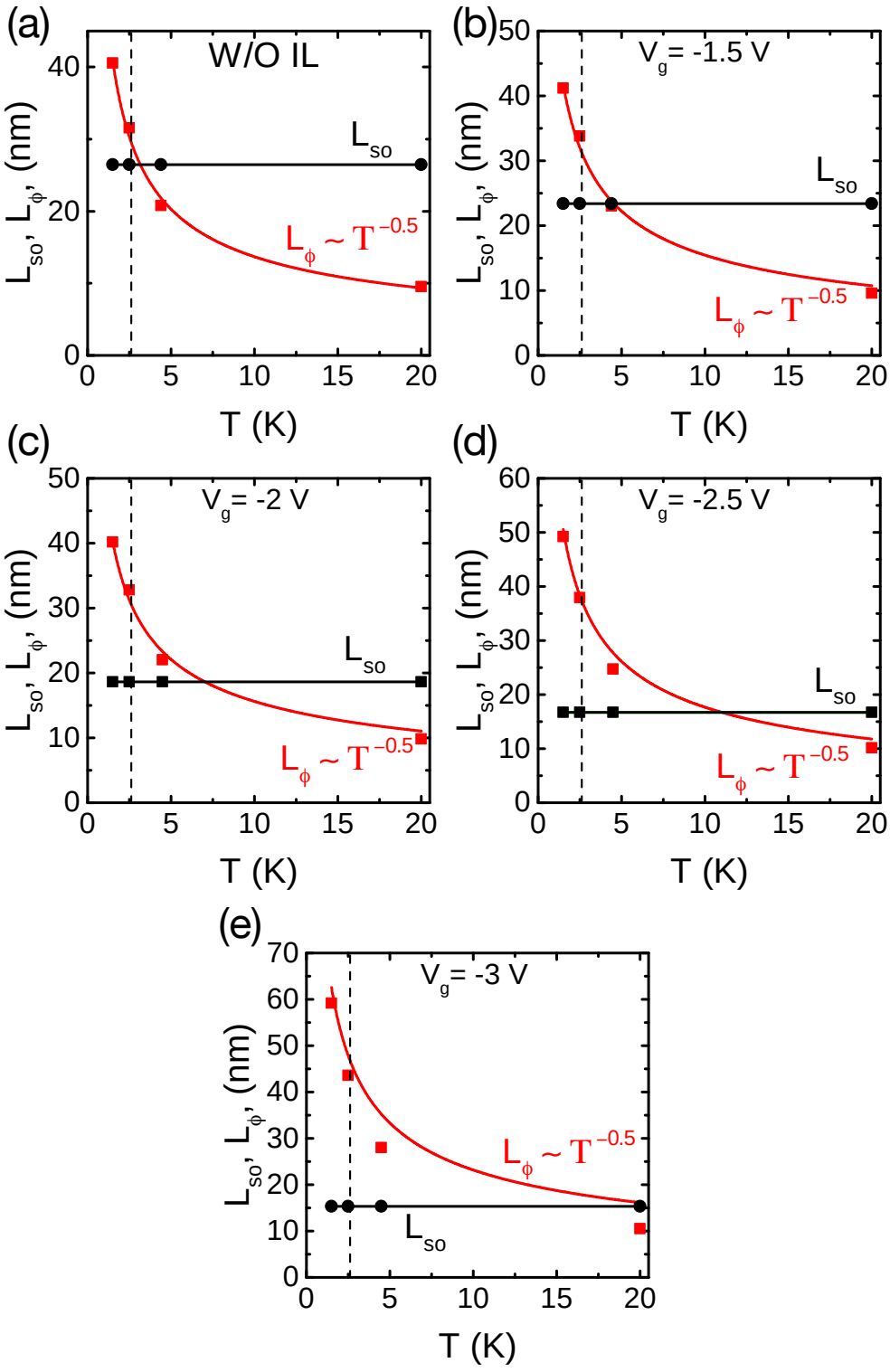

Figure S5: Temperature dependence of the characteristic spin coherence lengths, L_{SO}, (black circle) and phase coherence lengths, L_{ϕ}, (red square) with gate voltage V_g as parameter. The lines represent a $T^{-0.5}$ fit for L_{ϕ}.

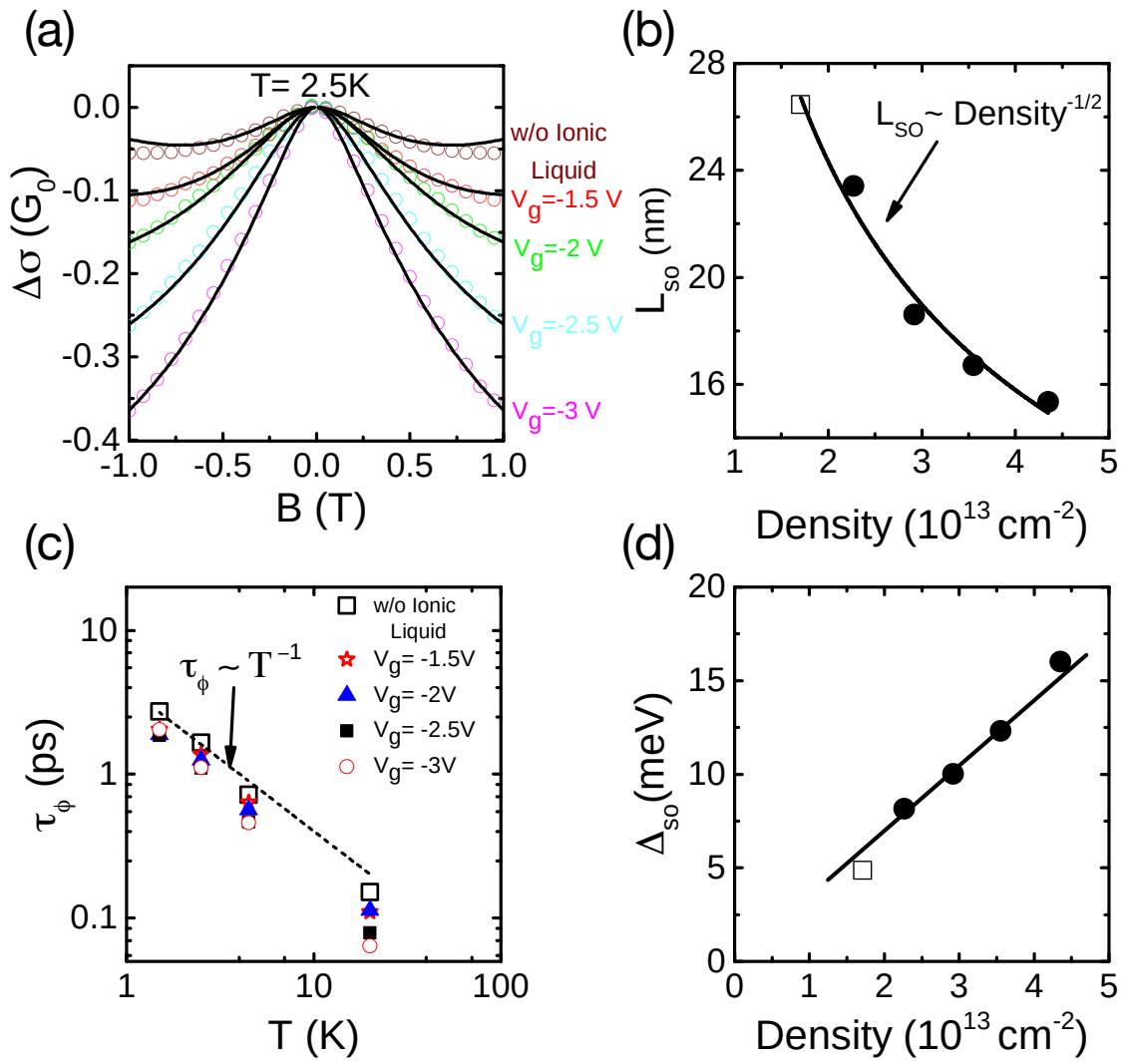

Figure S6: (a) Reduced magnetoconductivity, $\Delta\sigma = \sigma(B) - \sigma(B = 0)$ (in units of $G_0 = e^2/\pi h$), for different gate bias at 2.5 K; (b) spin coherence length L_{so} as a function of hole density; (c) temperature dependence of the dephasing time (τ_ϕ) plotted at different gate biases; the broken line indicates $\tau_\phi \sim T^{-1}$ consistent with Nyquist dephasing; (d) tuning of the spin-orbit splitting strength, Δ_{SO}, with hole sheet density; the solid line is a linear fit to the data. The open squares represent the data obtained for the un-gated device in all figures.

Table SI: Summary of calculated parameters

Gate Voltage, V_g[V]	w/o IL	-1.5	-2.0	-2.5	-3.0
Estimated Interaction strength, K_{hh}, obtained from the slope of normalised $\rho_{xy}/B(\Omega/T)$ vs. $\ln(T)$	0.396	0.554	0.309	0.436	0.578
Interaction strength, K_{hh}, obtained from collapsing all $\rho_{xy}^{Measured}(B)$ onto one curve ($\rho_{xy}^{Corrected}(B)$)	0.40±0.01	0.25±0.03	0.28±0.03	0.54±0.01	0.55±0.01
Hole sheet density, *p,* before HHI removal [$10^{13}cm^{-2}$] (20K)	1.16	1.98	2.19	2.67	3.52
Hole sheet density, *p,* after HHI removal [$10^{13}cm^{-2}$]	1.17	2.27	2.92	3.55	4.35
Drude conductivity, σ_D [$10^{-4}\Omega^{-1}$] (30K)	1.23	1.33	1.58	2.42	2.94
Transport relaxation time, τ [fs]	7.9	4.95	4.33	6.68	6.15
Mean free path, l [nm]	3.1±0.1	2.9±0.1	3.0±0.2	4.2±0.5	4.6±0.5
Diffusion coefficient, D [$10^{-3}m^2s^{-1}$]	0.9±0.1	1.0±0.1	1.1±0.1	1.7±0.2	2.1±0.2
Characteristic transport field, B_{tr} [T]	34.52	39.88	36.01	18.86	15.62

3. Minkov Fitting:

We performed magnetotransport measurements in the presents of constant B field. Constant in-plane B field, $B_{\|}$, in the range of 0 to 1 T with steps of 0.2T is applied while sweeping the perpendicular magnetic field from -1 to 1T. The B_{ϕ} and B_{so} remains constant as a function of $B_{\|}$ for that reason we use the same B_{so} and B_{ϕ} that we extracte from the equation above at 2.5K. and by following Minkov *et. al.* method [7] Zeeman splitting and interface roughness terms are extracted. This is done by adding Zeeman term to singlet terms of the equation 4 and interface roughness to both singlets and triplets:

$$\Delta\sigma = \frac{e^2}{2\pi^2\hbar}\left[\Psi\left(\frac{1}{2}+\frac{B_{\phi}+B_{so}+\Delta_r}{B}\right)+\frac{1}{2}\Psi\left(\frac{1}{2}+\frac{B_{\phi}+2B_{so}+\Delta_r}{B}\right)-\frac{1}{2}\Psi\left(\frac{1}{2}+\frac{B_{\phi}+\Delta_S+\Delta_r}{B}\right)-\ln\left(\frac{B_{\phi}+B_{so}+\Delta_r}{B}\right)-\frac{1}{2}\ln\left(\frac{B_{\phi}+2B_{so}+\Delta_r}{B}\right)+\frac{1}{2}\ln\left(\frac{B_{\phi}+\Delta_S+\Delta_r}{B}\right)\right] \quad \text{(S5)}$$

$\Delta_S$and Δ_r is extracted for each gate bias and plotted as a function of $B_{\|}^2$.

4. Calculation of hole band dispersion:

The 2D dispersion curves of the heavy hole and light hole bands, calculated using the approach of ref [8] with a triangular well approximation, are given in Figure S7. The energy dispersion, $E = \hbar^2k^2/(2m_0m_{eff})$, where we have adopted the effective mass values of $m_{hh}^* = 0.208m_0$ and $m_{lh}^* = 0.288m_0$ for the heavy hole and light hole respectively from Ref [4, 9] that are appropriate for the direction parallel to the surface of diamond.

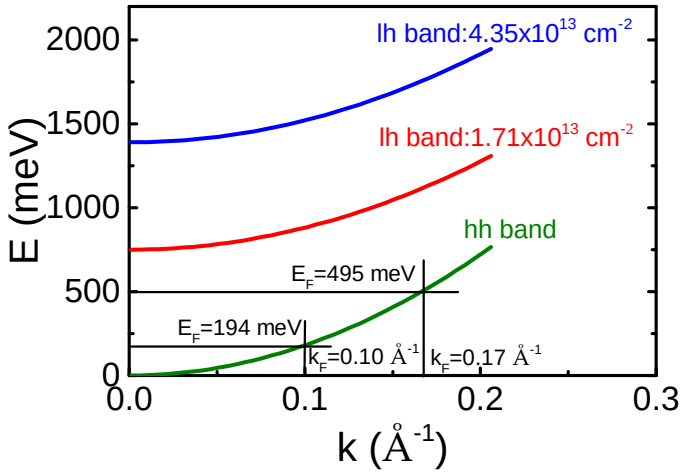

Figure S7: shows the 2D hole dispersion for lowest and highest density achieved in this experiment for k in the (100) plane. $k_F = (2\pi p)^{1/2}$ is the Fermi wave vector where p the areal hole concentration, and $E_F = pe/\varepsilon_0\varepsilon_D$ is the Fermi energy where ε_0 is the permittivity of vacuum and $\varepsilon_D = 5.7$ is the permittivity of diamond.

Corresponding Authors

*Email: g.akhgar@latrobe.edu.au; §Email: c.pakes@latrobe.edu.au

References

1. Altshuler, B.L. and A.G. Aronov, *Electron–electron interaction in disordered conductors*, in *Modern Problems in condensed matter sciences*. 1985, Elsevier. p. 1-153.
2. Goh, K., M. Simmons, and A. Hamilton, *Electron-electron interactions in highly disordered two-dimensional systems.* Physical Review B, 2008. **77**(23): p. 235410.
3. Akhgar, G., et al., *Strong and Tunable Spin–Orbit Coupling in a Two-Dimensional Hole Gas in Ionic-Liquid Gated Diamond Devices.* Nano letters, 2016. **16**(6): p. 3768-3773.
4. Edmonds, M.T., et al., *Spin–Orbit Interaction in a Two-Dimensional Hole Gas at the Surface of Hydrogenated Diamond.* Nano letters, 2014. **15**(1): p. 16-20.
5. Knap, W., et al., *Weak antilocalization and spin precession in quantum wells.* Physical Review B, 1996. **53**(7): p. 3912.
6. Altshuler, B.L., A. Aronov, and D. Khmelnitsky, *Effects of electron-electron collisions with small energy transfers on quantum localisation.* Journal of Physics C: Solid State Physics, 1982. **15**(36): p. 7367.
7. Minkov, G., et al., *Weak antilocalization in quantum wells in tilted magnetic fields.* Physical Review B, 2004. **70**(15): p. 155323.
8. Ando, T., A.B. Fowler, and F. Stern, *Electronic properties of two-dimensional systems.* Reviews of Modern Physics, 1982. **54**(2): p. 437.
9. Naka, N., et al., *Direct measurement via cyclotron resonance of the carrier effective masses in pristine diamond.* Physical Review B, 2013. **88**(3): p. 035205.

6

Conclusion

6.1 Thesis Summary

This thesis presented a series of studies relating to the spin properties of the two-dimensional hole band in surface conducting diamond. We have performed magnetotransport measurements in surface conducting diamond Hall bar devices using both perpendicular and parallel magnetic fields and at different temperatures. Interpretation of these measurements using existing quantum transport models have allowed us to determine the dimensionality of the hole accumulation layer and to determine the gyromagnetic ratio of holes in this system, to determine the spin-orbit interaction of the holes and demonstrate its tunability with an electrostatic gate, and to probe the microroughness of the hole quantum confinement potential.

The key results of this thesis are as follows:

- We have shown that surface conducting hydrogen-terminated diamond possesses a 2D hole band with the tunable spin orbit splitting at its surface. The spin orbit coupling strength determined here is the highest reported for a 2D hole system and is comparable in strength with the best 2D electron systems. In this work, we have used an ionic liquid to gate to control the hole carrier density and spin orbit

coupling in Hall bar devices fabricated in hydrogen terminated (100) diamond. By employing this simple gating method, we have been able to engineer the spin orbit coupling over a five-fold dynamic range, from 5 to 25 meV. This tunability in spin-orbit coupling is achieved because the spin orbit interaction arises from the asymmetry of the confinement potential well through the Rashba effect. The well asymmetry is modulated, via the Poisson equation, when the hole carrier density is modified by the gate potential. The significant extent of band bending at the surface gives rise to a highly asymmetric confinement potential for holes. The results of this work have been published in journal *Nano Letters* (2016).

- The magnetoconductance in surface conducting Hall devices is found to be highly anisotropic in its response to an external magnetic field when an in-plane field, parallel to the diamond surface, is applied in addition to a perpendicular field. While this provides further evidence to the 2D nature of the hole band, the application of an in-plane field while sweeping the perpendicular magnetic field provides a method to probe the gyromagnetic ratio of the holes in the surface accumulation layer; to our knowledge this is the first time the g-factor of 2D holes in diamond has been determined. This has been achieved by observing the quenching of the signature WAL 'cusp' in the magnetoconductance as the in-plane magnetic field was increased in strength, with data analysed using the same quantum transport models as noted above but with the addition of a Zeeman interaction term. The in-plane hole g-factor determines the coupling strength of the hole spin with an external magnetic field, and thus plays an important role in devices for spin transport. As we have shown, the addition of an in-plane magnetic field also enables us to probe fluctuations in the width of the hole confinement potential which cause an additional dephasing of the WAL. In the devices probed here, the magnetoconductance correction arising from this microroughness was found to be greater than that of the Zeeman interaction. Furthermore, the level of fluctuations deduced from modelling of the magnetoconductance curves was found to be greater than the surface roughness obtained from atomic force microscopy images of the surface, suggesting that the microroughness inferred from magnetotransport measurements arises from a significant inhomogeneity in the hole carrier density, with variations of up to an order of magnitude over lateral length-scales of the phase coherence length. This work, published in *Applied Physics Letters* (2018), presents a new picture of the hole accumulation layer in

surface conducting diamond, suggesting that the 2D charged sheet forms local ‘puddles’ on short-range (about 30 nm and less) lateral length scales.

- Finally, we have combined the in-plane magnetotransport measurement techniques with our ionic liquid gating methodologies to probe the g-factor of the hole band and well width fluctuations as a function of hole carrier density. In the presence of an ionic liquid gate, the magnitude of the hole g-factor was found to increase monotonically from 1.3 to 2.3 and the roughness parameter dropped by factor of three while the hole sheet density was increased by a similar factor using the ionic liquid gate. As we discussed in Chapter 5, it may be evident in this work that the extent of inhomogeneity in the hole density is modified in the presence of an ionic liquid. This may be the case if the distribution of negative ions in the ionic liquid is different to that when only water is on the diamond surface; when the electric field is increased using the gate the distribution is modified further. This suggests that more investigation using different theoretical models is required to evaluate the possibility that long-range fluctuations in quantum well width arise as a result of charge distributions when ionic liquid is applied. This work has been submitted to *Physical Review B* (2018).

6.2 Future Outlook

- In this thesis we have used ionic liquid gating techniques to tune the hole sheet density of the hole band. Ionic liquid gating has many advantages compared to gating with a solid state dielectric such as Al_2O_3. The ionic liquid is straightforward to apply to a device using a micropipette and causes minimal chemical modification of the surface termination. As we have shown, it can be used to engineer the device over a considerable range of carrier density and importantly provides a reliable gating methodology with low leakage current compared to conventional solid state gated devices [1, 2]. However, the major disadvantage of this gating method is that the device must be warmed to room temperature in order to change the gate bias which is time consuming when measurements are being conducted at cryogenic temperatures using a dilution refrigerator. While this is not an issue for the measurements conducting here, operation of a gated diamond device in the form of a MOSFET or MISFET requires fast operation and therefore necessitates a gate with a solid-state

dielectric that can be operated at low temperature. While Al_2O_3 gating is regularly used to fabricate devices such as MOSFETs or MISFETs on diamond it is likely that the achievable hole density in these devices is not as high as that achieved using ionic liquid gating [3, 4]. For this reason, alternative 'soft' dielectric materials such as parylene can be explored for use as gate insulators. Parylene has properties that are desirable for use as a gate insulator in diamond transistors [5, 6].

- As we note above, alternative theoretical models should be explored to explain the magnetoconductance behaviour observed in in-plane field measurements in the presence of an ionic liquid. As Mathur *et al.* [7] notes, the presence of long-range fluctuations in quantum well width necessitates a microroughness correction in the Hikami equation that takes a different form in its dependence on the in-plane field; this would be an important extension to this work, however the precise form that correction should take is currently not clear.

  It would be interesting to also perform in-plane magnetotransport measurements with a diamond device doped using a transition metal oxide adlayer such as MoO_3 for which, in principle, the negative carriers in the adlayer are mobile at any temperature [8]. Such a device may exhibit a very different lateral charge distribution to those studies here and, in the case where charge is mobile in the transition metal oxide layer, it may be possible to explore magnetotransport in the diamond device in the presence of Coulombic drag between the positive and negative charged layers.

  An alternative way of introducing "micro-roughness" to the 2D hole gas at the diamond surface would be to apply magnetic impurities to the surface; the length scale of these impurities would in principle dictate the range of the imposed fluctuations. A possible example would be the molecule ferrocene that has been previously studied on graphene [9] and for which the Kondo effect has been explored. Similar studies on surface conducting diamond may well be feasible as long as the presence of the magnetic molecules does not disrupt the underlying surface transfer doping.

- The overriding aim of understanding the spin transport properties of materials is to make real-life devices that utilise carrier spin for the transport of information. An important example is the spin FET. While our diamond devices show the high and tunable spin-orbit coupling required to control the carrier spin with a gate, to operate coherently these devices must to be engineered with a channel length on the scale of L_{SO} which we have shown to be about 30 nm and therefore in principle experimentally achievable using electron beam lithography processing techniques. In addition, a method to inject and detect the spin of carriers at the source and drain of the device is required. This is a more complex problem and extensive work needs to be done to explore, for example, the electronic properties of ferromagnetic materials as potential electrical contacts on the hydrogen-terminated diamond surface. This field is very much in its infancy and there are some interesting experiments to undertake in the years ahead.

- One last thing that I believe is necessary to consider further is the hole mobility and to explore possible routes to engineering a device with higher mobility. Compared to other common 2D materials, such as graphene, the mobility of holes in surface conducting diamond is low and, as we have explained, originates from scattering due to charged impurities in the surface water layer. In principle, if this scattering mechanism can be eliminated the mobility of carriers in the 2D hole band could be increased from 50 $cm^2V^{-1}s^{-1}$ to several thousand, due to the high mobility of carriers in the diamond bulk. However, achieving this will be difficult and a new approach to fabrication of the device would be required. One approach, in principle, would be to remove the surface water layer and utilise an ionic liquid gate to draw carriers from the device leads with the surface otherwise encapsulated to prevent further exposure to water. There are a number of gating approaches being explored in the field of topological electronics, such as the use of thin sheets of h-BN [10], and which may be applicable to future surface conducting diamond devices.

6.3 Closing Remarks

We started this thesis by reflecting on the extraordinary electrical and physical properties of diamond. These have given rise to a diverse range of important applications such as coatings for machine tools due to its hardness, electron emission devices as a result of its negative electron affinity, and as a heat sink due to its very high thermal conductivity.

The work of this thesis has been ultimately achieved due to another well-known property of diamond - its high electric breakdown field. As we have described this allows a quantum well to be established as a result of a significant band bending which arises from surface transfer doping. With its high breakdown field, diamond can sustain a triangular confinement potential which is highly asymmetric and it is this asymmetry, through the Rashba effect, that produces the high spin orbit interaction that we have described. It is remarkable that this can be achieved in a diamond substrate that simply has a hydrogen-terminated and has been exposed to air.

References

1. Kim, S.H., et al., *Electrolyte-Gated Transistors for Organic and Printed Electronics.* Advanced Materials, 2013. **25**(13): p. 1822-1846.
2. Raymundo-Pinero, E., et al., *Relationship between the nanoporous texture of activated carbons and their capacitance properties in different electrolytes.* Carbon, 2006. **44**(12): p. 2498-2507.
3. Kawarada, H., *High-current metal oxide semiconductor field-effect transistors on H-terminated diamond surfaces and their high-frequency operation.* Japanese Journal of Applied Physics, 2012. **51**(9R): p. 090111.
4. Pakes, C.I., J.A. Garrido, and H. Kawarada, *Diamond surface conductivity: Properties, devices, and sensors.* MRS Bulletin, 2014. **39**(6): p. 542-548.
5. Gluschke, J.G., et al., *Using ultra-thin parylene films as an organic gate insulator in nanowire field-effect transistors.* Nano Letters, 2018.
6. Sabri, S., et al., *Graphene field effect transistors with parylene gate dielectric.* Applied Physics Letters, 2009. **95**(24): p. 242104.
7. Mathur, H. and H.U. Baranger, *Random Berry phase magnetoresistance as a probe of interface roughness in Si MOSFET's.* Physical Review B, 2001. **64**(23): p. 235325.
8. Russell, S.A., et al., *Surface transfer doping of diamond by MoO3: A combined spectroscopic and Hall measurement study.* Applied Physics Letters, 2013. **103**(20): p. 202112.
9. Jobst, J., F. Kisslinger, and H.B. Weber, *Detection of the Kondo effect in the resistivity of graphene: Artifacts and strategies.* Physical Review B, 2013. **88**(15): p. 155412.
10. Petach, T.A., et al., *Disorder from the Bulk Ionic Liquid in Electric Double Layer Transistors.* ACS nano, 2017. **11**(8): p. 8395-8400.